Connecting the drops: Exploring precipitation changes from a process and weather perspective

Kjersti Konstali

UNIVERSITY OF BERGEN

Connecting the drops: Exploring precipitation changes from a process and weather perspective

Kjersti Konstali

Thesis for the degree of Philosophiae Doctor (PhD)
at the University of Bergen

Date of defense: 22.03.2024

Year: 2024

Title: Connecting the drops: Exploring precipitation changes from a process and weather perspective

Name: Kjersti Konstali

Print: Skipnes Kommunikasjon / University of Bergen

Scientific environment

This study was carried out at the Geophysical Institute, University of Bergen and the Bjerknes Centre for Climate Research in Norway. During my PhD, I received a grant from the Meltzer Foundation to visit the National Center for Atmospheric Research in Boulder, Colorado, US. I have been enrolled in the Norwegian Research School on Changing Climates in the Coupled Earth System (CHESS).

Acknowledgments

First and foremost, I would like to thank my supervisors, Asgeir Sorteberg and Thomas Spengler. Thank you, Asgeir, for the weekly meetings and chats that kept me on track. Your trust in allowing me to take ownership of my project and explore precipitation my own way meant a lot to me. I appreciate the outreach opportunities you directed my way – I genuinely enjoyed them. Thomas, I am grateful for your interest in my work and that you took on the role as co-superviser halfway through my project. I am deeply impressed by your superb and fast feedback, and thanks for inspiring me to do my best.

Clemens, a special thank you for your valuable collaboration and thoughtful comments, and for introducing me to dynlib. Thanks to Ethan Gutmann for hosting me for a couple of months at NCAR in Boulder and for introducing me to ICAR, but most importantly, thanks for giving me access to NCAR's supercomputer and the CESM2-LE simulations – which ended up providing enough material for both Paper III and Paper IV.

Thanks to my friends and colleagues at GFI, both old and new, for making it such a great place that I ended up staying for 10+ years even though my plan was to leave after one. Thanks for making it an inclusive community where I feel at home, especially when tackling colleagues on the football field, discussing the weather every Friday, or science during MetLunch.

Thanks to the DynMet group for the meetings, dinners, and company on the conferences, and for making me part of a scientific community. Thanks to those who cheered me across the finish line, especially everyone in room 3050.

Thanks to Isak and Reidun for reading through my sammendrag for the thesis. To the football girls in Skansens for the weekly reminder that there is a world outside of academia and for the company during covid. Thanks to my family for their perennial support and listening to my PhD problems when I needed to vent. But most of all, thanks to Till! Thanks for all the input, the figure discussions, and for allowing me to sometimes have lectures during dinner when there were no more work debriefs while biking home. Thanks for pushing me, being proud of (at) me, and for all the support. And lastly, thanks for reading this thesis more times than anyone should have to.

Kjersti Konstali
Bergen, December 2023

Abstract

Precipitation provides one of the most fundamental resources to humankind: freshwater. Extreme precipitation, however, can be a threat through floods and landslides. It is, therefore, crucial to determine the change of precipitation in the past, present, and future, as well as its dominant drivers and how it is represented in climate models. Global mean precipitation is projected to increase, with extreme precipitation expected to increase even more. This increase is due to both thermodynamic and dynamic contributions, with the latter being the main source of uncertainty. We therefore explore past and future precipitation changes from a process and weather perspective in four studies, using observations, reanalyses, and a climate model.

In Paper I, we use precipitation observations from Norway to investigate the changing precipitation characteristics over the past century. We find that precipitation in Norway increased by 19% between 1900-2019, almost half of which occurred between 1980-1999. We use a simple diagnostic model to separate the contribution from changes in vertical velocity (dynamic contribution), temperature (thermodynamic contribution), and relative humidity to the changes in precipitation. The model shows that changes and variability in the contribution from vertical velocity determine the long-term trend and the interannual variability. We hypothesize that the changes in vertical velocity are linked to variations in storminess in the North Atlantic, which increased during the same period.

To further pinpoint the synoptic weather features responsible for precipitation, we introduced a novel method for attributing precipitation to weather features in Paper II. We attribute precipitation to cyclones, fronts, moisture transport axes (MTA, Atmospheric river-like features in the midlatitudes), and cold air outbreaks, as well as their combinations. Using the ERA5 reanalysis, we present the first global climatology of the contributions of these features to seasonal (DJF and JJA) and extreme precipitation. Most of the precipitation in the midlatitudes relates to the combination of cyclones, fronts, and MTAs (28%), while in polar regions, most precipitation occurs within the cyclone-only category (27%). Extreme precipitation events in all extratropical regions are predominantly associated with the combination of cyclones, fronts, and MTAs (46%). Moreover, in the midlatitudes, this combination of weather features occurs almost four times more often during extreme events.

In Paper III, we use the same method as in Paper II to link projected changes in precipitation to changes in weather features. We attribute precipitation to weather features in 10 ensemble members of the CESM2-LE between 1950-2100 and decompose the change into changes in intensity and frequency, as well as the contributions from the different weather features. To gain confidence in the future projections, we first evaluate how

CESM2-LE represents the current climate compared to ERA5. We find that CESM2-LE represents the precipitation associated with the different weather features and their combinations well. Projections reveal that the weather features that contribute the most to precipitation in the current climate also contribute the most to the changes in precipitation. The total frequency of precipitation is largely decreasing, whereas the intensity contributes positively to the precipitation change. Along the stormtracks, only about half of the projected intensity increase is due to an increase in the precipitation associated with the weather features, whereas the remaining precipitation is due to a shift in which weather features cause the precipitation.

In Paper IV, we shifted the focus from mean precipitation to precipitation extremes. As extreme precipitation is expected to increase more than the global mean, we quantify the changes in 6-hourly precipitation intensity for all the different weather features using the same setup as in Paper III. In the extratropics, we find that precipitation associated with fronts increases substantially more than non-frontal precipitation for the higher percentiles. This suggests that not all weather features are equally effective in converting the additional atmospheric moisture content to precipitation.

Collectively, our four studies help to connect observed and projected changes in precipitation to synoptic processes in the atmosphere. Our novel method of attributing precipitation to weather features and explicitly considering their various combinations allows for a more nuanced interpretation of the precipitation changes.

Sammendrag

Nedbør er kilden til en av de viktigste ressursene for mennesker: ferskvann. På den andre siden kan ekstremnedbør utgjøre en trussel i form av flom og skred. Det er derfor avgjørende å fastslå hvordan nedbøren har forandret seg i fortid, nåtid og fremtid, de viktigste drivkreftene bak, samt om klimamodeller simulerer nedbøren realistisk. Den globale gjennomsnittsnedbøren er forventet å øke under klimaendringer, og ekstremnedbør enda mer. Denne økningen skyldes bidrag både fra termodynamiske og dynamiske bidrag, der sistnevnte er den største kilden til usikkerhet. I de fire artiklene undersøker vi historiske og fremtidige nedbørendringer fra et prosess- og værperspektiv ved hjelp av observasjoner, reanalyse og en klimamodell.

I artikkel I bruker vi nedbørsobservasjoner fra hele Norge til å undersøke endringer i nedbør det siste århundret. Vi finner at nedbøren økte med 19% i perioden 1900-2019, hvorav nesten halvparten av økningen kom mellom 1980 og 1999. Vi bruker en enkel diagnostisk modell for å tallfeste bidragene fra endringer i vertikalhastighet (dynamisk bidrag), temperatur (termodynamisk bidrag) og relativ fuktighet til den observerte nedbørsendringen. Modellen viser at det er variasjoner i bidraget fra vertikalhastigheten som bestemmer den langsiktige trenden, i tillegg til variasjonene fra år til år. Perioden hvor nedbøren øker mest, sammenfaller hvor lavtrykksaktiviteten i Nord-Atlanteren var høy, og vi formoder at disse henger sammen.

I artikkel II forsøker vi å finne nøyaktig hvilke værfenomener som bidrar til nedbøren. Vi tilskriver nedbør til lavtrykk, fronter, fuktighetstransportakser (FTA, som likner på atmosfæriske elver på midlere breddegrader) og kaldluftsutbrudd, samt kombinasjonene av disse. Ved hjelp av ERA5-reanalysen presenterer vi den første globale klimatologien for værfenomenenes bidrag til sesong- (sommer og vinter) og ekstremnedbør. Mesteparten av nedbøren på midlere breddegrader skyldes kombinasjonen av lavtrykk, fronter, og FTA-er (28%), mens lavtrykk er viktigst i polare strøk (27%). Nesten halvparten av alle ekstreme nedbørshendelser utenfor tropene skyldes kombinasjonen av lavtrykk, fronter og FTA-er, og denne kombinasjonen forekommer fire ganger så ofte under ekstreme nedbørshendelser på midlere breddegrader.

I artikkel III bruker vi samme metode som i artikkel II for å knytte klimaframskrivninger av nedbør til endringer i værfenomener. Vi tilskriver nedbør til værfenomener i 10 ensemble-medlemmer i klimamodellen CESM2-LE mellom 1950 og 2100. For å få tillit til klimaframskrivningene evaluerer vi først hvorvidt CESM2-LE representerer dagens klima sammenlignet med ERA5. CESM2-LE representerer de unike egenskapene til de ulike kombinasjonene av værfenomenene godt. Framskrivningene viser at de værfenomenene som bidrar mest til nedbør i dagens klima, også bidrar mest til nedbørsendringene. Det blir færre antall nedbørshendelser, men intensiteten av hendelsene øker. Langs lavtrykks-

banene skyldes nesten halvparten av intensitetsforandringen at det blir flere hendelser av typen kombinasjonen lavtrykk, fronter, og FTA-er, mens intensitetsforandringen i de enkelte kombinasjonene bidrar med resten.

I artikkel IV retter vi fokus mot endringer i ekstremnedbør. Ettersom ekstremnedbør forventes å øke mer enn global gjennomsnittsnedbør, tallfester vi hvorvidt de ulike vær-fenomenene er assosiert med ulik endring i nedbørintensitet. Utenfor tropiske strøk finner vi at nedbør langs fronter øker betydelig mer en annen nedbør for de høyeste prosentilene. Dette tyder på at ikke alle værfenomenene greier å ta utbytte av det økte fuktighetsinnholdet i atmosfæren og gjøre det om til nedbør.

Samlet sett bidrar våre fire studier til å knytte historiske og fremtidige nedbørsendringer til synoptiske prosesser i atmosfæren. Vi presenterer en ny metode for å tilskrive nedbør til værfenomener. Ved eksplisitt å betrakte ulike kombinasjoner av værfenomener, bidrar vi til en mer nyansert tolkning av nedbørsendringene.

List of Publications

I. Konstali, K., Sorteberg, A., (2022) *Why has Precipitation Increased in the Last 120 Years in Norway?*, Journal of Geophysical Research: Atmospheres **127/15** <https://doi.org/10.1029/2021JD036234>

II. Konstali, K., Spensberger, C., Spengler, T., Sorteberg, A., (In press, 2023) *Global attribution of precipitation to weather features*, Journal of Climate. <https://doi.org/10.1175/JCLI-D-23-0293.1>

III. Konstali, K., Spensberger, C., Spengler, T., Sorteberg, A., (Manuscript in preparation) *Linking future precipitation changes to weather features in CESM2-LE.*

IV. Konstali, K., Spensberger, C., Spengler, T., Sorteberg, A., (Manuscript in preparation) *Atmospheric fronts drive future changes in extreme precipitation in the extratropics.*

Additional contribution

Spensberger, C., **Konstali, K.**, Spengler, T. (In preparation, 2023) *Moisture transport axes and their relation to atmospheric rivers and warm moist intrusions*

Contents

1 Introduction

1.1 The role of precipitation in the global water cycle

Every minute, approximately 1000 billion kg of water precipitate onto Earth (or 2 mm/day, Trenberth et al., 2003). Freshwater is one of the most basic resource on Earth and most of the freshwater available to humans comes from runoff after precipitation events (Boberg, 2005). Most of the evaporation that eventually leads to precipitation comes from the ocean and thus precipitation provides a net flux of freshwater from the oceans to the continents (Trenberth et al., 2003). Moreover, about 60% of the world's staple food is produced from rain-fed fields (Molden et al., 2011). As precipitation patterns may change in a changing climate, this can have profound implications for food production as well as on the world's water towers, such as the Indus, which provides freshwater for more than 235 million people (Immerzeel et al., 2020).

Not only the pattern but also the characteristics of how precipitation changes are of utmost importance. Steady moderate rain soaks into the soil and benefits plants, whereas the same amount in a short amount of time can lead to flooding and landslides (Trenberth et al., 2003). Precipitation is highly localized in time and space. In fact, it precipitates only around 8% of the time over land outside the tropics (Trenberth and Zhang, 2018) and between 40°S to 40°N half of the total annual precipitation falls within the 12 most intensely precipitating days (Pendergrass and Knutti, 2018).

Given the importance of precipitation and the possible impacts of precipitation changes, it is essential to assess its variability, its dominant drivers, and how it may change in the future as the climate changes. Precipitation has changed and will continue to change in a warmer and moister climate (Douville et al., 2023, and references therein), but there is still uncertainty associated with the change of mean precipitation patterns as a response to climate change (i.e., Chou et al., 2013).

1.2 Physical basis of precipitation change

For precipitation to occur, air must reach saturation to form droplets. Lifting an air parcel is the most effective way of cooling a parcel such that it reaches the level of condensation (Hartmann, 2016). Despite the process of forming precipitation occurring on a vast range of scales, from what happens within the individual clouds at a droplet scale ($\mathcal{O}(10^{-6})$m) to the mechanisms providing lift for air to rise ($\mathcal{O}(10^6)$ m), precipitation requires two fundamental ingredients: lift and moisture. Changes in precipitation are therefore closely dependent on changes in moisture (thermodynamic) and lift (dynamic).

The atmospheric temperature determines the upper limit of water vapour content

through the Clausius-Clapeyron (CC) relationship (Clausius, 1850). Thus, as the temperature of Earth increases, so does the atmospheric moisture content, given that the relative humidity stays constant. In that case, water vapour saturation pressure increases at roughly 7%/K (Trenberth et al., 2003). This is the same rate at which extreme precipitation is expected to increase, as extreme precipitation is constrained by low-level convergence (Allen and Ingram, 2002; Pall et al., 2007; Trenberth et al., 2003). Changes in the atmospheric water vapour content through the CC-rate are referred to as the thermodynamic contribution to precipitation change. This contribution is uniform in space and climate models show little spread, implying that climate models are rather certain about this change (Pfahl et al., 2017).

Even though the thermodynamic contribution is expected to dominate the response in extreme precipitation in the extratropics (Emori and Brown, 2005; Lu et al., 2014; Pfahl et al., 2017), the dynamic contribution can either augment or counteract the precipitation change. In O'Gorman and Schneider (2009)'s framework, the dynamic contribution changes the condensation rate. The vertical velocity can change through the frequency or location of cyclones, their associated fronts, changes in atmospheric stability, and even through changes in humidity: The increased latent heating associated with the increased moisture content of the atmosphere can invigorate the vertical velocity - but heating a layer aloft also increases the stability below the level of maximum heating, stabilizing the atmosphere. Hence, there are large uncertainties associated with the net effect of these processes, and thus the dynamic contribution towards precipitation change is uncertain (Pfahl et al., 2017).

Unlike extreme precipitation, global mean precipitation does not increase at the same rate as the water vapour content of the atmosphere. Mitchell et al. (1987) was the first to point out that the global mean precipitation increases at a lower rate and ascribed this to the constraint imposed by radiative cooling. Increasing CO_2 in the atmosphere increases the efficiency of cooling to space; and thus more latent heat can be released in the atmosphere (Mitchell et al., 1987). The energy budget has to be in balance on interannual timescales, consequently, there cannot be more latent heat in the atmosphere than what can be radiated to space. Global mean precipitation is, therefore, expected to increase between 1-3%/K (Held et al., 2006), a considerably smaller rate than the increase in atmospheric moisture content.

The different rates of changes in mean and extreme precipitation imply that the heavy and extreme precipitation must increase at the expense of the lighter-intensity precipitation (Trenberth, 2011). Thus, a warming of the atmosphere leads to a reduced frequency of precipitation and the somewhat puzzling effect of climate change on precipitation yielding simultaneously more drought and flooding.

1.3 Observed precipitation changes

The global mean temperature has increased by approximately 1K since 1850. Thus, changes in precipitation might already be visible in the observational record.

However, precipitation is difficult to measure. Not only is it very localized in space and time (it only rains 5-10% of the time Trenberth and Zhang, 2018), but collecting precipitation is also difficult, as windy conditions can lead to undercatch (i.e., droplets blow over or around the precipitation gauge rather than into it (Wolff et al., 2015)) and

changing the measuring system can lead to breakpoints in the time series (Hanssen-Bauer and Førland, 1994). Before 1950, there were few weather stations globally and only over land. Thus, determining long-term trends over larger regions, or even globally, is thus virtually impossible (Westra et al., 2013).

Precipitation changes on a regional scale are often dominated by internal variability (Knutson and Zeng, 2018). Long-term precipitation trends are mostly non-significant, except for a few regions such as Scandinavia, parts of Russia and North America, the La-Plata basin in South America, and North Australia (Douville et al., 2023).

Observations largely confirm the aforementioned notion that extremes increase more than the mean. Karl and Knight (1998) found that precipitation increased between 10% between 1910-1998 in the US and that heavy precipitation increased at the expense of the lower percentiles. Whenever there are statistically significant regional changes, the relative changes in extreme precipitation are of the same sign and are stronger than that of the mean (Easterling et al., 2000). In other regions, the mean precipitation did not change, but the extremes did (Easterling et al., 2000).

Seneviratne et al. (2023) summarized all the studies on changes in extreme precipitation between 1950-2020 and found an increase in most regions with sufficient coverage since the 1950s. Westra et al. (2013) examined changes in annual maximum daily precipitation (Rx1day) and found a positive relationship between the global mean temperature and the extreme precipitation. Although the average Rx1day intensity response largely followed the 7%/K-response (∼CC-scale), they found large spatial dependency. The tropics were the most sensitive, followed by the midlatitudes. The NH midlatitudes showed an increase of 10% per degree warming, indicating that the thermodynamics may not be the only contributor to the observed changes in extreme precipitation (Westra et al., 2013).

A quantification of the relative impact of thermodynamic and dynamic on changes in the mean precipitation is, however, missing in the literature. We use precipitation observations from Norway, which has an unusually long and complete precipitation time series due to Norway's interest in hydropower. Precipitation in Norway increased by 18% between 1900-2014 (Hanssen-Bauer et al., 2017), but both the CMIP3 and the CMIP6 models projected a considerably smaller trend than the observed one (van Haren et al., 2013; Vicente-Serrano et al., 2021). Norway is located at the end of the North Atlantic stormtrack and is thereby heavily influenced by synoptic-scale systems. In Paper I, we quantify the contribution from changes in thermodynamics and dynamics to precipitation changes between 1900-2019 in Norway. Additionally, we investigate the precipitation change in terms of frequency and intensity, as well as the changes in extreme precipitation.

1.4   The importance of weather features for precipitation

Although decomposing the precipitation change into a thermodynamic and dynamic component yields important insight into the precipitation changes, it neither provides a link to the driving mechanisms, nor to the dominant features controlling the day-to-day variability in precipitation.

Poleward of 30°, low-pressure systems in the atmosphere transport the bulk of heat and moisture to higher latitudes (Hartmann, 2016). The maximum precipitation in the midlatitudes coincides with the major oceanic stormtracks (Figure 1.1). The stormtracks

mark the climatological paths of cyclones – where cyclones are born, propagate and dissipate (Chang et al., 2002). These cyclones tend to form in the western part of the midlatitude ocean basins before moving east with the mean westerly upper-level winds. Extratropical cyclones are areas of large-scale ascent and are associated with 80% of the precipitation in the northern hemisphere midlatitudes (Hawcroft et al., 2012). These cyclones either form on existing fronts or are accompanied by fronts during much of their lifecycle (Schemm et al., 2018).

While precipitation in the Northern Hemisphere is strongest in the western margins of the North Atlantic and the North Pacific, precipitation is strong at all longitudes in the Southern Hemisphere, due to the lack of continents causing zonal asymmetries (Hartmann, 2016).

The most intense precipitation in cyclones tends to occur along their fronts, which are identified as regions of an enhanced temperature and moisture gradient (although other parameters can also be used, see Thomas and Schultz (2019) for an overview). Fronts are associated with vertical velocities, because of the sloping isentropes (lines of constant potential temperature) as well as a thermally direct circulation (warm air rises and cool air sinks) across the front, which leads to intense upward motion. Fronts contribute to more than 40% of the midlatitude precipitation, but locally up to 80% in the stormtrack region (Catto et al., 2012; Hénin et al., 2019). Additionally, the most intense precipitation is associated with the co-occurrence of cyclones and fronts (Dowdy and Catto, 2017; Pfahl and Wernli, 2012).

Low-level moisture convergence ahead of cold fronts leads to filaments of locally enhanced integrated water vapour transport, often referred to as atmospheric rivers (AR Dacre et al., 2015). ARs account for more than 90% of the meridional transport of water vapour despite covering less than 10% of the Earth's circumference (Zhu and Newell, 1998). Heavy precipitation often ensues when the AR feeds the warm conveyor belt of the extratropical cyclone or intersects with a mountain range (Gimeno et al., 2016). Consequently, ARs have received a lot of attention for their relevance for extreme precipitation in California, Antarctica, the British Isles, Western Norway, and Australia (Benedict et al., 2019; Gorodetskaya et al., 2014; Lavers and Villarini, 2013; Michel et al., 2021; Ralph et al., 2006; Reid et al., 2022).

Lastly, ETCs tend to draw cold air from the continents over the relatively warmer water, such as over the Gulf Stream in winter, leading to Cold Air Outbreaks (CAOs). CAOs also occur when very cold air flows from the sea ice over the warmer water. Because the air is so cold, these events are associated with intense air-sea heat fluxes (Papritz et al., 2015), leading to atmospheric convection and subsequent precipitation, which maximizes as the flow intersects with topography downstream (Papritz and Sodemann, 2018).

1.4.1   Case study example: Bergen November 2013

To illustrate the importance of weather features (extratropical cyclones, fronts, and ARs) for precipitation, we present the synoptic situation on 15 November 2013, when it rained 56 mm in 6 hours at Florida, Bergen. A band of precipitation associated with a front extends across the entire domain in the North Atlantic (Figure 1.2). The front is tied to an extratropical cyclone in the middle of the domain close to Iceland. A band of locally enhanced integrated water vapour transport is located on the warm side of the front, resembling the structure of an AR. The yellow line marks the line of a well-defined
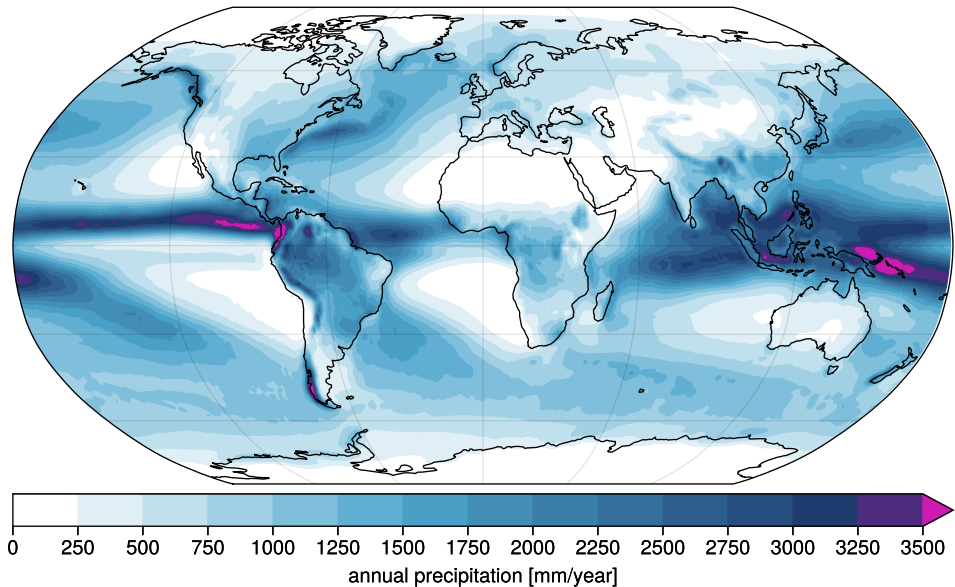
Figure 1.1: Annual mean accumulated precipitation based on ERA5.

maximum transport of water vapour, which we refer to as a moisture transport axes (Spensberger et al., 2023, Preprint).

Thus, the two ingredients for heavy precipitation are present in Western Norway: lift, generated by both the flow over topography and the front, and moisture, as indicated by the presence of an atmospheric river and the moisture transport axis. The large-scale flow is steered towards the topography of western Norway, both by the low-pressure system between Norway and Svalbard and by the anticyclone close to Great Britain. The dipole of low pressure to the north and high pressure to the south is typical for heavy precipitation events in Norway (Azad and Sorteberg, 2017). In this case, the angle of the wind, as well as the moisture transport axis, is orthogonal to the coastline and topography, providing the best conditions for lift and intense precipitation.

1.4.2 Attributing precipitation to weather features

While it has been established that precipitation in extratropical regions primarily stems from weather features, the intricate interactions between these features and their implications for precipitation characteristics remain unclear.

Fronts and ARs often accompany an ETC and the most extreme precipitation tends to be associated with the co-occurrence of cyclones and fronts (Catto and Pfahl, 2013; Dowdy and Catto, 2017). Despite the attention ARs have gained for their importance in extreme precipitation events (Benedict et al., 2019; Lavers and Villarini, 2013; Michel et al., 2021; Ralph et al., 2004, 2006; Reid et al., 2022), their relation to global mean precipitation remains unclear.

Hitherto, the methods developed to attribute precipitation to weather features rely on a radius of influence of the weather system (Catto et al., 2012; Hawcroft et al., 2012;
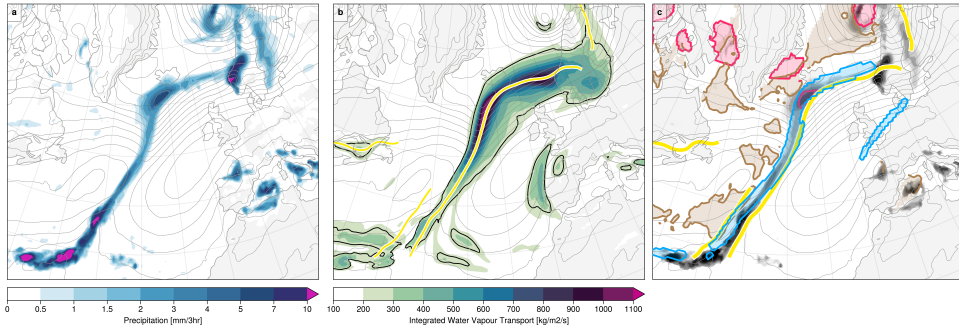
Figure 1.2: Synoptic situation leading to the 71 mm measured in Bergen during 15 November 2013 21:00 UTC. a) Precipitation in shading, mean sea level pressure in contours. b) Integrated water vapour transport in shading, yellow line marks the axis of maximum transport, a so-called moisture transport axis. The black contour marks the 250kg/m2/s-contour, a typical threshold used in atmospheric river-detection schemes. c) detected weather features, blue: fronts, yellow: moisture transport axis, cerise: ETCs, and brown: cold air outbreaks. Shading in black is the precipitation, as in a).

Hénin et al., 2019; Rüdisühli et al., 2020; Utsumi et al., 2017), rendering the method sensitive to this subjectively chosen radius. In Paper II, we introduce a new method to attribute precipitation to weather features globally, overcoming some of the challenges and limitations of the existing methods.

In addition, we include moisture transport axes, which resemble atmospheric rivers in the midlatitudes, as a weather feature in the attribution method in Paper II. We allow the features to overlap and can thus determine how the interactions of the different weather features shape the precipitation characteristics.

1.5 Projected Precipitation Changes

The global mean precipitation is projected to increase by 1.7 ± 0.6 % K^{-1} (Rehfeld et al., 2020). The relationship between global surface air temperature is known as the apparent hydrological sensitivity. The apparent hydrological sensitivity is, as previously mentioned, radiatively constrained, and is therefore quite certain (Pendergrass, 2013). However, there are large spatial variability and uncertainty, and disagreement between models on a regional scale (Chou et al., 2013).

Nonetheless, the large-scale pattern of precipitation change can be explained by the dry-get-drier-wet-get-wetter pattern, at least over the oceans (Byrne and O'Gorman, 2015). Global warming increases the water vapour content in the atmosphere, enhancing moisture convergence in the already wet regions and divergence in the already dry regions. Thus, the overall precipitation pattern in Figure 1.1 would be enhanced.

The already dry regions in the subtropics are projected to become even drier. The decreasing trend in these precipitation regions is caused by an increase in the number of dry days, which in most subtropical semi-arid regions is projected to increase markedly (10-15%, Polade et al., 2014) due to an expansion of the Hadley Cell (Laua and Kim, 2015). Poleward of 40° and in the tropics, both the change in frequency and intensity drive the future changes (Polade et al., 2014).

Many studies have decomposed the changes in extreme precipitation into changes in a thermodynamic and dynamic contributions. Lu et al. (2014) found that the scaling for the different percentiles showed the importance of circulation change in shaping the meridional structure of the change in daily precipitation. The importance of the dynamic component in explaining the regional pattern of precipitation is consistent with Pfahl et al. (2017). However, few studies have considered the impact of changing synoptic scale systems on precipitation changes.

1.5.1 Projected changes to synoptic-scale systems

Extratropical cyclones

Because the Arctic warms more than the equator at the lower levels, known as Arctic Amplification, the overall meridional baroclinicity reduces (Catto et al., 2019). The number of extratropical cyclones (ETCs) is therefore projected to decrease in both DJF and JJA in the SSP5-8.5 scenario in the NH by the end of the century (Priestley and Catto, 2022).

As the moisture in the atmosphere increases, the latent heat release also increases. This diabatic heating is thought to intensify ETCs through its effect on stratification, vertical motion, and sea level pressure (Catto et al., 2019, and references therein). Despite this possible intensification mechanism, studies have found little change in the strength of ETCs, either as measured by the maximum wind, mean sea level pressure, or vorticity (Bengtsson et al., 2009; Catto et al., 2011; Kodama et al., 2019; Yettella and Kay, 2017; Zappa et al., 2013). However, precipitation associated with ETCs is projected to increase (Bengtsson et al., 2009; Hawcroft et al., 2012; Yettella and Kay, 2017). Because the changes in the dynamical strength of the cyclone are small, most of the studies ascribe the increased ETC precipitation to changes in thermodynamic rather than dynamic changes in the ETC (Hawcroft et al., 2018; Kodama et al., 2019; Yettella and Kay, 2017).

As the atmosphere warms in the upper levels, the stability increases, which inhibits vertical velocity. Even though the background stability increases, the latent heating can also enhance the vertical motion. Tamarin-Brodsky and Hadas (2019) found that the decrease in stability from the latent heating within the most intense cyclones was stronger than the overall increase in the background stability. Priestley and Catto (2022) found that the upper-level divergence increased in cyclones, most likely associated with an increase in the vertical velocity of the cyclone. The maximum increase in divergence occurred in the warm sector of the cyclone, with a smaller decrease in the convergence behind the cold front, associated with subsidence, indicating an increased asymmetry of the vertical velocities in future cyclones (Priestley and Catto, 2022), consistent with the findings of Tamarin-Brodsky and Hadas (2019). The asymmetry of the vertical motions is expected to intensify in a warmer climate, which could locally enhance precipitation beyond the CC-scaling (Tamarin-Brodsky and Hadas, 2019).

Fronts

Fronts are an important feature of extratropical cyclones, but their changes have been considerably less studied than changes in ETCs. CMIP5 models project the number of fronts over large parts of the NH to decrease (Catto et al., 2014), while frontal activity is expected to increase over the Southern Ocean (Blázquez and Solman, 2018). However,

the combination of decreased front frequency in the future together with an increased amount of precipitation associated with ETCs implies an intensification of the front-associated precipitation intensity, or a shift of the precipitation within the cyclones to a more central part of the cyclone (Catto et al., 2019).

Intense fronts tend to precipitate more intensely than weak fronts (Schemm et al., 2017), with frontal intensity measured as the strength of the equivalent potential gradient across the front. A thermally direct circulation across the front acts to concomitantly strengthen the frontal intensity and differential diabatic heating, which further strengthens the cross-frontal circulation and the frontal intensity through a positive feedback loop (Eliassen, 1962). Observations suggest that the frontal intensity and precipitation have increased since 1979, particularly over the North Atlantic and Europe, which has been attributed to the moisture increase (Schemm et al., 2017).

Atmospheric Rivers

Atmospheric rivers are projected to increase in both frequency of occurrence as well as in their areal extent (O'Brien et al., 2022). However, as ARs are often defined more qualitatively rather than quantitatively, several different AR detection and tracking algorithms (ARDTs) exist (see i.e., Lora et al., 2020; Rutz et al., 2019, for an overview). Thus, evaluating changes in ARs yields highly uncertain results, as the spread across different ARDTs in the AR frequency trend far surpasses the uncertainty across climate models (Shields et al., 2023).

The uncertainty associated with the ARDTs also encompasses the projected changes in the bulk precipitation characteristics associated with ARs (Shields et al., 2023). The spread of values across the ARDTs under the RCP8.5 scenario falls within the historical spread. Thus, the choice of ARDT largely determines the associated trend (Shields et al., 2023).

Nonetheless, some studies have attributed the projected precipitation to changes in atmospheric rivers. For example, Gershunov et al. (2019); Rhoades et al. (2020) found that the precipitation delivered by land-falling atmospheric rivers on the West Coast of the United States is projected to increase with climate change. In addition, most of the frequency of the heavy precipitation events could be linked to an increase in the frequency of ARs, while the non-AR storms changed little (Gershunov et al., 2019).

1.5.2 Linking projected precipitation changes to weather features

To get a physical link between the projected changes in precipitation and the driving mechanism, we attribute precipitation to weather features between 1950-2100 in a climate model. Attributing precipitation to weather features in a climate model may, in addition, provide a more physical understanding of the precipitation biases.

There are still large biases associated with the intensity and frequency of precipitation in climate models, although the total precipitation is relatively well represented (Ahn et al., 2023; Pendergrass, 2013; Stephens et al., 2010). These biases may limit the usefulness of future projections (Trenberth et al., 2003). To have confidence in future projections of precipitation in the midlatitudes, it is imperative that climate models adequately simulate the current precipitation characteristics associated with the different features (Hawcroft et al., 2018).

Catto et al. (2015) showed that the frontal frequency as well as the frontal precipitation was quite well simulated in the CMIP5 models in the Southern Ocean; and Hawcroft et al. (2018) showed that a high-resolution climate models did simulate the precipitation associated with extratropical cyclones adequately. In Paper III, we add to these type of analyses by considering more weather features (ETCs, fronts, moisture transport axes, and cold air outbreaks) and assessing whether CESM2 can simulate the precipitation characteristics associated with the different weather features.

Investigating precipitation change from a weather perspective reveals a direct, physical link between the precipitation changes and the mechanism governing it. Thus, it provides an easily interpretable mechanism for future precipitation changes. Although some studies have considered the changes in cyclones (Hawcroft et al., 2018), fronts (Blázquez and Solman, 2018; Catto et al., 2015), or atmospheric rivers (Gershunov et al., 2019), few studies consider the co-occurrence of weather features. We address this gap in Paper III, where we investigate the relevant weather features for precipitation change and decompose it into changes in intensity and frequency. In Paper IV, we further complement the analysis by investigating the changes in precipitation across the precipitation distribution.

1.6 Objectives

In short, we aim to answer the following research questions in this thesis through four papers:

- What were the relative roles of the thermodynamic and dynamic contribution in shaping the observed precipitation increase in Norway over the past 120 years?

- How do precipitation characteristics vary in association with different weather features?

- Are climate models able to represent the precipitation characteristics associated with the different weather features and their combinations?

- Which weather features contribute most to the projected precipitation changes?

- How does the precipitation associated with the different weather features respond to climate changes?

2 Data

2.1 Observations

Precipitation is difficult to measure because it is highly localized in both time and space. In the first paper, we use observations of daily accumulated precipitation between 1900-2019 from The Norwegian Meteorological Institute. The data set is quality-controlled and has 200 stations all over Norway, of which 55 stations have measured since 1900. For details on the additional quality control and homogeneity testing, we refer the reader to Paper I.

2.2 Reanalysis

A reanalysis takes a state-of-the-art numerical weather prediction model and blends short-term forecasts with observations. Assimilating the observations into the short-term forecasts makes sure that the state of the atmosphere matches that of observations well. In this thesis, we use three different reanalysis products: The European Centre for Medium-Range Weather Forecast's (ECMWF) 20th-century reanalysis (ERA-20C, Poli et al., 2016), and ERA5 (Hersbach et al., 2020), as well as the National Ocean Atmosphere Administration's (NOAA) 20th-century reanalysis version 3 (20CRv3, Slivinski et al., 2019).

Both ERA-20C and 20CRv3 are twentieth-century reanalyses, meaning that they provide data output all over Earth for all of the twentieth century. Because of a rather limited observational network before 1950, and the satellite era (from 1979 and onward), these reanalyses only assimilate surface pressure. ERA-20C assimilates marine winds in addition. Because of their different assimilation techniques, ERA-20C is expected to work better over areas with good observational coverage, while 20CRv3 may use the sparse observations better and provide better estimates in the Southern Hemisphere or in the high latitudes (Poli and National Center for Atmospheric Research Staff, 2022). However, neither of these two reanalyses provide the best-state-atmosphere since 1979 and they may be associated with spurious trend associated with changes in the observing system, and the manyfold increase of observations assimilated into the reanalysis.

ERA5, on the other hand, assimilates all observational products available and provides the best estimate of the atmosphere after 1979. Although there are some precipitation biases associated with the reanalysis, it represents the precipitation in the extratropics well (Lavers et al., 2022).

2.3 CESM2-LE

The Community Earth System Model version 2 (CESM2, Danabasoglu et al., 2020) is part of the Coupled Model Intercomparison Project Phase 6 (CMIP6) and was developed at the National Center for Atmospheric Sciences (NCAR). In Paper III and Paper IV, we use the output from 10 ensemble members from the CESM2 Large Ensemble (CESM2-LE, Rodgers et al., 2021), between 1950 and 2100. These members are stored with high-frequency output and more atmospheric variables to facilitate regional climate models run, and correspond to the macro-perturbation runs initialized at $1011, 1031, 1051, ..., 1191$.

CESM2-LE follows the historical and SSP3-7.0 forcing protocols as recommended by O'Neill et al. (2016) and has a $1°$ horizontal resolution. The 10 members we use differ slightly from CMIP6 in their biomass burning protocol, which is smoothed using an 11-year temporal average to avoid the interannual variability due to the inclusion of new observations of biomass burning (Rodgers et al., 2021).

3 Summary of the papers

Paper I: **Why has precipitation increased in the last 120 years in Norway?**

We investigated precipitation changes in Norway using rain gauge measurements between 1900-2019. Observations show that both mean and extreme precipitation increased during this period. The bulk of the increase occurred between 1980-1990, but continued to increase, albeit at a slower rate, in the 2000s. We use a modified version of the precipitation scaling developed by O'Gorman and Schneider (2009) to decompose the precipitation change into contributions from changes in vertical velocity (dynamic), temperature (and subsequent moisture, thermodynamic), and relative humidity. For this analysis, we used output from two century reanalyses, 20CRv3 and ERA-20C. The reconstructed precipitation based on vertical velocity, temperature, and relative humidity matches the annual precipitation record in Norway well. Based on these findings, we argue that the changes in the 1980s were dominated by changes in vertical velocity, whereas changes since the 2000s were mainly due to temperature changes. We hypothesize that the increased contribution from vertical velocity in the 1980s is most likely caused by increased storminess in the North Atlantic in the same period.

Paper II: **Global attribution of precipitation to weather features**

In Paper II, we identify fronts, cyclones, moisture transport axes, and cold air outbreaks globally in ERA5. We then attribute precipitation to these weather features, as well as their combinations at all latitudes, using a novel attribution method. This new method proves to be more robust compared to previous methods in terms of sensitivity to subjective choices of, for example, distance thresholds. We classify more than 70% of the precipitation globally and present their average precipitation intensities for DJF and JJA. Within the stormtrack regions, we find that most precipitation occurs when extratropical cyclones, fronts, and moisture transport axes co-occur. Moreover, when cyclones, moisture transport axes, and fronts co-occur, precipitation is most intense on average and associated with the bulk of extreme precipitation events in the extratropics.

Paper III: **Linking precipitation changes to weather features**

In Paper III, we investigate whether climate models (here represented by CESM2-LE) can be a tool to investigate future changes in precipitation from a weather perspective. We use the same method as in Paper II and attribute precipitation to weather features across 10 ensemble members in CESM2. We compare the occurrence and positions of weather features, as well as the precipitation distribution associated with the different weather features. Overall, we find CESM2 to adequately represent both the weather features and the associated precipitation distribution in the current climate.

We find that the decreasing precipitation trends were mainly caused by a decrease in frequency, whereas the intensity mainly contributed positively to the change. The precipitation categories that contribute the most to precipitation in the current climate also tend to have the largest change. Along the stormtracks, the co-occurrence of cyclones, fronts, and moisture transport axes contribute the most to the change in total precipitation. As this is the most intensely precipitating category in the present climate, an increased contribution could lead to an intensification of the total precipitation, without the precipitation categories themselves becoming more intense. We find this effect to be responsible for roughly half of the intensity increase in the stormtrack regions.

Paper IV: **Fronts drive future changes in extreme precipitation**

Different weather systems may respond differently to global warming, with the possibility of changing their precipitation characteristics dramatically. In Paper IV, we investigate the change in precipitation intensity associated with different weather features in 10 ensemble members in CESM2-LE across the entire precipitation distribution. We find that extreme precipitation associated with fronts increased substantially more than the non-frontal precipitation. The frontal extreme precipitation increases close to, or exceeds the Clausius-Clapeyron scaling, suggesting altered frontal circulation dynamics may enhance future precipitation extremes.

4   Conclusions and outlook

This thesis explores the relationship between the two most vital ingredients of precipitation – lift and moisture – using observations, reanalyses, and a climate model. We used observations and reanalyses in Paper I and decomposed the precipitation changes into changes in vertical velocity, relative humidity, and temperature. In the other three papers, we used a weather feature framework to investigate the roles of weather features in shaping the current pattern of precipitation as well as projected changes in precipitation.

In the introduction, we defined the following research questions:

What were the relative roles of the thermodynamic and dynamic contribution in shaping the observed precipitation increase in Norway over the past 120 years?

In Paper I, we found that we were able to reconstruct the annual observed precipitation between 1930-2010 using vertical velocity, relative humidity, and temperature. We found that the dynamical component (changes in vertical velocity) was crucial for shaping the long-term and interannual variability in precipitation in Norway. The importance of the dynamic contribution and the shift occurring in the 1980s are potential reasons why CMIP3 and CMIP6 models underestimated the observed precipitation trends (van Haren et al., 2013; Vicente-Serrano et al., 2021). The precipitation increase and the changes in vertical velocity increased simultaneously as increased storminess in the North Atlantic (Chang et al., 2003), but we lacked the tools to explicitly link the vertical velocity and the atmospheric circulation.

How do precipitation characteristics vary in association with different weather features?

Seeking to directly and robustly link precipitation to weather features, we introduced a novel and more robust attribution method in Paper II. We attributed precipitation to cyclones, fronts, moisture transport axes, cold air outbreaks, and combinations thereof in ERA5 between 1979-2020. Precipitation in the current climate is strongest when multiple features co-occur (cyclones, fronts, and MTAs), a category which indicates both strong dynamic forcing and an abundance of moisture. This category contributes most of the precipitation along the stormtracks and occurs four times as often during extremes than during wet events in the extratropics. On the other hand, precipitation attributed to single weather features or without weather features present is associated with relatively weaker precipitation.

Where most previous studies considered features in isolation (Catto et al., 2012; Hawcroft et al., 2012; Hénin et al., 2019), or split the precipitation between overlapping features evenly (Utsumi et al., 2017), we allow for combinations of features. Introducing multiple

weather features and allowing them to overlap yields a more refined interpretation of the precipitation characteristics and makes it possible to infer the relative contributions to lift and moisture.

Are climate models able to represent the precipitation characteristics associated with the different weather features and their combinations?

That weather features and associated precipitation are well represented in the current climate is imperative to have confidence in future projections of precipitation (Hawcroft et al., 2018). However, few studies have addressed how weather features and their associated precipitation characteristics are represented in climate models. In Paper III, we showed that CESM2 adequately reproduces the precipitation characteristics associated with the different combinations of weather features. The precipitation intensity is underestimated in all categories, pointing toward a systematic bias. In addition, the different categories contribute approximately equally to the total precipitation in CESM2 and ERA5, indicating that CESM2 does precipitate for the right reasons. Thus, the state of precipitation in the latest generation of climate models may not be as "dreary" Stephens et al. (2010) as thought.

Which weather features contribute most to the projected precipitation changes?

While several studies have investigated precipitation changes associated with ETCs, few studies have considered multiple weather features, which is particularly important as the most intense precipitation in an ETC tends to occur along the frontal zones. In Paper III, we found that precipitation associated with the co-occurrence of cyclones, moisture transport axes, and fronts is projected to contribute relatively more to future extratropical precipitation. This increase is to a large extent driven by an increase in frequency. Thus, although the number of cyclones is projected to decrease (Catto et al., 2019, and references therein), cyclones that do occur are more likely to be accompanied by fronts and moisture transport axes.

Precipitation associated with the co-occurrence of cyclones, moisture transport axes, and fronts is the most intensely precipitating category. Hence, when this category contributes more to the total precipitation, it could lead to a trend in the intensity of the total precipitation. Thus, the projected increase in precipitation intensity could be the result of the more intensely precipitating categories occurring more often rather than the different categories becoming more intense. In Paper III, we quantified this effect and found the combined category to contribute up to 50% of the total precipitation intensity increase in the stormtracks.

How does the precipitation associated with the different weather features respond to climate change?

The precipitation characteristics associated with the different weather features respond distinctly to climate change. While some categories show an increase in their mean intensity, other categories decrease. In Paper IV, we assessed changes in precipitation beyond only considering changes in the mean precipitation and considered changes across the entire precipitation distribution. Categories involving fronts increase at rates close to the CC-rate for extreme precipitation, whereas the change in non-frontal precipitation is similar for both extreme and mean precipitation. Thus, we argue that it is mainly

fronts that are associated with sufficiently strong dynamic forcing to take advantage of the additional moisture in the atmosphere and convert it into precipitation.

Concluding remarks

Attributing precipitation to weather features provides a physical link between precipitation and its governing mechanisms. This connection can further be exploited to connect weather features, occurring on shorter time scales, to long-term climatic changes. Using weather features to understand climate change facilitates a more nuanced understanding of how specific atmospheric processes contribute to broader climate patterns.

In synthesis, this thesis highlights the subtle interplay of lift and moisture in shaping precipitation patterns and changes. Although the dynamic contribution to precipitation in the extratropics is deemed small, we found it crucial both for the long-term precipitation trend in Norway and in determining whether the features can exploit the increased atmospheric moisture content. The findings not only enhance our understanding of current precipitation patterns, but also offer valuable insights into the potential implications of a warmer and moister future climate for precipitation characteristics. However, perhaps most importantly, we find that CESM2, despite some biases, represents the precipitation characteristics surprisingly well, boosting our confidence in climate projections.

4.1 Outlook

Using concepts from synoptic meteorology to understand larger-scale patterns and changes, enables several interesting avenues of research.

In Paper I, we concluded that the dynamic component was the primary driver for the observed precipitation trend. Both ERA-20C and 20CRv3 represented the precipitation and the atmospheric circulation well after 1930. Thus, it is a possibility to link precipitation changes in Norway to changes in weather features. Combining this with historical climate model output could help determine why none of the CMIP6 models were able to reproduce the observed precipitation trends in Northern Europe (Vicente-Serrano et al., 2021).

Although only briefly touched upon in Paper III, we believe there is unexplored potential in investigating precipitation biases in climate models from a weather perspective. In Paper III, we linked the frequency bias to a frequency bias of CAOs in the North Atlantic and subsequently to the SST bias. In addition, the absence of a well-defined Great Plains Low-Level Jet (also briefly touched upon in Paper III) may link to the dry and warm bias over the Great Plains (Lin et al., 2017). Precipitation in this region tends to be associated with mesoscale convective systems (MCS, Feng et al., 2019). In Paper II, we found that most precipitation over the Great Plains in JJA was associated with moisture transport axes and fronts, indicating the importance of synoptic-scale systems in providing a favourable environment for convection. Errors in moisture transport could point to errors beyond that of poorly parameterized convective systems in climate models.

While the selection of weather features in Paper II makes for a good attribution in the extratropics, it does not distinguish between different precipitation types in the tropics. In the tropics, the main driver of precipitation are convective instability and MCS, which we do not capture in our attribution. These convective instabilities further

interact with the large-scale environment, such as equatorially coupled convective waves (Cheng et al., 2023), and lead to relatively enhanced precipitation in some locations. Over continents in summer, MCSs interact with synoptic-scale features. Thus, including MCSs would not only enhance the attribution in the tropics but also over land. Analyzing the interaction between convection, either in the form of MCS or more locally forced events, and synoptic-scale features is lacking in our analysis and provides a possible future research avenue.

Lastly, the physical mechanism of why some precipitating categories precipitate more intensely than others requires analysis beyond the scope of this thesis. Ultimately, understanding the interactions between features and how they relate to precipitation would help interpret future changes in precipitation. Using metadata, such as the strength of the features, could be one way of trying to separate the events further. Another possibility could be to adopt a Lagrangian approach to the features and consider their temporal evolution. Perhaps cyclones without fronts and moisture transport axes precipitate weakly simply because they have started their cyclolysis.

5 Scientific results

Paper I

Why has Precipitation increased the last 120 years in Norway?

K Konstali and A Sorteberg

JGR Atmospheres

Key Points:

- Precipitation has increased by more than 19% over the last 120 years in Norway
- We decompose changes in precipitation into changes in thermodynamics and dynamics
- Vertical velocity is the dominant driver for interannual variability in precipitation in Norway

Correspondence to:

K. Konstali,
kjersti.konstali@uib.no

Why has Precipitation Increased in the Last 120 Years in Norway?

K. Konstali[1,2] and **A. Sorteberg[1,2]**

[1]Geophysical Institute, University of Bergen, Bergen, Norway, [2]Bjerknes Center for Climate Research, Bergen, Norway

Abstract We use a data set with daily precipitation observations from 55 homogeneity-tested stations in Norway from 1900 to 2019 available from MET-Norway. These observations show that precipitation in Norway has increased by 19% since 1900. Notably, over half of the overall increase occurred within the decade of 1980–1990 and is happening across all precipitation rates. To examine possible mechanisms behind the precipitation increase, we use a diagnostic model to separate the effects of changes in vertical velocity, temperature and relative humidity. We use daily vertical velocity, near-surface temperature and relative humidity from two reanalysis products, ERA-20C and 20th Century Reanalysis. The model-based precipitation correlates significantly with the observed precipitation on an annual timescale ($r > 0.9$), as well as captures the trend in all reanalysis products. The diagnostic model indicates that the variability in vertical velocity chiefly determines the interannual variability and long-term trend. The trend in vertical velocities contributes to more than 80% of the total modeled trend in precipitation between 1900 and 2019. However, over the last two decades (1995–2015), changes in temperature and relative humidity are the main contributors to the modeled trend in precipitation.

1. Introduction

Norway is located at the end of the North-Atlantic storm track and is thus warmer and wetter than the average climate at the same latitude, as cyclones transport heat and moisture poleward. Between 1900 and 2014, precipitation in Norway has increased by more than 18% (Hanssen-Bauer et al., 2017). Furthermore, Northern Europe is one of the few regions globally where there is high confidence that human influence has contributed to the observed changes in extreme precipitation (Seneviratne et al., 2021). Precipitation is expected to increase in Europe with continued warming (Seneviratne et al., 2021), and the relative change in extreme precipitation is expected to increase faster than the mean (Kharin et al., 2007; Myhre et al., 2019; Sillmann et al., 2013). Knowledge is currently lacking on how precipitation extremes have changed in Norway, on the changes in precipitation characteristics, and a discussion of possible mechanisms behind the precipitation increase. To close this gap, we analyze an extensive station network with data from 1900 and provide an updated and consistent view of mean and extreme precipitation changes. Furthermore, we examine possible mechanisms behind the precipitation variability and link it to thermodynamic and dynamic changes using a diagnostic model to decompose the observed changes into contributions form vertical velocity, temperature, and relative humidity.

Precipitation is expected to increase in a warmer climate because higher temperatures are related to increased precipitation through moisture availability. If the relative humidity is constant, the atmosphere's moisture content scales directly with the saturation vapor pressure, which increases with rising temperatures (Clausius, 1850). At our current temperature, this means an increase in atmospheric water vapor content of approximately 7% K^{-1} (Trenberth et al., 2003). The thermodynamic contribution to extreme precipitation change is well understood and positive everywhere (Pfahl et al., 2017), and it can also be interpreted as the maximum amount the mean precipitation can increase at a regional level if the relative humidity and upward vertical velocity are constant. However, this effect is insufficient to explain the observed precipitation increase in Norway; while the temperature in Norway has increased by 1 K, precipitation increased by 18% (Hanssen-Bauer et al., 2017).

Thus, we must consider the dynamic changes in addition to the thermodynamic changes. Atmospheric circulation and associated vertical velocities comprise the dynamic component. This component is one of the major sources of uncertainty in climate models (Shepherd, 2014), and even the sign of the dynamic contribution to precipitation change differs between climate models in the same region (Pfahl et al., 2017; Seneviratne et al., 2021). The historical simulations of both CMIP6 and CMIP3 models produced considerably smaller trends in precipitation

in Northern Europe than observed in the last century (van Haren et al., 2013; Vicente-Serrano et al., 2021). However, some pf the CMIP6 models are able to capture the observed trend in the second half of the century (Vicente-Serrano et al., 2021). van Haren et al. (2013) linked the trend bias in CMIP3 to the circulation and sea surface temperature trend biases in the models' boundary conditions. As synoptic scale features, such as atmospheric rivers and extratropical cyclones (ETCs), are responsible for most extreme precipitation events in coastal Norway (Azad & Sorteberg, 2017; Benedict et al., 2019; Heikkilä & Sorteberg, 2012; Michel et al., 2021), dynamic changes have likely played a substantial role in changing the precipitation in the past.

Although thermodynamics' and dynamics' contributions to extreme precipitation changes are widely discussed, no studies have, to our knowledge, quantified the thermodynamic and the dynamic contributions to the observed mean precipitation increase over longer timescales using a physical diagnostic. Previous studies have quantified the thermodynamic and dynamic contributions to modeled extreme precipitation changes in the future (Pfahl et al., 2017; Tandon et al., 2018), changes in extreme precipitation over India between 1979 and 2019 (Ali & Mishra, 2018), and record-events of short timescales in the past (Oueslati et al., 2019). We adopt a similar framework to decompose the changes in mean precipitation into changes in thermodynamics and dynamics. We use a simplified model of precipitation that assumes pseudoadiabatic ascent and estimate the precipitation in Norway between 1900 and 2019 based on temperature, vertical velocity, and relative humidity. The method then allows us to decompose changes in precipitation into contributions from these three variables.

Although changes in precipitation in Norway have previously been investigated (e.g., Hanssen-Bauer, 2005; Hanssen-Bauer et al., 2017; Hanssen-Bauer & Førland, 1998; Hanssen-Bauer & Førland, 2000), there is currently no peer-reviewed literature on the topic. The most updated view on the trends used a monthly gridded data set (Hanssen-Bauer et al., 2017), and the interpolation uncertainties associated with such gridded precipitation datasets can be much larger than the uncertainties associated with measuring precipitation itself (Haylock et al., 2008). We avoid the interpolation uncertainties using the observations directly, although there may be issues of homogeneity in long precipitation time series (Hanssen-Bauer & Førland, 1994). In addition, none of the studies have considered changes in extreme precipitation in Norway since 1900. We aim to complement the existing literature on seasonal and annual mean changes by providing an updated view of the annual mean to daily extreme precipitation trends using daily observations over the last 120 years.

2. Data and Methods

2.1. Observations and Quality Control

We use observations of daily accumulated precipitation from The Norwegian Meteorological Institute. The data set is quality-controlled and has more than 200 stations all over Norway.

To select appropriate stations for our study, we check for sufficient data coverage in addition to homogeneity. For the data coverage, we require that the stations have less than 25% of the data missing between 1961 and 1990. Because some stations have changed location over the past 120 years, we merge data from stations closer than 4 km if the altitude difference is less than 100 m to get a longer continuous time series from the stations. We correct the shortest time series by multiplying it with the systematic bias, defined as the ratio of the longest to the shortest time series, if at least a 2 year data overlap exists. The results did not change much depending on a 2 or 4 radius, but for an 8 km radius, the bias between the stations became substantially larger. The strict 100 m altitude difference was important to avoid merging a valley station with a mountain station. Then, to assure that a change of location, measuring technique, a merging of a station, or similar, have not artificially induced a trend in the time series, we check for breakpoints with a homogeneity test. The homogeneity test is a penalized maximum F-test (RHv4 Wang, 2008a; 2008b). If a breakpoint is detected within the time series at a 5% significance level, we remove the station from the record. Lastly, we visually inspect the time series and the remaining non-significant breakpoints. If a breakpoint is detected close to a station merging, or if the time series differ substantially from neighboring stations, we also remove these stations. The station metadata is available in Table S2 of Supporting Information S1.

Due to a shift in the number of stations in the late 1950s, we focus on two different periods: 1900–2019 and 1960–2019. In the time series starting in 1900, 69 stations meet the data coverage criteria. However, 14 of these did not pass the quality control, leaving 55 stations, of which 15 are merged with a neighboring station. Nearly all the stations are located in Southern Norway (Figure 1), while the two northernmost regions in Norway only
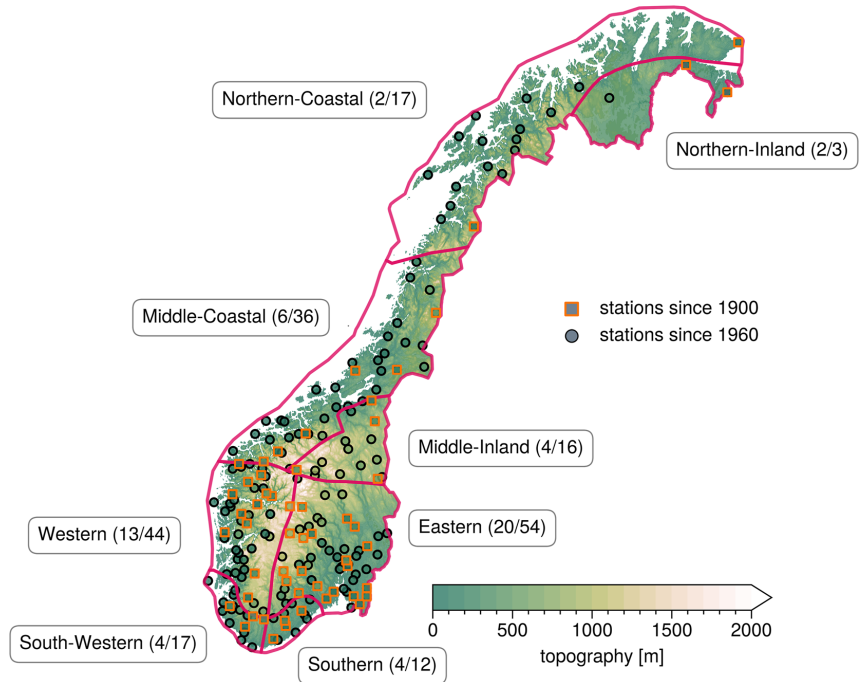
Figure 1. Map of Norway showing precipitation stations and the regions used in this study. Circles mark stations in the short time series and squares stations in the long time series. Colors indicate elevation. The numbers shown after the region names represent the number of stations available in the region from 1900 to 1960.

have two stations each. In the time series starting in 1960, 229 stations meet the data coverage criteria. Of these, 199 passed the quality control, and 64 stations were merged with a neighboring station. Despite the increase in the number of stations, most of them are still located in Southern Norway and at low elevations. We will refer to the aforementioned time-series of precipitation as OP1900 and OP1960, respectively.

We use the same precipitation regions as Michel et al. (2021), as shown in Figure 1. We refer to South-Western, Western, Middle-Coastal, Northern-Coastal, and Southern as coastal regions, and Middle-Inland, Northern-Inland and Eastern as inland, based on their seasonality characteristics of precipitation.

To calculate mean statistics for Norway, we weigh all regions equally regardless of area. This averaging method gives a bias toward Southern-Norway, where the regions are more numerous and smaller than the regions in Northern-Norway. However, the relative trend calculated for Norway of annual accumulated precipitation is almost insensitive to the choice of averaging methods (weighing all stations equally, weighing all regions equally, and weighing regions by area), differing only by 0.6%. We ignore the missing data and use only the existing values when we calculate the means for the individual stations. If the number of missing days exceeds 10% in a month, the monthly value for the station is assigned as missing.

2.2. Reanalyses

We use two reanalyzes products that provide global atmospheric data since 1900; European Centre for Medium-Range Weather Forecasts' (ECMWF) twentieth-century reanalysis, ERA-20C (Poli et al., 2016) and National Oceanic and Atmospheric Administration's (NOAA) Twentieth century Reanalysis version 3, 20CRv3 (Slivinski et al., 2019). Both are available on a 1° latitude × 1° longitude grid and at a 3 hourly temporal resolution. ERA-20 C has 91 vertical levels between the surface and 0.01 hPa, while 20CRv3 has 28 vertical levels from

the surface to 1 hPa. They both assimilate surface pressure, but ERA-20C assimilates marine winds in addition. For comparison and reference, we use ERA5 from ECMWF (Hersbach et al., 2020). ERA5 is available from 1979 to the present on a 30 km grid and has 137 levels in the vertical and an hourly temporal resolution.

We select 2 m temperature, dew point temperature or relative humidity, depending on availability, and vertical velocity in pressure coordinates from all available levels between 1,000 and 200 hPa at 12:00 UTC. We use the reanalyzes at 12:00 UTC because there are more observations assimilated at this time step, particularly in the early part of the century (Cram et al., 2015).

2.3. Trend Analysis

We use the non-parametric Mann-Kendall test (Mann, 1945) to detect statistically significant trends in the time series. Because the test does not assume a distribution of the data, it is commonly used to detect trends in both mean and extreme precipitation (e.g., Alexander et al., 2006; Westra et al., 2013; Wu et al., 2016). If a trend is present in the time series, we use Sen's slope estimator (Sen, 1968) to calculate the magnitude of the trend. Note that "significant" refers to statistically significant at the 95% confidence level throughout the paper unless otherwise stated.

2.3.1. Trend Analysis for Extreme Events

To determine the trend of different quantiles, we performed quantile regression on daily precipitation for each station following the method from Koenker and Hallock (2001). The advantage of using quantile regression compared to standard linear regression is that the quantile regression can estimate changes in all parts of the distribution rather than just the mean. While standard linear regression entails minimizing the sum of squared errors, quantile regression involves minimizing a weighted average of the absolute errors (Tareghian & Rasmussen, 2013). Several studies have used quantile regression to look at changes in extreme precipitation (e.g., Bohlinger & Sorteberg, 2018; Fan & Chen, 2016).

Rarer events, such as annual maxima, follow a Generalized-Extreme-Value (GEV) distribution and can thus be described with three parameters: location (μ), scale (σ), and shape (ξ). To determine whether trends are present in the annual maxima precipitation, we introduce time as a covariate to the location parameter, $\mu = \mu_0 + \mu_1 t$, where t is time. If the distribution with a varying location parameter is a better fit than a stationary location parameter according to a maximum-likelihood test with a 95% confidence level, we say that there is a significant trend in the annual maximum. Knowing the change in the location parameter allows us to calculate changes in both magnitude and return period for rare events, for example, 100 year events. We only used the stations available since 1900 to minimize the uncertainty in the calculated return values because the GEV distribution is highly sensitive to the record length (Hu et al., 2020). We use the extRemes software package, written in the statistical software language R (Gilleland & Katz, 2016), for extreme value analysis.

2.4. Diagnostic Model: Estimating Precipitation Based on Pseudoadiabatic Ascent

To relate trends in the observed precipitation to dynamically or thermodynamically induced changes, we use a diagnostic model based on moist pseudoadiabatic ascent. A similar formulation has been used by Sinclair (1994), Collier (1975), and Kunz and Kottmeier (2006) to model orographic precipitation. However, instead of using orographically induced velocity, we use the vertical velocity from reanalysis. We assume that all condensate precipitates out immediately and that no precipitation evaporates on the way down. Integrating the total condensate from the lifting condensation level to the top of the troposphere then yields the precipitation generated by the moist-pseudoadiabatic ascent, PAP, as formulated in Haltiner and Williams (1980, pp. 309–310):

$$PAP = \frac{\lambda_{RH}}{g} \int_{p_{LCL}}^{p_{top}} \delta_m \frac{q_s T}{Rp} \left(\frac{L_v R - c_p R_v T}{c_p R_v T^2 + q_s L_v^2} \right) \omega(p) dp \ . \tag{1}$$

In Equation 1, p_{LCL} and p_{top} are the pressure of the cloud base and 200 hPa, respectively. q_s is the saturation mixing ratio, ω is the vertical velocity in pressure coordinates, which is a function of pressure (p), T is temperature, R and R_v are the ideal gas constants for dry air and moist air, respectively, and L_v is the latent heat of vapourization. δ_m is the Heaviside function which is 1 if the vertical velocity is upward and 0 otherwise and is evaluated at all levels. To avoid precipitation in unsaturated conditions but account for that part of the grid cell may be

saturated even if the average RH is below saturation, we introduce the RH-threshold parameter, λ_{RH}. λ_{RH} is 1 if RH > RH_c and 0 otherwise. RH_c is a critical relative humidity, set to 0.75 in every grid point, which according to Quaas (2012) is representative of pressure levels below 900 hPa over Europe as well as close to the mean global value at 1,000 hPa. For simplicity, we set the cloud base as the lifting condensation level, where air reaches saturation with a dry-adiabatic ascent from 1,000 hPa, estimated from the 2 m temperature and the 2 m relative humidity. Although keeping the sea level pressure constant is a simplification, we find the effect negligible as the results differ with <0.5%. Within the cloud, we assume the air is saturated and that the temperature follows the moist-adiabatic lapse rate.

Equation 1 shows that precipitation depends on the upward vertical velocity inside the cloud and indirectly on the 2 temperature and 2 m relative humidity, which affect the level of condensation, and thus the temperature within the cloud. We integrate all the levels with upward vertical velocity from the level of condensation to 200 hPa, where 200 hPa approximates the top of the troposphere.

2.4.1. Separating the Effects of Changes in Vertical Velocity, Temperature, and Relative Humidity

To separate the contribution from changes in vertical velocity, temperature, and relative humidity to the long-term trend in precipitation, we decompose Equation 1. First, we construct a seasonal mean based on data from each day from all the years for the three variables at all pressure levels in a grid cell. Thereafter, we smooth the mean using a running 25 day average. The seasonal cycle of the vertical velocity is constructed from days with upward motion only at each pressure level. We then allow one term to vary on a daily timescale while keeping the seasonal cycle of the two other terms constant;

$$PAP \approx P_\lambda + P_{T^*} + P_{\omega^*}$$

$$= \lambda_{RH} \int_{p_{LCL}}^{p_{top}} [T^*] [\omega^*(p)] \, dp + [\lambda_{RH}] \int_{p_{LCL}}^{p_{top}} T^* [\omega^*(p)] \, dp + [\lambda_{RH}] \int_{p_{LCL}}^{p_{top}} [T^*] \omega^*(p) \, dp$$

(2)

where T^* is $\frac{q_s T}{R p} \left(\frac{L_v R - c_p R_v T}{c_p R_v T^2 + q_s L_v^2} \right)$, ω^* is $\delta_m(p)\omega(p)$, and the square brackets denote the smoothed average seasonal cycle. P_λ, P_{T^*}, and P_{ω^*} thus represent the precipitation contribution from relative humidity, temperature, and vertical velocity, respectively. Despite the terms not being independent, their sum deviates little from that of the full equation with an average absolute error of 2.9%, 3.6%, and 3.1% in 20CRv3, ERA-20C, and ERA5, respectively, on an annual timescale. The small absolute errors indicate that the separation method is adequate and that the contributions from the interactive terms are small.

3. Observed Climatology and Trends

3.1. Is the Station Network in the Long Time Series Representative?

As the station coverage increased substantially from 1900 to 1960 (55 stations to 199 stations), we check whether OP1900 represents precipitation on both a regional and national level compared to OP1960 (see Figure 1 for an overview of the spatial distribution of the stations). The national annual mean precipitation from OP1900 correlates near-perfectly to OP1960 ($r = 0.99$). Furthermore, a linear regression of the monthly average precipitation from OP1900 to OP1960 reveals a mean slope of $0.98x$, where x is the monthly average precipitation. Thus, OP1900 overestimates the monthly average precipitation by 2% compared to OP1960. However, OP1900 and OP1960 show a similar mean (difference <2.5%) and trend (difference <1%).

The high correlations between OP1900 and OP1960 can be explained by the high correlation between the stations in the coastal regions. For example, a station in Western correlates better to a station in Northern-Coastal more than 1,000 km away ($r = 0.4$) than to a closer station in Eastern, only 250 km away ($r = 0.1$).

With the number of stations and the correlation distances in mind, we do not have sufficient station coverage to calculate representative trends for Northern-Inland or Northern-Coastal. Northern-Inland has only two stations in OP1900 available, and they correlate poorly to each other because the correlation drops rapidly with distance ($r = 0.2$, mean distance = 100 km) and to stations in other regions ($r < 0.2$). The station coverage in Northern-Coastal is also poor, with only two stations in OP1900. Although these stations are better correlated than in Northern-Inland ($r = 0.4$, mean distance = 250 km) and show a quite high correlation to Middle-Coastal ($r = 0.4$, mean distance = 650 km), it is impossible to determine whether they are representative of the region.

However, we will present the climatology for both regions based on OP1960, when the station coverage in Northern-Coastal improves substantially (from 2 to 17 stations).

The high correlation between the stations within regions and the linear regression slope parameter (close to 1) gives us confidence that we can use OP1900 to analyze changes in the mean and extreme precipitation of most regions and Norway as a whole between 1900 and 2019.

3.2. Observed Precipitation Climatology

We calculate the climatology for 1960–2019 to include as many stations as possible. Norway has a clear separation between the coastal and inland climates. In the coastal regions, humid air masses from the west meet the steep orography along the coastline and form orographically enhanced precipitation, which maximizes at the first orographic barrier before it decreases (Figure 2). Both the frequency of precipitation and the intensity are highest in Western and South-Western in all seasons (Figures 2b and 2c). It rains more than 45% of the days with an average of more than 10 mm/day (see table 1 for an overview). In contrast, Northern-Inland and Middle-Inland are the driest regions, reflected in both low mean wet day intensity (<6 mm/day) and wet day frequency (<33%).

The seasonal timing of precipitation is also different between the inland and coastal regions (Figure 2a). While most precipitation in the coastal region falls during September-November (SON), June-August (JJA) is the wettest season in the inland regions. March-May (MAM) is the driest season in coastal regions, whereas December-February (DJF) is the driest season in inland regions. Although JJA contributes relatively more to annual precipitation in the inland regions, the coastal regions are wetter in all seasons.

The distribution of the extreme precipitation (99th percentile) largely follows that of the observed climatology (Figure 2d). The 99th percentile is highest in Western Norway, and extreme precipitation events mainly occur in SON and DJF. Most extreme precipitation events occur in JJA and SON in the inland regions, and the 99th percentile is lower than in the coastal regions. However, the contribution from extreme precipitation to the annual total precipitation is higher in inland regions (15%–17%) than in coastal regions (12%–14%), and the proportion is increasing northwards (not shown).

The different seasonal cycles of precipitation and the differences in the rate at which correlation decrease with distance indicate different precipitation-generating mechanisms between the regions. That precipitation in coastal regions affects larger areas than in inland regions is consistent with precipitation events in coastal regions being of more synoptic-scale nature and directly associated with ETCs and westerly flow. This is consistent with Michel et al. (2021), who found that 82% of precipitation extremes in Western were associated with atmospheric rivers, which are linked to ETCs (e.g., Ralph et al., 2004). In contrast, <50% of extreme events in inland regions occurred with atmospheric rivers. This suggests that local convection and fewer or weaker ETCs dominate inland regions.

3.3. Trends and Changes in Time

The annual mean precipitation in Norway has increased by 19% between 1900 and 2019 (Figure 3a). The slightly larger value compared to Hanssen-Bauer et al. (2017) can be partly attributed to the inclusions of the years 2017–2019. It is also possible that the discrepancies come from different datasets used, as we use the station observations directly while Hanssen-Bauer et al. (2017) use a monthly gridded data set. Gridded datasets and observations have been shown to give different trends (Hanssen-Bauer et al., 2006). Precipitation has increased significantly in Western, Eastern, Middle-Coastal, Middle-Inland, and South-Western (see table 1 for an overview of all trends in all regions). Middle-Coastal has the largest relative increase (30.2%), but the region has no trend in the second half of the time series. In contrast, South-Western has the largest absolute increase (414 mm), with most of the increase after 1960 (402 mm). Lastly, five of the six regions with adequate data coverage exhibit a statistically significant trend at the 99% confidence level compared to the 4 of 13 regions in Hanssen-Bauer (2005).

Consistent with Hanssen-Bauer (2005), we find that precipitation in Norway since 1900 has increased in all seasons, but most in absolute magnitudes in SON (19.9%) and relative magnitudes in MAM (Figure 4, Figure S1 in Supporting Information S1). DJF is the only season without a significant trend in the long time series because of high interannual variability (however, the trend is still positive). Notably, almost half of the long-term increase occurred between 1980 and 1990 and was most prominent in DJF. Western and South-Western show the largest
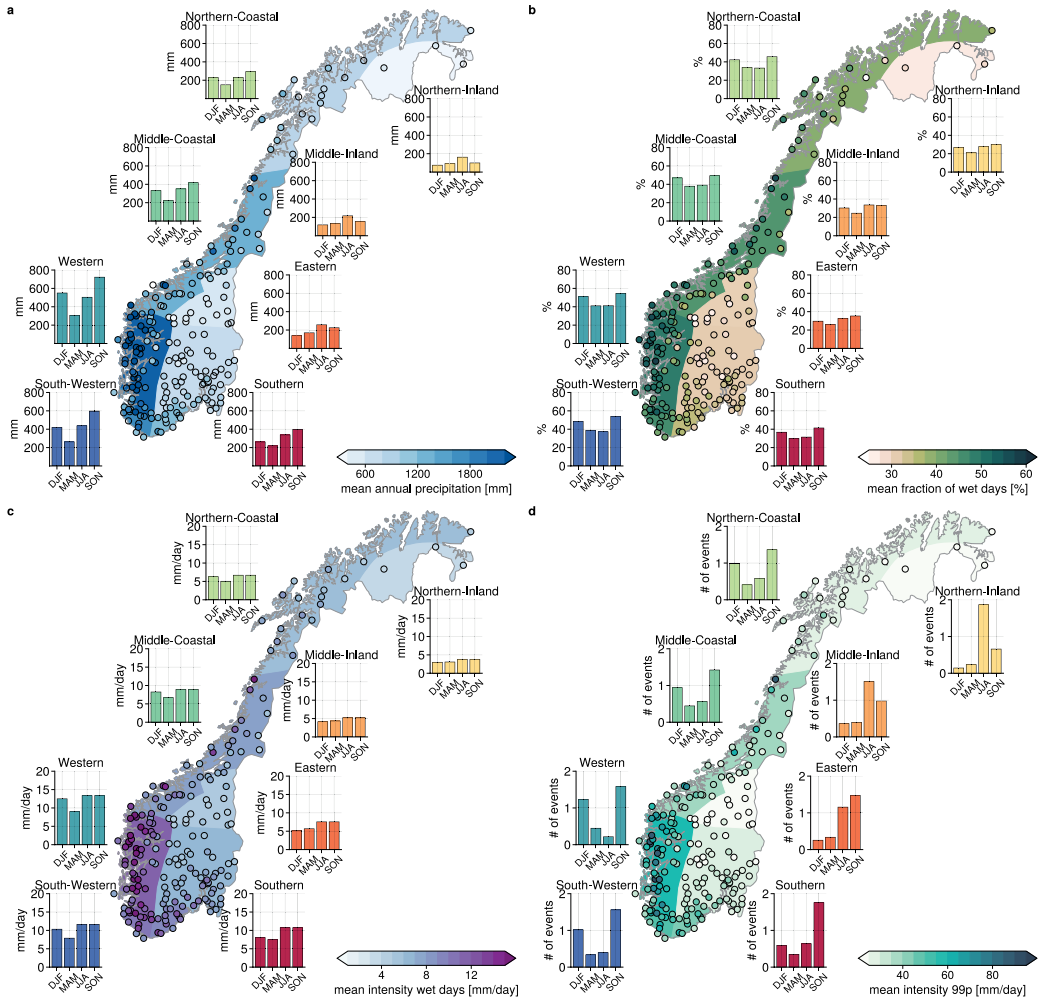
Figure 2. Spatial pattern of precipitation in Norway. Bars represent the seasonal average in the different regions. The map and individual stations are shaded according to (a) The annual mean precipitation in mm, (b) Wet day frequency, given in percent, and (c) mean intensity on the wet days in mm/day, (d) 99th percentile of daily precipitation amount (99p), while the bars represent the average number of events per year in the different seasons in the different regions.

increase, both in absolute and relative terms, but a signal is present in all regions (Figure 4 a, see Figure S1 in Supporting Information S1 for relative terms). This increase looks particularly dramatic because the years before 1980 were anomalously dry, while the years after were anomalously wet compared to the mean. The precipitation continued to increase after 1990, but at a lower rate and in all regions and seasons (Figures 4a–4d).

Both the frequency and intensity have contributed to the change in observed precipitation. In Norway, on average, between 1960 and 2019, the number of wet days increased by almost 10 days (6%, see Table 1), with an accompanying significant decrease in the annual longest dry spells (consecutive dry days, <1 mm/day). The trend in the absolute contribution of the precipitation rates to the annual total precipitation increase across all precipitation rates (Figure S2a in Supporting Information S1) indicates an overall increase in wet days, including an increase in

Table 1
Trends in Mean Wet-Day Intensity Intensity, Annual Total, and the Number of Wet Days

			South-Western	Southern	Northern-Inland	Western	Eastern	Middle-Coastal	Middle-Inland	Northern-Coastal	Norway
Mean wet-day intensity	1900	mean [mm/day]	10.8	10.0	3.9	10.7	6.8	7.8	5.5	5.8	8.1
		rel	13.9[b]	2.1	-	7.2[a]	5.8[a]	20.6[b]	4.6	-	8.1[b]
		abs	1.5[b]	0.2	-	0.8[a]	0.4[a]	1.6[b]	0.3	-	0.7[b]
	1960	mean [mm/day]	10.1	9.2	4.0	11.4	6.7	7.9	5.1	6.1	8.2
		rel	12.5[b]	5.2	1.4	11.1[a]	7.3[a]	9.2[a]	7.9[b]	9.3	9.4[b]
		abs	1.3[b]	0.5	0.1	1.3[a]	0.5[a]	0.7[a]	0.4[b]	0.6	0.8[b]
Annual precipitation	1900	mean [mm/year]	1,772.7	1,362.1	381.1	1,850.5	803.0	1,230.8	686.9	785.4	1,189.1
		rel	23.4[b]	9.0	-	17.3[b]	18.3[b]	30.2[b]	22.4[b]	-	20.0[b]
		abs	414.5[b]	123.0	-	319.9[b]	147.1[b]	371.9[b]	154.0[b]	-	236.6[b]
	1960	mean [mm/year]	1,720.8	1,207.6	409.0	2,079.9	786.9	1,332.1	610.4	907.2	1,270.0
		rel	23.8[b]	16.7	0.4	18.0	15.6[a]	10.2	14.4[b]	4.9	17.2[b]
		abs	408.8[b]	201.3	1.8	372.3	122.7[a]	135.4	88.0[b]	44.5	219.2[b]
Number of wet days	1900	mean [days/year]	162.9	135.5	98.3	166.7	116.4	152.3	117.4	135.9	137.2
		rel	7.6[a]	7.2	-	12.2[b]	13.4[b]	10.7[b]	18.5[b]	-	12.9[b]
		abs	12.6[a]	9.7	-	20.3[b]	15.6[b]	16.3[b]	21.7[b]	-	17.7[b]
	1960	mean [days/year]	167.9	130.6	102.2	177.3	117.1	163.4	115.7	145.3	146.1
		rel	10.9[a]	10.9[a]	0.0	6.9	9.8	2.7	8.1[a]	−2.6	6.6
		abs	18.3[a]	14.3[a]	0.0	12.2	11.5	4.5	9.4[a]	−3.8	9.7

Note. Changes are both from the long and short time series; note that the trends starting in 1960 are based on substantially more stations. The changes are multiplied with the length of the period, 120 and 60 years for the time series starting in 1900 and 1960, respectively. rel is the change in relative terms over the period, whereas abs is the trend in absolute measures (units of mm, days, and mm). The no-data is in regions where we find it misleading to calculate the trends because of the poor station coverage.

[a]Significant at the 5% confidence level. [b]Significant at 99% confidence level.

drizzle days. This is in contrast to the hypothesis that a warmer climate dominated by the thermodynamic mechanism would have more days of heavy precipitation and fewer days of drizzle, leading to a general decrease in the number of wet days. Climate models show fewer days of drizzle at the end of the century compared to present over most land areas in a low-emission scenario (Sun et al., 2007), but the result is highly dependent on model resolution (Stephens et al., 2010). In contrast to the trend in the absolute contribution of the precipitation rates to the annual total precipitation, the relative contribution decreases at the lower precipitation rates and increased at higher rates (Figure S2b in Supporting Information S1). The precipitation intensity has increased by almost 10%
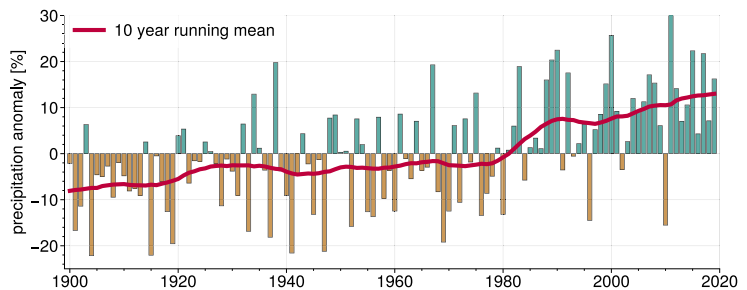
Figure 3. Time series of annual mean precipitation anomalies relative to the whole time series. The thin red line indicates number of averaging years is less than the length of the sliding averaging-window.
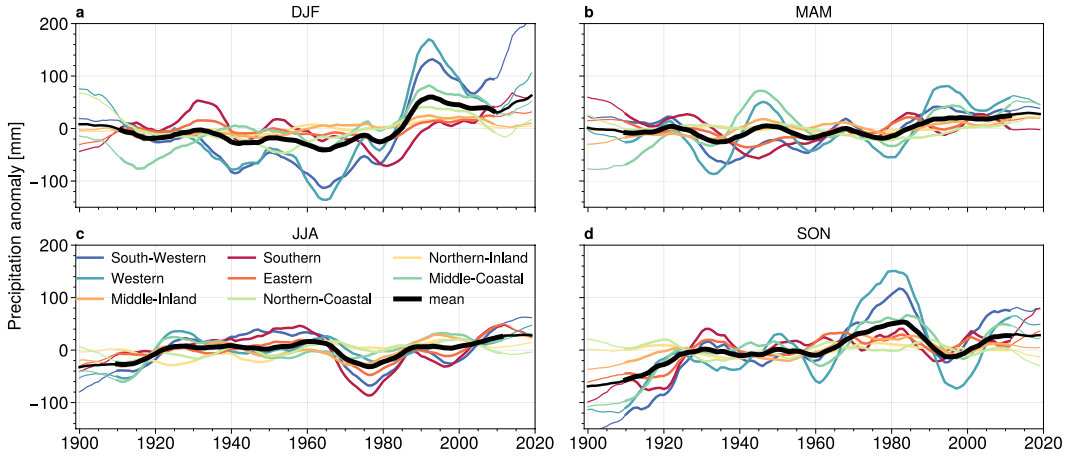
Figure 4. Seasonal 10 year running mean precipitation anomalies for each region relative to the whole time series.

in Norway since 1900. The precipitation increase in Norway is due to both increased frequency and intensity. It is neither constrained to the upper percentiles nor is it happening at the expense of the lower percentiles.
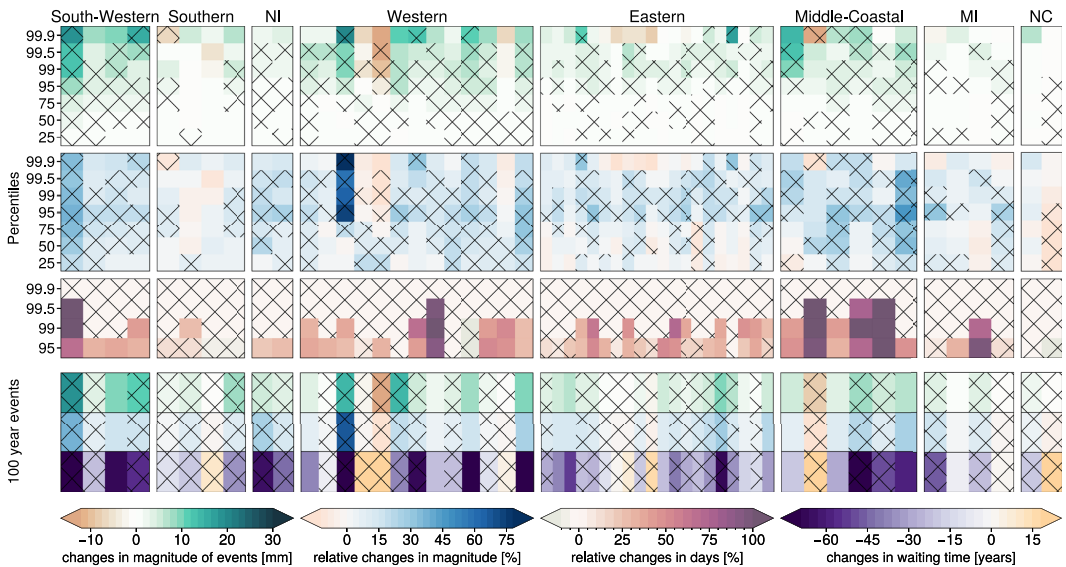
3.4. Changes in Intense and Extreme Precipitation

To investigate changes in intense and extreme precipitation, we use quantile regression as well as extreme value theory.

The 95th and 99th percentiles show a positive change in 90% of the OP1900-stations using quantile regression, and half of these trends are significant at the 5% significance level. That the absolute increase is becoming larger for the higher percentiles and that most stations exhibit a positive trend is visible in Figure 5 top panel (absolute changes). The relative changes of the 99th percentile are larger than the mean in 49% of the stations in Norway and 69% of the stations for the 95th percentile, consistent with the notion that intense precipitation will increase faster than the mean in the future (Myhre et al., 2019) (Figure 5, second row). Although more stations show negative trends at even higher percentiles (99.5th and 99.9th), the majority still show positive trends (96%/76% OP1900/OP1960), but few of the trends are significant. The 95th percentile increases significantly in South-Western (23%), Northern-Inland (23%), Eastern (16%), and Middle-Coastal (25%). Despite the significant increase of the 95th percentile, the fraction of the 95th percentile to the total annual precipitation has only increased significantly in South-Western (increased by 9% over the past 120 years), Northern-Inland (6.5%), and Middle-Coastal (9.6%). At lower percentiles (25th to 75th), the trends are both positive and negative but small (<1 mm/60 years/<10%).

Calculating the changes in the number of days of intense precipitation based on a constant threshold for the 95th, 99th, 99.5th, and 99.9th percentile, most stations show an increase in the number of days exceeding the thresholds (Figure 5, third panel), although not necessarily significant. Days exceeding the 95th percentile increased by 4.9 days over 120 years (30%), the 99th percentile increased by 0.8 days (24%), while there is no trend for the 99.9th percentile. The relative trend is of similar magnitude for the different percentiles. In Middle-Coastal, the days with precipitation exceeding the 95th percentile have increased by 12 days in the past 120 years, and the trend is steeper in OP1960 (0.7 days/year) than OP1900 (0.04 days/year).

The bottom panel of Figure 5 shows the results from fitting a GEV-distribution to the annual maxima and introducing time as a covariate to the location parameter. Although the uncertainties are large (not shown), most stations have a positive trend in the magnitude of the 100-year events (on average, 40% increase), and the waiting time is reduced by 25 years. However, some of the stations show more than 60 years reduction in waiting time for a 100 year event. It is worth noting that all significant trends are positive (23% of the stations). In addition, the overall pattern is qualitatively consistent with the trends in the quantile regression.

Figure 5. Summary of the changes in extreme and intense precipitation. Each tile along the x-axis represents the individual stations grouped together in regions. Top panel: Changes in percentiles grouped by regions for all stations available from 1900 from quantile regression. The upper percentiles (>95) are based on all days, while the lower are based on only the wet days to avoid zero precipitation at the lower percentiles. Second panel: same as top, but for relative changes. Third panel: Trend in relative number of days exceeding a percentile. Bottom panel: Results from the GEV-fitting, split into three rows: (a) changes in the absolute magnitude of 100 year events, (b) changes in the relative magnitude of 100 year events, (c) changes in waiting time in years. Note that the changes are given over a 120 year period (1900–2019). NI is Northern-Inland, MI is Middle-Inland, and NC is Northern-Coastal. Hatching indicates non-significant trends at the 95% significant level.

Some variability in the sign of the trends is expected as all statistical tests are designed to have a specified false discovery rate. Sun et al. (2021) found that for the Rx1day index (the annual maximum precipitation), 10% of the stations in Europe showed significant increasing trends at the 95% confidence interval, which was larger compared to what can be expected by chance alone (between 0% and 6%). Although not directly comparable, 18% of the stations show a significant increasing trend in Norway for the 99th percentile, which on average occur 4 times a year. The 3.6% stations showing significant negative trends are, on the other hand, within the range of what can be considered "due to chance," and there are no systematic negative trends within or between regions. The overall tendency is thus toward more intense precipitation, although the interannual variability is large. Furthermore, the fact that the two different methods agree corroborates that the extreme precipitation has increased over the past century.

4. Drivers of Annual Precipitation Variability and Trends

What has caused the change in annual mean precipitation? We have described the statistical properties of how the precipitation has changed over the past 120 years. To relate the observed annual mean precipitation increase to either thermodynamic or dynamic changes, we use the diagnostic model outlined in Equation 1. The diagnostic model estimates precipitation – based on pseudoadiabatic ascent – for three different reanalysis products, ERA-20C, 20CRv3, and ERA5. We show the annual relative anomalies of the estimated precipitation (pseudoadiabatic precipitation, [PAP]) compared to the observed precipitation (OP1900) and precipitation from ERA-20C (P_ERA-20C) and 20CRv3 (P_20CRv3) in Figure 6. Because observations represent point-processes rather than area averages as models do, we bin the observations on a 1° × 1° latitude-longitude grid and do the average of all stations in a grid box prior to averaging over all the grid boxes in a region. This way, we avoid emphasizing regions with a high station density but note that we are comparing PAP to a smaller set of grid points which can cause some discrepancies when comparing PAP to OP1900.
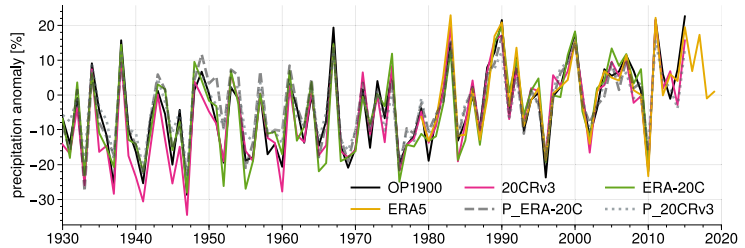
Figure 6. Pseudoadiabatic precipitation based on ERA5, ERA-20C, and 20CRv3, observed precipitation (OP1900), and precipitation from reanalysis (P_ERA-20C and P_20CRv3) anomalies compared to the 1980–2010 average over Norway.

The number of pressure observations assimilated into the reanalysis in Northern Europe was sparse before 1935 (Slivinski et al., 2019) and the quality of the reanalyzes is more questionable before 1950 in terms of circulation indices such as the North Atlantic and Arctic Oscillations (Bloomfield et al., 2018; Poli et al., 2016). However, we find that PAP correlates well with OP1900 after 1930 ($r > 0.9$) in both reanalyses, and considerably higher than between 1900 and 1930 ($r = 0.68$) on an annual time scale. We therefore omit the period 1900–1930 from our analysis.

The absolute level of PAP is underestimated compared to OP1900, and more so using ERA-20C than both 20CRv3 and ERA5 (see a summary of key numbers in Table S1 of Supporting Information S1). The different magnitude of PAP in ERA-20C compared to 20CRv3 can be linked to the critical relative humidity; although the relative humidity is consistently higher in 20CRv3 than in ERA-20C, we have used the same critical relative humidity. However, the variability and the relative anomalies are similar between PAP using all reanalysis products and OP1900, indicating that the relative humidity mainly affects the magnitude of precipitation and not the variability.

In addition to a high temporal correlation on an annual time scale, PAP also shows similar spatial variability characteristics, with higher values in coastal Norway than inland regions. The trend is also relatively well captured in PAP, 20% (17%) in 20CRv3 (ERA-20C) compared to the observed 14%. Note that the trend differs slightly from the result presented earlier (see Table 1) due to a different period (1930–2010) and averaging method. Because the method works adequately, both spatial and temporal, we use Equation 2 to decompose the observed changes in precipitation into contributions from thermodynamics (through changes in temperature and subsequent changes in the water vapor content), dynamics (through changes in vertical velocity), and changes in relative humidity.

Vertical velocity is the key variable in understanding the interannual variability and the long-term trend in annual precipitation (Figure 7). $P_{\omega*}$ (precipitation varying only due to the vertical velocity) accounts for 93% (89%) of the yearly variance in PAP based on 20CRv3 (ERA-20C). The contribution from vertical velocity to the precipitation anomalies is mainly negative before 1970 and positive after 1970. This shift coincides with the marked increase in the observed precipitation (Figure 3). In addition, it is worth noting that the absolute magnitude of the vertical velocity differs substantially between ERA-20C and 20CRv3, although the relative anomalies are the same. ERA-20C shows consistently weaker vertical motion than 20CRv3, which provides an additional explanation for why the estimated absolute precipitation values are lower in ERA-20C than 20CRv3.

P_{λ} (precipitation varying only due to the relative humidity) accounts for <1% of the interannual variability using 20CRv3 and 45% using ERA-20C. The discrepancy arises because the relative humidity is higher in 20CRv3 than in ERA-20C, but RH_c is the same. As the relative humidity in 20CRv3 tend to be above RH_c, the precipitation frequency is mainly decided by the frequency of upward motion, while it is also limited by relative humidity in ERA-20C. Therefore, the correlation of PAP to $P_{\omega*}$ in 20CRv3 is higher than in ERA-20C, while P_{λ} accounts for more of the variability in ERA-20C. Lastly, P_T* (precipitation varying only due to surface temperature) accounts for 58% (61%) in 20CRv3 (ERA-20C). Note that the sum of the variability exceeds 100% because the terms are not independent.

We can decompose the trend into the trends in individual additive terms (Equation 2). The sum of the trends of the individual terms (P_{λ}, $P_{\omega*}$, P_{T*}) roughly equals the full estimated PAP trend (the difference is less than 2%
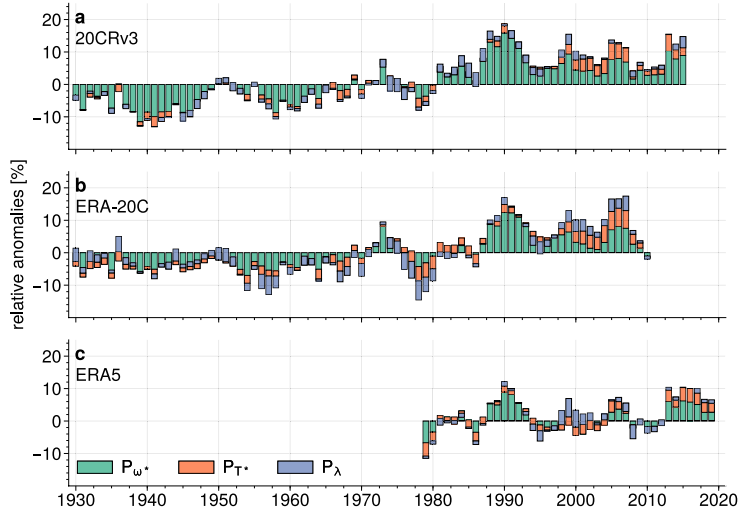
Figure 7. 5 year running mean of relative anomalies over Norway. $P_{\omega*}$ - contribution from vertical velocity, P_λ - relative humidity, P_{T*} - temperature. Note that 20CRv3 (a) and ERA-20C (b) use the same averaging period (1930–2010), whereas ERA5 (c) use the whole period available as the reference (1979–2019).

using both 20CRv3 and ERA-20C. However, the relative trends in PAP are overestimated compared to OP1900's in 20CRv3 (5% higher using 20CRv3). Decomposing the trends yield no contribution from P_λ in ERA-20C nor 20CRv3 between 1930 and 2010 because there is no trend in relative humidity over Norway. Changes in $P_{\omega*}$ accounts for 86% of the total trend in ERA-20C, and 84% in 20CRv3, while P_{T*} comprises the rest. In ERA5, between 1979 and 2019, the slightly positive trend in $P_{\omega*}$ is directly offset by the negative trend in P_λ, while P_{T*} accounts for 93% of the trend. Consistent with ERA5, the trend is smaller in $P_{\omega*}$ in ERA-20C and 20CRv3 between 1979 and 2019.

To estimate the sensitivity of the surface temperature to precipitation, we do a linear regression of PAP to the near-surface temperature over Norway in the respective reanalysis. The temperature increase in ERA-20C is only 0.6 K over Norway, while it is 0.7 K in 20CRv3, less than the observed 1K increase (Hanssen-Bauer et al., 2017). For 20CRv3 (ERA-20C), this yields a sensitivity to temperature of 10%/K (12%/K) of PAP to temperature, and 4.5%K (5%/K) for P_{T*} in 20CRv3 (ERA-20C). The sensitivity of P_{T*} to temperature is slightly less than we would expect from pseudoadiabatic scaling. $P_{\omega*}$ sensitivity to temperature is 8%/K in 20CRv3 and 6.8%/K in ERA-20C. The main discrepancy between the reanalyzes is in P_λ, which shows no relation to temperature in 20CRv3, while it is positive (6.8%/K) in ERA-20C. However, this difference is most likely due to the discrepancies in RH and RH_c, as discussed earlier.

The sensitivity of the dynamic contribution to temperature is what differs most compared to Pfahl et al. (2017), who showed a sensitivity in the dynamic contribution in the future of 1%–3%/K over Scandinavia. However, the sensitivity in Pfahl et al. (2017) is calculated based on the model ensemble mean, and individual members' dynamic components may be more sensitive to changes in temperature. This is reflected in the large uncertainty in the future changes in the dynamic component (Pfahl et al., 2017). In addition, part of the discrepancy may be because we regress the dynamic component against changes in annual mean temperature in Norway rather than the global mean temperature. Furthermore, we have calculated the dynamic component directly, and taken the seasonality into account of the decomposition, which differs from the method of Pfahl et al. (2017).

Although the vertical velocity is argued to change little in the future, we find that the vertical velocity in the reanalyzes has changed over the past century. Vertical velocity is thought to change little with climate change in the extratropics because it does not depend on either static stability or latent heating in a non-convective environment (O'Gorman, 2015). However, in ETCs, the asymmetry of vertical velocity and hence the strength of the
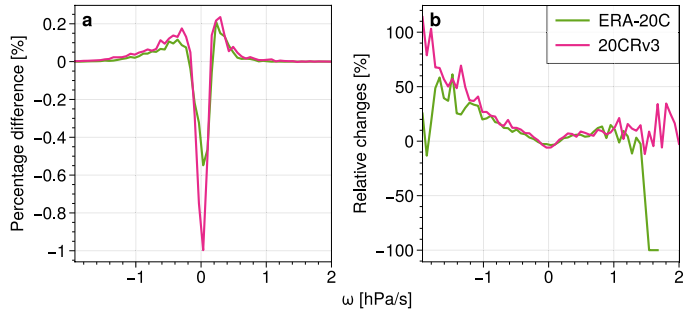
Figure 8. Changes in the distribution of ω at 850 hPa, calculated as the change of the number of occurrences in each intensity of the vertical velocity between 1970 and 2010 compared to 1930–1970. (a) The change in the probability for the different intensities of vertical velocity. (b) Same as a, but normalized by the probability of an intensity to occur in the former period.

upward motion has the potential to increase in the future because of increased latent heating (Tamarin-Brodsky & Hadas, 2019). If the asymmetry of the vertical motion increases, this may not be visible in the average changes of the vertical velocity but might be vital for precipitation changes as its distribution is known to link intimately to the precipitation distribution. Pendergrass and Gerber (2016) found that changing the skewness of the vertical velocity distribution was crucial to represent important characteristics of the changes in precipitation, that is, that extreme precipitation is increasing more than the mean. We, therefore, compare how the mean distribution of ω has changed over Norway between 1970-2010 and 1930–1970 (Figure 8). For all pressure levels (Figure 8a, only 850 hPa shown), there are fewer occurrences of weak vertical motion in the later period than in the earlier period, indicating that the width of the distribution increased. Both the upward and downward intensity increase in both reanalysis products, but the change is more pronounced in 20CRv3 than ERA-20C. Although the overall change is small (2% more days of upward motion in the later period compared to the earlier period), some bins show substantial changes (Figure 8b). The strongest upward motion increases with more than 50% in ERA-20C and more than 100% in 20CRv3. The changes in vertical velocity distribution reveal that the tail is longer for changes in upward motions ($\omega < 0$) than downward motions, which agrees qualitatively with the observed asymmetric precipitation response. In addition, the frequency of days with upward motion is increasing, consistent with the observed frequency increase. However, the relative increase in the occurrences of upward motion is considerably smaller than the observed frequency increase.

4.1. Precipitation Increase From 1980 to 2010

Notably, almost half of the precipitation increase occurred between 1980 and 1990 (Figure 3). We focus on this period to better understand what caused this increase. The model captures the increase and the dry years before the increase (Figure 6). While anomalous low relative humidity and temperatures cause the dry years (negative contributions from P_{λ} and P_{T^*}), enhanced vertical velocity (positive contribution from $P_{\omega*}$) cause the wet period (Figure 7). The positive contribution from vertical velocity is consistent across all reanalysis products, although the magnitude differs.

ETCs are linked to precipitation as they constitute areas of large-scale ascent and subsequent condensation and precipitation. In addition, ETCs are associated with fronts and often intense moisture transport, which, as it approaches Norway, is forced over topography and causes heavy precipitation. Hawcroft et al. (2012) found that >75% of all winter precipitation over Norway can be associated with ETCs. The storm track activity has been analyzed in previous studies using different reanalyzes and proxies. Feser et al. (2015); Chang and Fu (2003) found that storm track activity was weakest during the 1960s and increased until the 1990s before it decreased back to average values until 2010. The increase in storm track activity was particularly prominent over the Eastern Atlantic and Europe (Chang & Fu, 2003). The timing of the lowest storm track activity fits well with the all-time driest winter in coastal regions in DJF in the 1960s and the subsequent increase in precipitation to an all-time maximum in DJF in the 1990s (Figure 4a). The decrease in storm track activity coincides with the decline

in the importance of vertical velocity in our diagnostic model (Figure 7), and we, therefore, hypothesize that the changes in the vertical velocity and hence the dynamic component of precipitation are associated with the storm track variability in the North Atlantic. In addition, as mentioned before, the asymmetry of vertical velocity in ETCs can increase because of increased latent heating due to increasing temperatures (Tamarin-Brodsky & Hadas, 2019). After 2000, the contribution from P_T^* and P_λ dominates, particularly in ERA-20C, simultaneously as coastal DJF precipitation decreases. The increase after 2000 is happening in all regions and all seasons. We note that this is consistent with a pure thermodynamic response in precipitation to the increasing temperatures in Norway after 2000. Furthermore, dynamic or circulation changes over Europe are consistent with other studies. Sippel et al. (2020) linked the rapid temperature increase in the 1980s over Europe to circulation changes. Furthermore, van Haren et al. (2013) found that errors in the climate model simulated circulation patterns were the main reason for the bias in precipitation trends over Northern Europe, rather than a direct effect of the models' coarse resolution on precipitation. However, making an exact link of ETCs to precipitation changes in Norway and changes in vertical velocity requires further research and is beyond the scope of this paper. In addition, previous studies have determined that the dynamic component has been crucial for changes in extremes. Ali and Mishra (2018) found that the dynamic component scaled with more than 10%/K for extreme precipitation events over India and was substantially larger than the thermodynamic scaling. When decomposing the moisture budget for a record-breaking wet January in Britain, Oueslati et al. (2019) found the dynamic component to play the most important role. We show that the dynamic component is also the main factor deciding the interannual variability in mean precipitation over long timescales in Norway.

4.2. Applicability of Method

Although we have only used this method in Norway, we believe we can say something about the general applicability of the method by investigating the method's performance in the different regions. In the individual regions, the correlation between OP1900 (observed precipitation) and PAP (pseudoadiabatic ascent estimated precipitation) drops to a mean of 0.78 in 20CRv3 (min = 0.54, max = 0.88) and 0.68 in ERA-20C (min = 0.4, max = 0.86), and the best agreement is in South-Western and Western, followed by the rest of the coastal regions.

In the inland regions (Eastern, Northern-Inland, and Middle-Inland), PAP is underestimated in summer and overestimated in winter compared to observations and reanalysis-precipitation. Although OP1900 increases from spring to summer in Northern-Inland and Middle-Inland, PAP overestimates the precipitation in SON and DJF. PAP underestimates precipitation in summer in Western and Middle-Coastal, but only compared to reanalyzes-precipitation, not OP1900. However, as the observations are averaged over a smaller number of grid points, it may be that the observations are located where summer precipitation is lower than the regional average or that the summer precipitation is not accurately represented in the reanalyzes. Although ERA5 has a higher resolution and should thus better represent the vertical velocity associated with convection and possibly better capture the seasonal cycle, PAP does not have a better seasonal cycle in ERA5 than the other reanalyzes. This is most likely related to the simplistic nature of the PAP model. An essential assumption of the model is that the moisture supply is unlimited when precipitation occurs, which is not necessarily valid in the inland regions. This may partly account for the overestimation of PAP compared to OP1900, particularly because the method assumes it precipitates for 24 hr. The assumption that precipitation does not evaporate on the way down may lead to an overestimation during drizzle events but is probably less important than the aforementioned simplification. Lastly, ERA-20C and 20CRv3 most likely represent the vertical velocity more accurately in regions where it is governed by synoptic-scale dynamics. The combination of this and the coastal regions having no shortage of moisture supply may explain why the seasonal cycle is better represented in coastal regions where most precipitation falls during SON and DJF.

To conclude, care should be taken in regions where most precipitation falls during strong convective events and regions where the moisture supply is limited if this method is further used for mean precipitation.

5. Uncertainties Associated With Precipitation Measurements

Precipitation measurements are susceptible to a change in location, measurement technique, or installation of windshields. Hanssen-Bauer and Førland (1994) found that the relocation of weather stations accounted for 47% of the detected inhomogeneities in precipitation stations in Norway. Relocation of weather stations can cause

artificially induced trends either because the sheltering conditions are different or because the annual precipitation is different. We might have induced artificially induced trends when we merged stations; however, we discarded the entire station if any breakpoint was detected close to a station merging.

In addition to relocation, wind affects the precipitation catch. Hanssen-Bauer and Førland (1994) found that the installation of windshields was responsible for 30% of the inhomogeneities in the long precipitation series in Norway. The installation of windshields improves the catch, particularly in regions where a large portion of the precipitation falls as snow, but does not substantially increase the catch, even in windy conditions, for temperatures <3°C (Wolff et al., 2015). In regions and mountainous areas where most precipitation falls as snow, a transition from snow to rain can also induce trends in measured precipitation. Such a trend would be mainly visible in the onset or offset of winter. However, it is impossible to determine whether the observed trends are due to a snow-rain transition. We, therefore, took the conservative approach and threw out all stations with significant breakpoints detected by the homogeneity test. The installation of windshields and snow-rain transition is likely why so few stations at high elevations and in Northern Norway passed the quality control.

In contrast, winters in South-Western and Western tend to be mild and rainy, and the installation of windshields is thought to be of minor importance (Hanssen-Bauer & Førland, 1994), as well as the snow-rain transition. Furthermore, 70% of all windshield installations were done in the period 1906–1910 (Hanssen-Bauer & Førland, 1994), and we find that the trend from 1930 to 2010 is not substantially different from the trend from 1900 to 2019. It is worth noting that, overall, the trends from the reanalyzes precipitation match the observed and the estimated precipitation (PAP).

Except for automatization gradually happening over the last decade, the sampling routine and bucket diameter have not changed. Automatization was responsible for 12% of the detected breakpoints between 1960 and 2018 and generally reduced the precipitation catch (Kuya & Tveito, 2021). At the same time, the sampling frequency has increased in some stations from one to three times a day, which might influence the very low precipitation amounts due to decreased evaporation.

Our calculated trends are consistent with previous studies (Hanssen-Bauer, 2005; Hanssen-Bauer et al., 2017; Hanssen-Bauer & Førland, 1998, 2000). Despite the uncertainties related to precipitation measurements, we are confident that the trends presented here represent the actual trends except in the Northernmost regions where the station coverage remains poor. Lastly, our study shows that 20th-century reanalyzes are not only providing accurate estimates of precipitation in Europe (Poli et al., 2016) but can also be representative for smaller areas such as Norway.

6. Conclusions

We have analyzed observations of daily accumulated precipitation from a network of stations that measured continuously between 1900 and 2019 and introduced and used a diagnostic model to assess the mechanisms responsible for the historical precipitation variation in Norway. We find that in Norway:

1. Precipitation has increased by 19% between 1900 and 2019. Notably, almost half of the increase occurred between 1980 and 1990 in winter. In contrast, the precipitation increase after 2000 occurs in all seasons.
2. Both frequency and intensity contribute to the precipitation increase. Although we find a positive trend across all precipitation rates, intense precipitation's absolute magnitudes increase faster than the mean.
3. The long-term trend and year-to-year variation in precipitation can be approximated with pseudoadiabatic ascent and hence three parameters: vertical velocity, temperature, and relative humidity. Changes in precipitation can then be related to these three parameters.
4. Vertical velocity is the key variable for precipitation variability and the long-term trend.
5. The precipitation increase between 1980 and 1990 appears dramatic, but this is partly because the late '60s and '70s were anomalously dry. While low temperatures and relative humidity can explain some of the period's dryness, anomalous upward motion, and thus the dynamic contribution, dominates the wet period in the late '80s and early '90s, which corresponds to a time period where previous studies have found increased storm track activity in the North-Eastern Atlantic.

6. From 2000 and onward, the vertical velocity is less important than before. Instead, the high precipitation amounts link to anomalously high temperatures and relative humidity, and, consistent with a pure thermodynamic response, the precipitation increase is happening in all regions and seasons.

The precipitation increase in Norway is larger than what can be explained by increased water vapor in the atmosphere alone. Our decomposition of the precipitation increase points to the importance of vertical velocity, both for the variability and long-term trend. The dynamic part is the most uncertain parameter regarding precipitation changes in climate models. Hence, to predict precipitation changes in the future, it is critical to understand the mechanisms responsible for the changes in vertical motion in the past and the weather that governs it.

Data Availability Statement

The precipitation station data from the Norwegian Meteorological Institute used in this study is accessible at https://frost.met.no/. ERA5 was downloaded from the Copernicus Climate Change Service (C3S) Climate Data Store (https://cds.climate.copernicus.eu/cdsapp), and ERA-20C from ECMWF (https://apps.ecmwf.int/datasets/data/era20c-daily). NOAA/CIRES/DOE 20th Century Reanalysis V3 (20CRv3) data was provided by the NOAA PSL, Boulder, Colorado, USA, from their website at https://psl.noaa.gov/data/gridded/data.20thC_ReanV3.html. The software for the penalized maximum *F*-test used for homogeneity testing of the stations is available for download at http://etccdi.pacificclimate.org/software. We used the extRemes package (Gilleland & Katz, 2016) for extreme value analysis, available for download at https://CRAN.R-project.org/package=extRemes.

References

Alexander, L. V., Zhang, X., Peterson, T. C., Caesar, J., Gleason, B., Klein Tank, A. M., et al. (2006). Global observed changes in daily climate extremes of temperature and precipitation. *Journal of Geophysical Research*, *111*, D05109. https://doi.org/10.1029/2005JD006290

Ali, H., & Mishra, V. (2018). Contributions of dynamic and thermodynamic scaling in subdaily precipitation extremes in India. *Geophysical Research Letters*, *45*(5), 2352–2361. https://doi.org/10.1002/2018GL077065

Azad, R., & Sorteberg, A. (2017). Extreme daily precipitation in coastal western Norway and the link to atmospheric rivers. *Journal of Geophysical Research: Atmospheres*, *122*, 2080–2095. https://doi.org/10.1002/2016JD025615

Benedict, I., Ødemark, K., Nipen, T., & Moore, R. (2019). Large-scale flow patterns associated with extreme precipitation and atmospheric rivers over Norway. *Monthly Weather Review*, *147*(4), 1415–1428. https://doi.org/10.1175/MWR-D-18-0362.1

Bloomfield, H. C., Shaffrey, L. C., Hodges, K. I., & Vidale, P. L. (2018). A critical assessment of the long-term changes in the wintertime surface Arctic Oscillation and Northern Hemisphere storminess in the ERA20C reanalysis. *Environmental Research Letters*, *13*(9), 094004. https://doi.org/10.1088/1748-9326/aad5c5

Bohlinger, P., & Sorteberg, A. (2018). A comprehensive view on trends in extreme precipitation in Nepal and their spatial distribution. *International Journal of Climatology*, *38*(4), 1833–1845. https://doi.org/10.1002/joc.5299

Chang, E. K., & Fu, Y. (2003). Using mean flow change as a proxy to infer interdecadal storm track variability. *Journal of Climate*, *16*(13), 2178–2196. https://doi.org/10.1175/2773.1

Clausius, R. (1850). Ueber die bewegende Kraft der Wärme und die Gesetze, welche sich daraus für die Wärmelehre selbst ableiten lassen. *Annalen der Physik*, *155*(3), 368–397. https://doi.org/10.1002/andp.18501550306

Collier, C. G. (1975). A representation of the effects of topography on surface rainfall within moving baroclinic disturbances. *Quarterly Journal of the Royal Meteorological Society*, *101*(429), 407–422. https://doi.org/10.1002/qj.49710142902

Cram, T. A., Compo, G. P., Yin, X., Allan, R. J., McColl, C., Vose, R. S., et al. (2015). The international surface pressure databank version 2. *Geoscience Data Journal*, *2*(1), 31–46. https://doi.org/10.1002/GDJ3.25

Fan, L., & Chen, D. (2016). Trends in extreme precipitation indices across China detected using quantile regression. *Atmospheric Science Letters*, *17*(7), 400–406. https://doi.org/10.1002/asl.671

Feser, F., Barcikowska, M., Krueger, O., Schenk, F., Weisse, R., & Xia, L. (2015). Storminess over the North Atlantic and northwestern Europe-A review. *Quarterly Journal of the Royal Meteorological Society*, *141*(687), 350–382. https://doi.org/10.1002/qj.2364

Gilleland, E., & Katz, R. W. (2016). ExtRemes 2.0: An extreme value analysis package in R. *Journal of Statistical Software*, *72*(8). https://doi.org/10.18637/jss.v072.i08

Haltiner, G. J., & Williams, R. T. (1980). *Numerical prediction and dynamic meteorology* (2nd ed.). Wiley and Sons.

Hanssen-Bauer, I. (2005). *Regional temperature and precipitation series for Norway: Analyses of time-series updated to 2004 (Tech. Rep. No. 15)*. Norwegian Meteorological Institute.

Hanssen-Bauer, I., & Førland, E. (1998). *Annual and seasonal precipitation variations in Norway 1896-1997 (Tech. Rep.)*. Norwegian Meteorologican Institute.

Hanssen-Bauer, I., & Førland, E. (2000). Temperature and precipitation variations in Norway 1900-1994 and their links to atmospheric circulation. *International Journal of Climatology*, *20*(14), 1693–1708. https://doi.org/10.1002/1097-0088(20001130)20:14<1693::aid-joc567>3.0.co;2-7

Hanssen-Bauer, I., & Førland, E. J. (1994). Homogenizing long Norwegian precipitation series. *Journal of Climate*, *7*(6), 1001–1013. https://doi.org/10.1175/1520-0442(1994)007<1001:hlnps>2.0.co;2

Hanssen-Bauer, I., Førland, E. J., Haddeland, I., Hisdal, H., Lawrence, D., Mayer, S., et al. (2017). Climate in Norway 2100. NCCS report no. 1/2017 (pp. 1–47). Retrieved from www.miljodirektoratet.no/M741

Hanssen-Bauer, I., Tveito, O. E., & Szewczyk-Bartnicka, H. (2006). *Comparison of grid-based and station-based regional temperature and precipitation series (Tech. Rep. No. 04)*. Norwegian Meteorological Institute.

Hawcroft, M. K., Shaffrey, L. C., Hodges, K. I., & Dacre, H. F. (2012). How much Northern Hemisphere precipitation is associated with extratropical cyclones? *Geophysical Research Letters*, *39*(24), 2012GL053866. https://doi.org/10.1029/2012gl053866

Haylock, M. R., Hofstra, N., Klein Tank, A. M., Klok, E. J., Jones, P. D., & New, M. (2008). A European daily high-resolution gridded data set of surface temperature and precipitation for 1950-2006. *Journal of Geophysical Research*, *113*, D20119. https://doi.org/10.1029/2008JD010201

Heikkilä, U., & Sorteberg, A. (2012). Characteristics of autumn-winter extreme precipitation on the Norwegian west coast identified by cluster analysis. *Climate Dynamics*, *39*(3), 929–939. https://doi.org/10.1007/s00382-011-1277-9

Hersbach, H., Bell, B., Berrisford, P., Hirahara, S., Horányi, A., Muñoz-Sabater, J., et al. (2020). The ERA5 global reanalysis. *Quarterly Journal of the Royal Meteorological Society*, *146*(730), 1999–2049. https://doi.org/10.1002/qj.3803

Hu, L., Nikolopoulos, E. I., Marra, F., & Anagnostou, E. N. (2020). Sensitivity of flood frequency analysis to data record, statistical model, and parameter estimation methods: An evaluation over the contiguous United States. *Journal of Flood Risk Management*, *13*(1), 1–13. https://doi.org/10.1111/jfr3.12580

Kharin, V. V., Zwiers, F. W., Zhang, X., & Hegerl, G. C. (2007). Changes in temperature and precipitation extremes in the IPCC ensemble of global coupled model simulations. *Journal of Climate*, *20*(8), 1419–1444. https://doi.org/10.1175/jcli4066.1

Koenker, R., & Hallock, K. F. (2001). Quantile regression. *The Journal of Economic Perspectives*, *15*(4), 143–156. https://doi.org/10.1257/jep.15.4.143

Kunz, M., & Kottmeier, C. (2006). Orographic enhancement of precipitation over low mountain ranges. Part II: Simulations of heavy precipitation events over southwest Germany. *Journal of Applied Meteorology and Climatology*, *45*(8), 1041–1055. https://doi.org/10.1175/JAM2390.1

Kuya, E. K., & Tveito, O. E. (2021). Homogenization of Norwegian monthly precipitation series for the period 1961 - 2018 METreport (Tech. Rep. No. 4). Retrieved from https://www.met.no/publikasjoner/met-report/_/attachment/download/829d6a8e-1ec8-417d-8231-0268bddac4b-b:7eb30ca105a6cf1d470453976bb8d729a64b25a4/METreport04-21-Homogenizationofprecipitation1961-2018.pdf

Mann, H. B. (1945). Nonparametric tests against trend. *Econometrica*, *13*(3), 245–259. https://doi.org/10.2307/1907187

Michel, C., Sorteberg, A., Eckhardt, S., Weijenborg, C., Stohl, A., & Cassiani, M. (2021). Characterization of the atmospheric environment during extreme precipitation events associated with atmospheric rivers in Norway - seasonal and regional aspects. *Weather and Climate Extremes*, *34*, 100370. https://doi.org/10.1016/j.wace.2021.100370

Myhre, G., Alterskjær, K., Stjern, C. W., Hodnebrog, Marelle, L., Samset, B. H., & Stohl, A. (2019). Frequency of extreme precipitation increases extensively with event rareness under global warming. *Scientific Reports*, *9*(1), 2–11. https://doi.org/10.1038/s41598-019-52277-4

O'Gorman, P. A. (2015). Precipitation extremes under climate change. *Current Climate Change Reports*, *1*(2), 49–59. https://doi.org/10.1007/s40641-015-0009-3

Oueslati, B., Yiou, P., & Jézéquel, A. (2019). Revisiting the dynamic and thermodynamic processes driving the record-breaking January 2014 precipitation in the southern UK. *Scientific Reports*, *9*(1), 1–7. https://doi.org/10.1038/s41598-019-39306-y

Pendergrass, A. G., & Gerber, E. P. (2016). The rain is askew: Two idealized models relating vertical velocity and precipitation distributions in a warming world. *Journal of Climate*, *29*(18), 6445–6462. https://doi.org/10.1175/JCLI-D-16-0097.1

Pfahl, S., O'Gorman, P. A., Fischer, E. M., O'Gorman, P. A., & Fischer, E. M. (2017). Understanding the regional pattern of projected future changes in extreme precipitation. *Nature Climate Change*, *7*(6), 423–427. https://doi.org/10.1038/nclimate3287

Poli, P., Hersbach, H., Dee, D. P., Berrisford, P., Simmons, A. J., Vitart, F., et al. (2016). ERA-20C: An atmospheric reanalysis of the twentieth century. *Journal of Climate*, *29*(11), 4083–4097. https://doi.org/10.1175/JCLI-D-15-0556.1

Quaas, J. (2012). Evaluating the "critical relative humidity" as a measure of subgrid-scale variability of humidity in general circulation model cloud cover parameterizations using satellite data. *Journal of Geophysical Research*, *117*, D09208. https://doi.org/10.1029/2012JD017495

Ralph, F. M., Neiman, P. J., & Wick, G. A. (2004). Satellite and CALJET aircraft observations of atmospheric rivers over the Eastern North Pacific Ocean during the winter of 1997/98. *Monthly Weather Review*, *132*(7), 1721–1745. https://doi.org/10.1175/1520-0493(2004)132<1721:sacaoo>2.0.co;2

Sen, P. K. (1968). Estimates of the regression coefficient based on Kendall's Tau. *Journal of the American Statistical Association*, *63*(324), 1379–1389. https://doi.org/10.1080/01621459.1968.10480934

Seneviratne, S. I., Zhang, X., Adnan, M., Badi, W., Dereczynski, C., Luca, A. D., et al. (2021). Weather and Climate Extreme Events in a Changing Climate. (Eds.). In *Climate change 2021: The physical science basis. contribution of working group i to the sixth assessment report of the intergovernmental panel on climate change (chap. 11).* Cambridge University Press. Retrieved from https://www.ipcc.ch/report/ar6/wg1/downloads/report/IPCC_AR6_WGI_Chapter11.pdf

Shepherd, T. G. (2014). Atmospheric circulation as a source of uncertainty in climate change projections. *Nature Geoscience*, *7*(10), 703–708. https://doi.org/10.1038/NGEO2253

Sillmann, J., Kharin, V. V., Zwiers, F. W., Zhang, X., & Bronaugh, D. (2013). Climate extremes indices in the CMIP5 multimodel ensemble: Part 2. Future climate projections. *Journal of Geophysical Research: Atmospheres*, *118*, 2473–2493. https://doi.org/10.1002/jgrd.50188

Sinclair, M. R. (1994). A diagnostic model for estimating orographic precipitation. *Journal of Applied Meteorology*, *33*(10), 1163–1175. https://doi.org/10.1175/1520-0450(1994)033<1163:admfeo>2.0.co;2

Sippel, S., Fischer, E. M., Scherrer, S. C., Meinshausen, N., & Knutti, R. (2020). Late 1980s abrupt cold season temperature change in Europe consistent with circulation variability and long-term warming. *Environmental Research Letters*, *15*(9), 094056. https://doi.org/10.1088/1748-9326/ab86f2

Slivinski, L. C., Compo, G. P., Whitaker, J. S., Sardeshmukh, P. D., Giese, B. S., McColl, C., et al. (2019). Towards a more reliable historical reanalysis: Improvements for version 3 of the Twentieth Century Reanalysis system. *Quarterly Journal of the Royal Meteorological Society*, *145*(724), 2876–2908. https://doi.org/10.1002/qj.3598

Stephens, G. L., L'Ecuyer, T., Forbes, R., Gettlemen, A., Golaz, J. C., Bodas-Salcedo, A., et al. (2010). Dreary state of precipitation in global models. *Journal of Geophysical Research*, *115*, D24211. https://doi.org/10.1029/2010JD014532

Sun, Q., Zhang, X., Zwiers, F., Westra, S., & Alexander, L. V. (2021). A global, continental, and regional analysis of changes in extreme precipitation. *Journal of Climate*, *34*(1), 243–258. https://doi.org/10.1175/JCLI-D-19-0892.1

Sun, Y., Solomon, S., Dai, A., & Portmann, R. W. (2007). How often will it rain? *Journal of Climate*, *20*(19), 4801–4818. https://doi.org/10.1175/jcli4263.1

Tamarin-Brodsky, T., & Hadas, O. (2019). The asymmetry of vertical velocity in current and future climate. *Geophysical Research Letters*, *46*(1), 374–382. https://doi.org/10.1029/2018GL080363

Tandon, N. F., Zhang, X., & Sobel, A. H. (2018). Understanding the dynamics of future changes in extreme precipitation intensity. *Geophysical Research Letters*, *45*(6), 2870–2878. https://doi.org/10.1002/2017gl076361

Tareghian, R., & Rasmussen, P. (2013). Analysis of Arctic and Antarctic sea ice extent using quantile regression. *International Journal of Climatology*, *33*(5), 1079–1086. https://doi.org/10.1002/joc.3491

Trenberth, K. E., Dai, A., Rasmussen, R. M., & Parsons, D. B. (2003). The changing character of precipitation. *Bulletin of the American Meteorological Society*, *84*(9), 1205–1218. https://doi.org/10.1175/bams-84-9-1205

van Haren, R., van Oldenborgh, G. J., Lenderink, G., Collins, M., & Hazeleger, W. (2013). SST and circulation trend biases cause an underestimation of European precipitation trends. *Climate Dynamics*, *40*(1–2), 1–20. https://doi.org/10.1007/s00382-012-1401-5

Vicente-Serrano, S. M., García-Herrera, R., Peña-Angulo, D., Tomas-Burguera, M., Domínguez-Castro, F., Noguera, I., et al. (2021). Do CMIP models capture long-term observed annual precipitation trends? *Climate Dynamics*, *58*(9–10), 2825–2842. https://doi.org/10.1007/s00382-021-06034-x

Wang, X. L. (2008a). Accounting for autocorrelation in detecting mean shifts in climate data series using the penalized maximal t or F test. *Journal of Applied Meteorology and Climatology*, *47*(9), 2423–2444. https://doi.org/10.1175/2008JAMC1741.1

Wang, X. L. (2008b). Penalized maximal F test for detecting undocumented mean shift without trend change. *Journal of Atmospheric and Oceanic Technology*, *25*(3), 368–384. https://doi.org/10.1175/2007JTECHA982.1

Westra, S., Alexander, L. V., & Zwiers, F. W. (2013). Global increasing trends in annual maximum daily precipitation. *Journal of Climate*, *26*(11), 3904–3918. https://doi.org/10.1175/JCLI-D-12-00502.1

Wolff, M. A., Isaksen, K., Petersen-ØVerleir, A., Ødemark, K., Reitan, T., & Brækkan, R. (2015). Derivation of a new continuous adjustment function for correcting wind-induced loss of solid precipitation: Results of a Norwegian field study. *Hydrology and Earth System Sciences*, *19*(2), 951–967. https://doi.org/10.5194/hess-19-951-2015

Wu, Y., Wu, S. Y., Wen, J., Xu, M., & Tan, J. (2016). Changing characteristics of precipitation in China during 1960-2012. *International Journal of Climatology*, *36*(3), 1387–1402. https://doi.org/10.1002/joc.4432

Supporting Information for "Why has precipitation increased in Norway the past 120 years?"

K. Konstali [1,2], A.Sorteberg [1,2]

[1]Geophysical institute

[2]Bjerknes Centre of Climate Research

[1]Universitetet i Bergen, Geofysisk Institutt, Postboks 7803, 5020 Bergen, Norway

Contents of this file

—————

June 20, 2022, 1:03pm
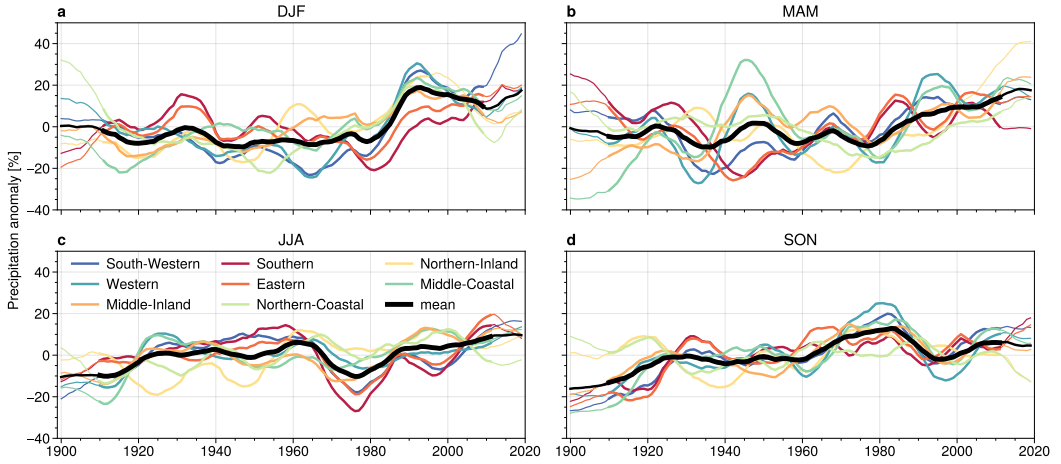
Figure S1. Seasonal 10-year sliding average relative precipitation anomalies for each region relative to the whole time series.

Table S1. Summary table, with mean, standard deviation (std), trend, and correlation for the estimated precipitation from reanalysis (PAP) observed precipitation (OP) and precipitation from reanalysis (P_ERA-20C and P_20CRv3). All values represent the mean over Norway based on annual averages in the common period between the reanalyses, 1979-2010. The trend is multiplied by the length of the period. Correlation is between the respective variable and OP1900.

Product	mean [mm/day]	std [mm/day]	trend [%]	correlation (r)
OP1900	3.1	0.4	20.9	1.00
P_ERA-20C	2.9	0.3	17.3	0.96
P_20CRv3	3.6	0.3	15.2	0.95
$\text{PAP}_{ERA-20C}$	2.0	0.2	24.8	0.93
PAP_{20CRv3}	3.1	0.3	16.9	0.94
PAP_{ERA5}	3.4	0.4	23.1	0.95
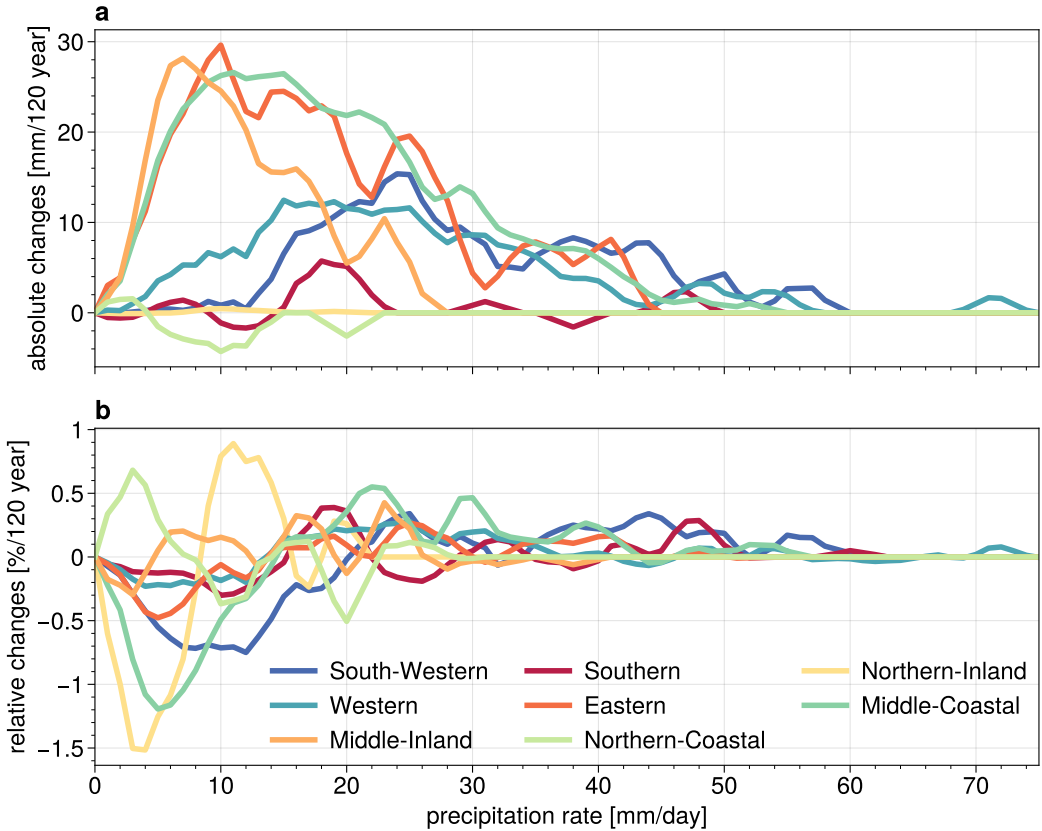
Figure S2. Changes in the contribution of the precipitation rates to the annual mean precipitation in each regions. a) Trend in contribution of the precipitation rates to the annual mean precipitation, in absolute terms [mm/year], b), same as a, but normalized by the annual mean precipitation, thus representing relative changes.

June 20, 2022, 1:03pm

Table S2. Meta-data of the stations. We have included station ID, start date, end date, latitude, longitude, elevation, and quality flag, where 0 represent the stations we have not included in the analysis. For the stations that are merged, we show the IDs of the merged stations as well as the biases (b) between the longest to the shortest time series. id1 correspond to b1 etc.

stationID	startDate	endDate	Lat	Lon	Elev	Flag	id1	id2	id3	b1	b2	b3
SN59450	1957-01-01	2019-12-31	62.15	5.21	75	1						
SN95350	1957-01-01	2015-12-30	70.06	24.99	5	0	SN95400			1.08		
SN87100	1909-09-01	2019-12-31	69.32	16.12	5	1	SN87110			0.83		
SN5350	1899-12-31	2019-12-31	60.39	11.56	147	1						
SN41550	1919-07-01	2019-12-31	58.79	7.35	504	1	SN41560					
SN27720	1957-01-01	2019-12-31	59.12	10.20	34	0	SN27600			1.07		
SN85540	1957-01-01	2019-12-31	68.14	13.61	13	1	SN85560			0.97		
SN50560	1899-12-31	2019-12-31	60.40	5.31	41	1	SN50550	SN50540		0.85	0.93	
SN49750	1957-01-01	2019-12-31	60.42	7.27	748	1	SN49850	SN49800			1.21	
SN800	1957-01-01	2019-12-31	62.25	11.76	670	1	SN810					
SN34600	1899-12-31	2019-12-31	59.10	9.07	82	0	SN34580	SN34620				
SN79740	1899-12-31	2019-11-30	66.51	14.91	155	0	SN79762					
SN15720	1950-08-14	2019-12-31	61.91	7.86	712	1	SN15730					
SN50450	1957-01-01	2019-12-31	60.27	5.33	54	1						
SN4050	1957-01-01	2019-12-31	59.76	11.14	163	1	SN4040					
SN86760	1954-01-01	2019-12-31	68.63	14.46	12	0	SN86750	SN86740				
SN42520	1899-12-31	2019-12-31	58.66	6.94	348	1						
SN58400	1950-01-01	2019-12-31	61.85	6.63	32	1	SN58390			1.04		
SN25590	1941-01-02	2019-12-31	60.53	8.22	795	0	SN25610	SN25630	SN25600			
SN18950	1943-01-01	2019-12-31	59.98	10.67	514	1	SN18960					
SN9100	1899-12-31	2019-12-31	62.13	10.05	709	0	SN9160					
SN12680	1957-01-01	2019-12-31	61.09	10.48	240	0	SN12640	SN12660				
SN42810	1957-01-02	2019-12-31	58.66	6.71	55	1	SN42800					
SN31900	1899-12-31	2019-12-31	59.75	8.81	464	1						
SN96400	1956-08-26	2018-07-30	71.09	28.22	8	0	SN96560					
SN14710	1957-01-01	2019-12-31	61.81	9.02	808	1	SN14711			1.14		

ID	Start Date	End Date	Value1	Value2	N	Flag	Linked Series	Ratios
SN70820	1962-07-01	2019-12-31	64.12	11.73	50	1		
SN81900	1899-12-31	2018-06-01	67.13	16.07	142	1		
SN94130	1957-01-01	2018-08-30	70.40	23.63	38	0	SN94120	0.88
SN45600	1957-01-01	2018-10-26	59.07	6.02	64	1		
SN72650	1957-01-01	2019-12-31	64.48	11.84	26	1	SN72700	0.92
SN19490	1957-01-01	2019-12-31	59.91	10.51	67	1	SN19600 SN19480 SN19610	0.89 0.94 0.86
SN52930	1939-01-01	2019-12-31	60.96	5.43	240	1		
SN46300	1899-12-31	2019-12-31	59.59	6.81	333	1		
SN96920	1899-12-31	2019-12-31	70.08	27.99	21	1	SN96910 SN96931 SN96930	
SN95600	1899-12-31	2019-12-31	70.32	25.55	10	0	SN95590 SN95610	
SN27800	1899-12-31	2019-12-31	59.20	9.96	31	1		
SN41770	1954-01-01	2019-12-31	57.98	7.05	16	1	SN41760	
SN18400	1899-12-31	2019-12-31	59.93	10.77	90	1	SN18700	0.94
SN37750	1957-01-01	2017-06-29	59.17	8.04	303	1	SN37740	
SN63580	1965-07-01	2019-12-31	62.67	9.20	596	1		
SN58780	1957-01-02	2019-12-31	61.92	6.04	34	1	SN58800	
SN55550	1899-12-31	2019-12-31	61.29	7.19	246	1		
SN82840	1957-01-01	2019-12-31	67.53	15.50	27	0	SN82860 SN82850	
SN42720	1899-12-31	2019-12-31	58.41	6.66	75	1		
SN97250	1899-12-31	2019-12-31	69.47	25.48	155	0	SN97251	
SN83300	1916-01-01	2019-12-31	67.92	15.11	31	1		
SN88100	1907-05-01	2019-12-31	68.65	18.24	230	1		
SN84200	1907-01-01	2019-05-20	68.18	17.55	56	1	SN84190	
SN55840	1921-02-02	2019-12-31	61.44	6.77	10	1	SN55830 SN55820	
SN600	1899-12-31	2018-06-29	61.84	11.85	696	1	SN610	1.03
SN43360	1957-01-01	2018-08-20	58.45	6.00	4	1		
SN82530	1957-01-01	2019-12-31	67.54	14.84	15	1	SN82540 SN82560 SN82550	
SN46150	1932-07-01	2019-12-31	59.48	6.28	25	1		
SN8720	1954-01-02	2019-12-31	61.89	10.14	749	1	SN8710	0.95
SN70850	1899-12-31	2019-12-31	64.16	12.47	195	1		
SN19710	1957-01-01	2019-12-31	59.86	10.44	163	1		
SN1650	1899-12-31	2019-12-31	59.30	11.66	113	1		
SN71800	1899-12-31	2019-12-31	64.09	10.49	250	1	SN71810	
SN2610	1957-01-01	2019-12-31	59.89	11.58	135	1	SN2600 SN2650	1.05

SN93700	1931-01-01	2019-12-31	69.00	23.03	307	0	SN93710			0.37
SN46850	1936-10-01	2019-12-31	59.55	5.99	159	1				
SN32900	1899-12-31	2019-12-31	59.50	8.20	573	1	SN32890			
SN69100	1946-01-02	2019-12-31	63.46	10.93	12	1				
SN24860	1899-12-31	2019-12-31	60.57	9.10	164	1	SN24890	SN24880	SN24870	0.90
SN24600	1957-01-01	2019-12-31	60.14	9.60	367	0				
SN47890	1926-01-01	2019-12-31	59.85	6.02	38	1	SN47900			0.96
SN29600	1899-12-31	2019-12-31	60.46	8.75	870	1				
SN18160	1957-01-01	2019-12-31	59.87	10.79	118	0				
SN6040	1919-06-01	2019-12-31	60.62	12.02	184	1	SN6020			
SN11080	1926-01-01	2015-06-29	60.28	11.21	178	1	SN11120			0.94
SN40420	1957-01-01	2019-12-31	59.35	7.34	599	0	SN40400			
SN62500	1919-01-01	2018-01-01	62.86	6.54	11	1	SN62490	SN62480		
SN16610	1923-02-01	2019-12-31	62.11	9.29	973	1	SN16600			
SN91370	1957-01-01	2019-12-31	69.37	20.27	5	1	SN91380	SN91350	SN91360	
SN44520	1962-01-01	2019-12-31	58.76	6.01	288	1				
SN36060	1957-01-01	2019-12-31	58.47	8.76	44	0	SN36110	SN36100		
SN52300	1899-12-31	2019-09-14	60.84	5.93	104	1	SN52290	SN52310		
SN42950	1936-01-01	2019-12-31	58.95	6.92	582	1	SN42940			1.07
SN93300	1906-12-01	2019-12-31	69.59	23.53	377	1	SN93301			
SN13310	1957-01-01	2018-06-29	61.46	10.31	770	1	SN13300			
SN7900	1957-01-01	2019-12-31	62.10	11.05	513	1	SN7920	SN7910		
SN28920	1927-01-01	2019-12-31	60.05	9.15	243	1	SN28921	SN28922		0.99
SN96220	1957-01-01	2019-12-31	70.58	26.99	18	0	SN96210			
SN50300	1957-01-02	2019-12-31	60.39	5.91	408	1	SN50310			
SN44900	1957-01-01	2019-12-31	58.83	6.06	44	1	SN44890	SN44880		1.06
SN3190	1899-12-31	2019-12-31	59.29	11.11	57	1	SN3200			
SN17150	1955-03-02	2019-12-31	59.37	10.80	40	1				
SN67150	1960-08-01	2019-12-31	63.33	10.27	13	1				
SN39690	1919-07-01	2019-12-31	58.67	7.81	212	1	SN39750	SN39710	SN39700	
SN52750	1957-01-01	2019-12-31	60.85	5.21	13	1				
SN27300	1899-12-31	2019-12-31	59.36	10.25	44	1	SN27315	SN27301		0.98
SN62700	1957-01-01	2019-12-31	62.91	7.24	80	1				
SN90450	1920-07-02	2019-12-31	69.65	18.94	100	1				

SN49350	1957-01-01	2019-12-31	60.12	6.56	32	1	SN49351		1.04
SN44560	1953-01-01	2019-12-31	58.88	5.64	7	1			
SN18450	1957-01-01	2019-12-31	59.97	10.79	173	1	SN18420		1.11
SN66850	1957-01-01	2019-12-31	62.60	10.27	549	1			
SN49630	1957-01-01	2019-12-31	60.47	7.07	5	1	SN49631		
SN71280	1957-01-01	2019-12-31	63.69	10.61	138	0	SN71270		
SN25640	1899-12-31	2019-12-31	60.53	8.15	841	1			
SN30530	1957-01-01	2019-12-31	59.57	9.26	34	1			
SN57940	1910-09-16	2019-12-31	61.83	5.67	24	1	SN57930		
SN78610	1957-01-01	2017-12-22	65.83	13.91	439	1			
SN62900	1957-01-01	2019-12-31	62.89	7.39	49	1			
SN52170	1957-01-01	2019-12-31	60.80	6.15	450	1			
SN36200	1936-12-31	2019-12-31	58.40	8.79	12	1			
SN24770	1957-01-01	2019-12-31	60.39	9.57	149	1	SN24710		0.81
SN15430	1911-01-01	2019-12-31	61.72	8.24	700	1			
SN31660	1957-01-01	2019-12-31	60.02	7.91	954	1			
SN23720	1902-08-01	2019-12-31	61.12	8.57	489	1			
SN51470	1899-12-31	2019-12-31	60.65	6.22	328	1			
SN35090	1957-01-01	2019-12-31	58.80	9.10	42	1	SN35080		
SN66070	1957-01-01	2017-07-07	63.29	9.73	84	1			
SN10400	1899-12-31	2019-12-31	62.57	11.38	628	0	SN10380		1.36
SN46610	1928-03-02	2019-12-31	59.65	6.35	5	1			
SN31080	1957-01-01	2019-12-31	60.13	8.70	762	0	SN31100		
SN42160	1954-01-01	2019-12-31	58.11	6.57	14	1			
SN60400	1899-12-31	2019-12-31	62.25	7.24	28	1			
SN77850	1899-12-31	2019-12-31	65.37	14.25	498	1			
SN35200	1899-12-31	2018-09-29	58.89	8.95	240	1	SN35180		1.05
SN58480	1940-01-01	2019-12-31	61.69	6.81	44	1			
SN30370	1899-12-31	2019-12-31	59.45	9.54	460	1	SN30380		
SN20520	1926-01-01	2019-12-31	60.30	10.58	372	1			
SN65450	1957-01-01	2019-12-31	63.52	9.09	20	0	SN65451		
SN25320	1957-01-01	2019-12-31	60.64	8.56	720	1			
SN57870	1899-12-31	2019-12-31	61.89	5.55	32	1	SN57860	SN57850	
SN74320	1957-01-01	2019-12-31	64.73	12.82	143	1	SN74300	SN74350	1.06

June 20, 2022, 1:03pm

ID	Start	End					Label	Value
SN15660	1899-12-31	2019-12-31	61.90	8.17	432	1		
SN24210	1957-01-01	2019-12-31	60.24	9.93	140	1		
SN12520	1901-01-01	2017-09-28	60.79	10.96	205	1		
SN58070	1957-06-01	2019-12-31	61.79	6.18	51	0		
SN57810	1939-01-01	2019-12-31	61.77	5.30	16	1	SN57800	1.00
SN37650	1957-01-01	2018-06-29	59.01	8.27	287	1		
SN39220	1899-12-31	2019-12-31	58.22	7.89	151	1		
SN10600	1957-01-01	2019-12-31	62.67	11.45	685	1		
SN86950	1957-01-01	2019-12-31	68.91	15.21	18	1		
SN73250	1943-03-17	2019-12-31	64.24	13.77	370	1		
SN61820	1959-01-01	2019-12-31	62.66	8.11	14	1		
SN22720	1899-12-31	2019-12-31	60.62	9.72	503	0	SN22730	
SN52860	1950-06-03	2019-12-31	61.03	5.38	38	1		
SN48500	1936-12-15	2019-12-31	59.99	6.03	75	1		
SN65600	1957-01-01	2014-01-01	63.62	8.72	23	1		
SN60800	1957-01-01	2019-12-31	62.48	6.82	5	1		
SN63420	1957-01-01	2019-12-31	62.68	8.55	6	1		
SN6460	1957-01-01	2019-12-31	60.69	12.40	295	1	SN6440	
SN99450	1899-12-31	2019-12-31	69.45	30.07	28	1	SN99460	
SN45900	1954-01-01	2019-12-31	59.18	6.07	1	0	SN45880	SN45870
SN80600	1954-01-01	2019-12-31	66.76	12.48	19	1	SN80610	
SN17250	1911-02-28	2019-12-31	59.43	10.67	31	1	SN17251	
SN56960	1943-11-01	2019-12-31	61.42	6.38	311	1		
SN42650	1957-01-01	2019-12-31	58.28	6.65	5	1		
SN87550	1957-01-01	2019-12-31	68.83	16.49	14	1	SN87640	
SN53080	1899-12-31	2019-12-31	61.08	6.58	30	1	SN53070	0.99
SN44160	1957-01-01	2018-08-30	58.69	5.64	19	1		
SN15480	1957-01-01	2019-12-31	61.88	8.47	374	0		
SN68420	1899-12-31	2019-12-31	63.06	11.57	302	1		
SN80200	1922-12-01	2019-12-31	66.39	13.18	115	1		
SN20250	1957-01-01	2018-06-29	60.11	10.29	66	1		
SN63100	1900-09-07	2019-12-31	62.69	8.42	47	1		
SN76100	1957-01-01	2019-12-31	65.12	12.37	24	1		
SN61350	1957-01-01	2019-12-31	62.57	7.68	20	1	SN61340	

ID	Start	End	V1	V2	N	Flag	Ref
SN93900	1913-04-01	2019-12-31	68.76	23.54	382	0	
SN35340	1957-01-01	2019-12-31	58.72	9.21	36	1	SN35350
SN38450	1899-12-31	2017-09-19	58.52	8.35	85	1	SN38445
SN1230	1899-12-31	2019-12-31	59.12	11.39	3	1	
SN9870	1957-01-01	2019-12-31	62.43	10.43	700	1	
SN84070	1964-02-01	2019-12-31	68.33	16.79	53	1	
SN56320	1957-01-01	2019-12-31	61.11	5.54	31	1	
SN52220	1957-01-01	2018-06-29	60.83	6.26	579	1	
SN1080	1957-01-01	2019-06-29	59.04	11.04	17	1	
SN98550	1899-12-31	2019-12-31	70.37	31.10	10	1	
SN23160	1931-01-02	2017-12-30	60.92	9.29	639	1	
SN44800	1899-12-31	2019-12-31	58.82	5.92	230	1	
SN53700	1957-01-01	2019-12-31	60.90	7.20	15	1	
SN39040	1946-01-02	2019-12-31	58.20	8.08	12	1	
SN78250	1957-01-01	2019-12-31	66.07	12.91	53	1	
SN73800	1907-01-01	2019-12-31	64.68	13.65	376	1	
SN37500	1957-01-01	2019-12-31	59.32	8.15	492	1	
SN50150	1957-01-01	2019-12-31	60.05	5.90	45	1	
SN22840	1957-01-01	2019-12-31	60.83	9.49	628	1	
SN5650	1957-01-01	2019-12-31	60.22	12.03	175	1	SN5590
SN54600	1899-12-31	2019-12-31	61.11	8.04	806	1	
SN14550	1957-01-01	2019-12-31	61.92	9.01	823	1	
SN69960	1962-07-01	2017-12-15	63.72	11.54	182	1	
SN64900	1957-01-01	2019-12-31	63.04	9.22	228	1	
SN57480	1899-12-31	2019-12-31	61.53	6.06	237	1	
SN56520	1899-12-31	2019-12-31	61.23	5.43	85	1	
SN44480	1902-10-01	2019-12-31	58.69	5.98	263	0	
SN45350	1899-12-31	2019-12-31	59.06	6.65	5	1	
SN47820	1961-09-01	2019-12-31	59.86	6.28	178	1	
SN33250	1899-12-31	2019-12-31	59.71	8.03	719	1	
SN47300	1943-01-02	2019-12-31	59.31	4.87	55	1	
SN43810	1957-01-01	2019-12-31	58.76	6.37	311	1	
SN24960	1963-12-01	2019-12-31	60.72	8.95	542	1	
SN700	1957-01-01	2019-12-31	61.89	12.05	672	1	

SN82290	1954-01-01	2019-12-31	67.27	14.36	11	1		
SN18500	1899-12-31	2019-12-31	60.05	10.69	360	1		
SN13700	1957-01-01	2018-06-29	61.42	9.54	752	1		
SN69550	1899-12-31	2019-12-31	63.49	11.35	174	1		
SN68270	1960-08-01	2019-12-31	63.23	10.44	173	1		
SN92350	1965-08-02	2019-12-31	69.84	21.90	20	1		
SN11900	1899-12-31	2019-12-31	60.95	10.60	190	1		
SN41480	1899-12-31	2019-12-31	58.62	7.41	268	1		
SN60500	1930-06-18	2019-12-31	62.23	7.42	11	1		
SN1950	1899-12-31	2019-12-31	59.48	11.65	123	1		
SN58320	1899-12-31	2019-12-31	61.71	6.61	315	1		
SN3780	1957-01-01	2019-12-31	59.64	11.05	144	1		
SN38600	1899-12-31	2019-12-31	58.63	8.29	245	1		
SN51250	1957-01-01	2019-12-31	60.69	5.96	316	1		
SN56400	1957-01-01	2019-12-31	61.01	4.67	3	1		
SN32780	1957-01-01	2019-12-31	59.14	9.27	113	1		
SN38800	1926-01-01	2019-12-31	58.79	8.23	220	1		
SN30860	1960-09-01	2019-12-31	59.89	9.06	514	1		
SN89500	1957-01-01	2017-04-21	68.86	18.34	114	1		
SN37230	1944-05-25	2019-12-31	59.03	8.52	252	1		
SN47090	1958-10-01	2019-01-01	59.50	5.63	5	1	SN47120	
SN58960	1899-12-31	2019-12-31	62.00	6.65	349	1		
SN75100	1909-06-09	2019-12-31	64.84	11.95	44	1		
SN55730	1899-12-31	2019-12-31	61.33	6.93	421	1		
SN23560	1899-12-31	2019-12-31	61.24	8.86	754	0		
SN71550	1954-11-01	2019-12-31	63.70	9.61	10	1		
SN34900	1899-12-31	2019-12-31	59.26	8.77	464	1		
SN72250	1957-01-01	2014-06-29	64.33	11.54	62	1		
SN4730	1965-09-01	2019-12-31	60.16	11.11	200	1	SN4740	1.03
SN71900	1957-01-01	2019-12-31	64.24	10.33	12	1		
SN31410	1925-01-01	2019-12-31	59.88	8.67	258	1		
SN60990	1958-07-02	2019-12-31	62.56	6.12	22	1		
SN89350	1946-05-31	2019-12-31	69.06	18.54	76	1		

Paper II

Global attribution of precipitation to weather features

Global attribution of precipitation to weather features

Kjersti Konstali,[a] Clemens Spensberger,[a] Thomas Spengler,[a] Asgeir Sorteberg,[a]

[a] *Geophysical Institute, University of Bergen, and Bjerknes Centre for Climate Research, Bergen,*
Norway

Corresponding author: Kjersti Konstali, kjersti.konstali@uib.no

ABSTRACT: Weather features, such as extratropical cyclones (ETC), atmospheric rivers (AR), and fronts, contribute to substantial amounts of precipitation globally. However, previous estimates of how much these individual features contribute to precipitation are very sensitive to subjectively chosen metrics. Furthermore, there is no information on how these weather features contribute to precipitation poleward of 60° latitude. To alleviate these shortcomings, we introduce a more robust attribution method applicable at all latitudes. Based on ERA5, we present the first global climatology of the contributions from ETCs, fronts, moisture transport axes (MTA; AR-like features), and cold air outbreaks, as well as their combinations to summer and winter precipitation as well as extreme precipitation. Most of the precipitation in the midlatitudes relates to the combination of ETC, Fronts, and ARs, while in polar regions, most precipitation occurs within the ETC-only category. Extreme precipitation events in all extratropical regions are predominantly associated with the combination of ETCs, fronts, and MTAs. In the midlatitudes, the combination of ETCs, fronts, and MTAs occurs almost four times as often during extreme events compared to regular events.

Extratropical cyclones (ETC), fronts, and atmospheric rivers (AR) comprise much of the daily weather and contribute substantially to precipitation in the midlatitudes (Catto et al. 2012; Hawcroft et al. 2012; Utsumi et al. 2017; Hénin et al. 2019; Rüdisühli et al. 2020; Solari et al. 2022). They also contribute significantly to the occurrence of extreme precipitation events (Pfahl and Wernli 2012; Catto and Pfahl 2013; Dowdy and Catto 2017). As these features differ in dynamical origin and evolution, their associated precipitation characteristics in terms of frequency and intensity as well as spatial distribution are expected to differ. To gain further insight into the precipitation mechanisms associated with these weather features, we introduce a precipitation attribution method and present a climatology for the period 1979-2020 using ERA5 (Hersbach et al. 2020).

ETCs contribute to more than 50% of the precipitation in the northern hemisphere (NH) (Hawcroft et al. 2012), and fronts to more than 40% (Catto et al. 2012). The contribution of fronts is largest along the stormtracks, where up to 80% of the precipitation is associated with fronts (Catto et al. 2012; Hénin et al. 2019). Moreover, fronts and ETCs are connected to 90% and 80% of extreme precipitation events in the midlatitudes, respectively (Pfahl and Wernli 2012; Catto and Pfahl 2013), and more than 50% of the extreme events are associated with a co-occurrence of fronts and ETCs in the stormtrack regions (Catto and Pfahl 2013; Dowdy and Catto 2017). In addition to fronts and ETCs, ARs have also been shown to be important for extreme precipitation events (Lavers and Villarini 2013; Ralph et al. 2006; Viale et al. 2018; Guan et al. 2023) as well as for seasonal precipitation in different regions worldwide (i.e., Gershunov et al. 2017; Nash et al. 2022; Reid et al. 2022). However, no studies have considered all of these weather features in conjunction with each other, and thus their relative contributions to climatological and extreme precipitation remain unclear.

Despite the importance of ETCs, fronts, and ARs for extreme precipitation, it is unknown how much they contribute climatologically to precipitation at higher latitudes. Catto et al. (2012) argued that fronts seldom occur in the polar regions and are, therefore, insignificant for annual accumulated precipitation. However, studies on extreme precipitation in the Southern Ocean (Papritz et al. 2014), over coastal Antarctica (Gorodetskaya et al. 2014; Terpstra et al. 2021; González-Herrero et al. 2023), Svalbard (Serreze et al. 2015), and the Canadian Arctic (Serreze et al. 2022) show that ETCs, fronts, and ARs contribute substantially to extreme precipitation. Besides, extreme precipitation events in coastal Antarctica contribute substantially to the inter-annual variability of precipitation

(Turner et al. 2019), highlighting the relevance of weather features for precipitation on longer time scales.

Investigating the importance of ARs in the polar regions is challenging as most AR detection algorithms are tuned towards the midlatitudes and rely on an integrated water vapour transport (IVT) threshold that is commonly too high for polar regions (Rutz et al. 2019). To alleviate this issue, we use a modified AR detection scheme designed to work seamlessly at all latitudes (Spensberger et al. 2023). In addition, we complement the catalogue of weather features with Cold Air Outbreaks (CAO) that occur frequently over high-latitude oceans (Papritz et al. 2015; Papritz and Spengler 2017). CAOs are associated with an intense hydrological cycle (Papritz and Sodemann 2018), but their climatological importance for precipitation has not been investigated.

A limitation of previous studies is their sensitivity to a subjectively chosen "radius of influence" surrounding the weather feature. All precipitation within this prescribed radius is attributed to the respective weather feature (see overview in table 2). For ETCs, Hawcroft et al. (2012) used a $10°$ radius around the ETC's center and considered all precipitation within this radius to belong to the ETC. Changing this radius by $\pm 2°$ changed the attributed precipitation over Europe from 58% to 83%, i.e., by 25%.

Similar to ETCs, frontal precipitation is also highly sensitive to the radius. Changing the radius from $2.5°$ to $10°$ changed the percentage of precipitation attributed to fronts by more than 50% in the midlatitudes (Catto et al. 2012). Furthermore, different studies employ different radii for the same feature. For fronts, Catto et al. (2012) and Hénin et al. (2019) chose $5°$ and $6°$, respectively, despite Hénin et al. (2019) having both higher spatial and temporal resolution. Utsumi et al. (2017) used 500 km, and Rüdisühli et al. (2020) included additional categories, such as near-frontal (within 300 km) and far-frontal (300-600 km). Despite the high sensitivity to the radius for the attributed precipitation, there is no consensus on which distances to use.

The fact that different weather features are associated with different spatial scales further complicates the choice of an appropriate "radius of influence". Utsumi et al. (2017) addressed this issue by having different distance thresholds for ETCs (1000 km) and fronts (500 km). However, choosing different distances for different weather features complicates the attribution when considering several weather features. In addition, weather features can be associated with different characteristic spatial scales in different locations (Hawcroft et al. 2012). It is therefore highly

4

desirable to avoid explicit distance criteria altogether – to avoid both the inherent sensitivity as well as different metrics across the considered weather features.

Inconsistencies due to using a blend of observational and reanalysis data can also be problematic. For example, the co-occurrence of extreme precipitation over India in observations and ERA-Interim is only 15-20% (Sørland and Sorteberg 2015). Thus, blending observations and re-analysis may yield physical inconsistencies with discrepancies between the precipitation-generating mechanism and the precipitation. Although the precipitation in ERA5 is closer to observations than ERA-Interim (Nogueira 2020), there are known dry and wet biases in ERA5 during summer (Lavers et al. 2022). Observations are also limited temporally and spatially; for instance, both Utsumi et al. (2017) and Dowdy and Catto (2017) only had 10 years of data coverage. The limited temporal coverage inhibits robust estimates of extreme events, i.e., the 99.9th percentile in 10 years of data with 6-hourly resolution yields less than 20 events per grid point, which is insufficient to obtain robust results.

To alleviate the challenges due to the sensitivity to a subjectively chosen radius of influence and the lack of information at higher latitudes, we introduce a new method to attribute precipitation to weather features that is applicable at all latitudes. The method does not rely on a fixed distance between the weather feature and precipitation. For consistency and better temporal and spatial coverage, we use data from ERA5 (Hersbach et al. 2020) for the period 1979-2020. The extended temporal coverage and resolution yield more robust estimates of precipitation attributed to weather features, particularly for extreme events. We present the first global climatology attributing mean and extreme precipitation to ETCs, fronts, ARs, and Cold Air Outbreaks (CAO), as well as combinations thereof.

1. Data

We use the ERA5 reanalysis for the period 1979-2020 on a $0.5° \times 0.5°$ grid with 3-hourly temporal resolution. Precipitation is derived from short-term forecasts initialized twice daily at 06 and 18Z. To obtain 3-hourly accumulated precipitation, we use the aggregated precipitation between 3h and 15h lead time and use the 3h aggregation interval preceding each analysis time step. We only consider wet events, defined as time steps with precipitation greater than 0.1 mm/3hr, as this

roughly equals the minimum amount it has to rain continuously throughout the day to be considered a wet day (1 mm/day, Klein Tank et al. 2009).

Using this threshold, we consider 97% of the total global precipitation. In the northern hemisphere (NH) high latitudes ($> 60°$N) we include slightly less precipitation, 92%, dropping to 78% poleward of 85°N. Over the Antarctic continent, we consider less than 10% of the precipitation, but values increase to 80% along the coast. Contributions are calculated as fractions of precipitation for wet events only. The relative contribution from weather features is mostly insensitive to the chosen precipitation threshold (not shown).

We define a time step where the 3-hourly accumulated precipitation exceeds the 99.9th percentile as an extreme precipitation event, where we use all timesteps independent of precipitation amount (as recommended by Schär et al. 2016). Specifically, we use the average of the annual 99.9th percentiles calculated individually for every grid point. With 3-hourly data for 40 years, the 99.9th percentile yields 117 time steps over the entire period. However, because of the annual averaging of the percentile, we end up with 149 events on average in every grid point, which is sufficient for a robust estimate. In the midlatitudes, 80% of these events are independent (separated by more than one 3-hour timestep), whereas half of them are independent in the subtropics.

2. Detecting Weather Features

We use the Wernli and Schwierz (2006) algorithm, including the modifications described in Sprenger et al. (2017), to detect ETCs. The algorithm searches for minima in sea level pressure and detects the outermost contour of each cyclone. Compiling a climatology of cyclone occurrences, the stormtracks in both hemispheres are clearly visible for DJF and JJA (Figure 1a,b)

Frontal volumes are detected following Spensberger and Sprenger (2018), where the gradient of equivalent potential temperature exceeds 4.5×10^{-5} K/m. We define the intersection of the frontal volumes at 850 hPa as frontal objects for our attribution. We mask out regions with elevations > 1500 m, because orography often causes spurious temperature gradients. Fronts occur mainly along the stormtracks, although more infrequent than ETCs (Figure 1 c,d).

We use objectively identified moisture transport axes (MTA; Spensberger et al. (2023)), which can be regarded as AR-like features. For a more in-depth comparison between MTAs and ARs, see Spensberger et al. (2023). The algorithm creates an axis tracing the line of maximum vertically

6

integrated total water transport and, unlike most AR detection algorithms, does not require a fixed integrated water vapour transport (IVT) threshold (Shields et al. 2022). Thereby, the MTA algorithm is applicable across all latitudes without re-setting a threshold. This is particularly useful for higher latitudes, where sufficient moisture seldom exceeds the typical IVT thresholds that are tuned towards the mid-latitudes. Although some algorithms use local thresholds to accommodate for these geographic variations (Shields et al. 2022), fixed thresholds also cause problems for longer time periods, as they could lead to a higher detection of ARs in a changing climate, such as for the used period 1979-2020.

We construct the MTA climatology by masking the grid point where an MTA occurs and thereafter compute the average frequency of occurrence at the grid point. Climatological MTA occurrences pinpoint preferential pathways in the tropics, including monsoonal circulations (e.g., India and Somalia), the intertropical convergence zone (ITCZ), and the South American low-level jet (Figure 1 e,f, see also Spensberger et al. (2023) for a more detailed description). In addition, MTAs often occur in the stormtrack regions. Note that because MTAs are lines and not areas, they cover substantially smaller areas than both fronts and ETCs. The frequency of MTAs in an individual grid point is accordingly small.

Lastly, we detect CAOs, where we use a CAO index greater than 3K as our CAO mask. The CAO index is defined as the potential temperature difference between 850 hPa and the sea surface temperature (SST) (e.g., Papritz and Spengler 2017). To include the leading edge of the CAO, we choose a lower CAO index than the more conventional 4K (Papritz and Spengler 2017). However, due to the strong gradient of the CAO index across the leading edge, the precipitation attributed to CAOs is not sensitive to this threshold (not shown). CAOs occur only in the winter hemisphere and more often in the Northern than the Southern Hemisphere (Figure 1g,h). Because we use the SST and not the skin temperature, we can, by definition, not have CAO conditions over land.

Considering all weather features in synthesis, at least one of the weather feature is present in the stormtrack regions for more than 50% of the time steps both during JJA and DJF (Figure 1i,j). In DJF over the warm, western boundary currents, all ETCs, MTAs, fronts, and CAOs frequently occur in the same region, causing a weather feature to be present for more than 90% of the time steps. In contrast to the midlatitude stormtrack regions, weather features are only present up to 10% of the time in the subtropics. Weather features are also relatively rare in the Arctic in DJF

¹⁶⁷ (occurrence < 10%) except in the Barents Sea and Fram Strait, where they occur more than 50%
¹⁶⁸ of the time.

¹⁷² *a. Attributing precipitation to weather features*

¹⁷³   Previous studies attributed precipitation to a weather feature if the precipitation occurred within
¹⁷⁴ a certain distance from the weather feature (Catto et al. 2012; Hénin et al. 2019; Dowdy and Catto
¹⁷⁵ 2017; Rüdisühli et al. 2020; Hawcroft et al. 2012; Utsumi et al. 2017). We take another approach
¹⁷⁶ and organize precipitation into precipitation objects using a watershed algorithm (Beucher and
¹⁷⁷ Lantuejoul 1979), where individual objects feature a precipitation maximum. Two maxima belong
¹⁷⁸ to the same precipitation object if they occur closer than the minimum separation distance of 750
¹⁷⁹ km (as illustrated by the grey line in Figure 2b), which we choose based on the length scales used
¹⁸⁰ to attribute precipitation to ETCs and fronts (Utsumi et al. 2017).

¹⁸¹   Considering a typical synoptic situation (Figure 2a), we first attribute all precipitation occurring
¹⁸² within the CAO mask, because precipitation within CAOs tends to be relatively weak without
¹⁸³ clearly defined local maxima (Figure 2a,b). Subsequently, the watershed algorithm yields distinct
¹⁸⁴ precipitation objects (Figure 2c), each featuring a precipitation maximum (Figure 2b). Each precip-
¹⁸⁵ itation object is attributed to the weather features intersecting the precipitation object (Figure 2d).
¹⁸⁶ Thereby, our method is independent of the distance between the precipitation and the weather
¹⁸⁷ feature. Considering all permutations of our weather features (ETCs, Fronts, and MTAs) yields ten
¹⁸⁸ different precipitation categories with different contributions to annual precipitation (Table 1), with
¹⁸⁹ MTA, ETC/MTA/front, and ETC featuring the highest attributions globally, in the midlatitudes,
¹⁹⁰ and in the polar regions in both hemispheres, respectively.

²⁰²   As attributions are sensitive to the chosen distance threshold, we calculated the amount of
²⁰³ precipitation attributable to all the different combinations of ETCs with varying the minimum
²⁰⁴ separation distance, i.e., how far apart the local maxima must be to yield independent precipitation
²⁰⁵ objects (± 33%, i.e., 500 km and 1000 km) for the IPCC climate reference regions (Iturbide et al.
²⁰⁶ 2020): the North Atlantic as the North Atlantic region, and Northern Europe combined with
²⁰⁷ Western Central Europe for Europe. While Hawcroft et al. (2012) showed that the precipitation
²⁰⁸ attributable to ETCs over Europe and the North Atlantic increased by approximately 30% when the
²⁰⁹ distance threshold was varied by 25%, our results are only half as sensitive. Overall, the sensitivity

8
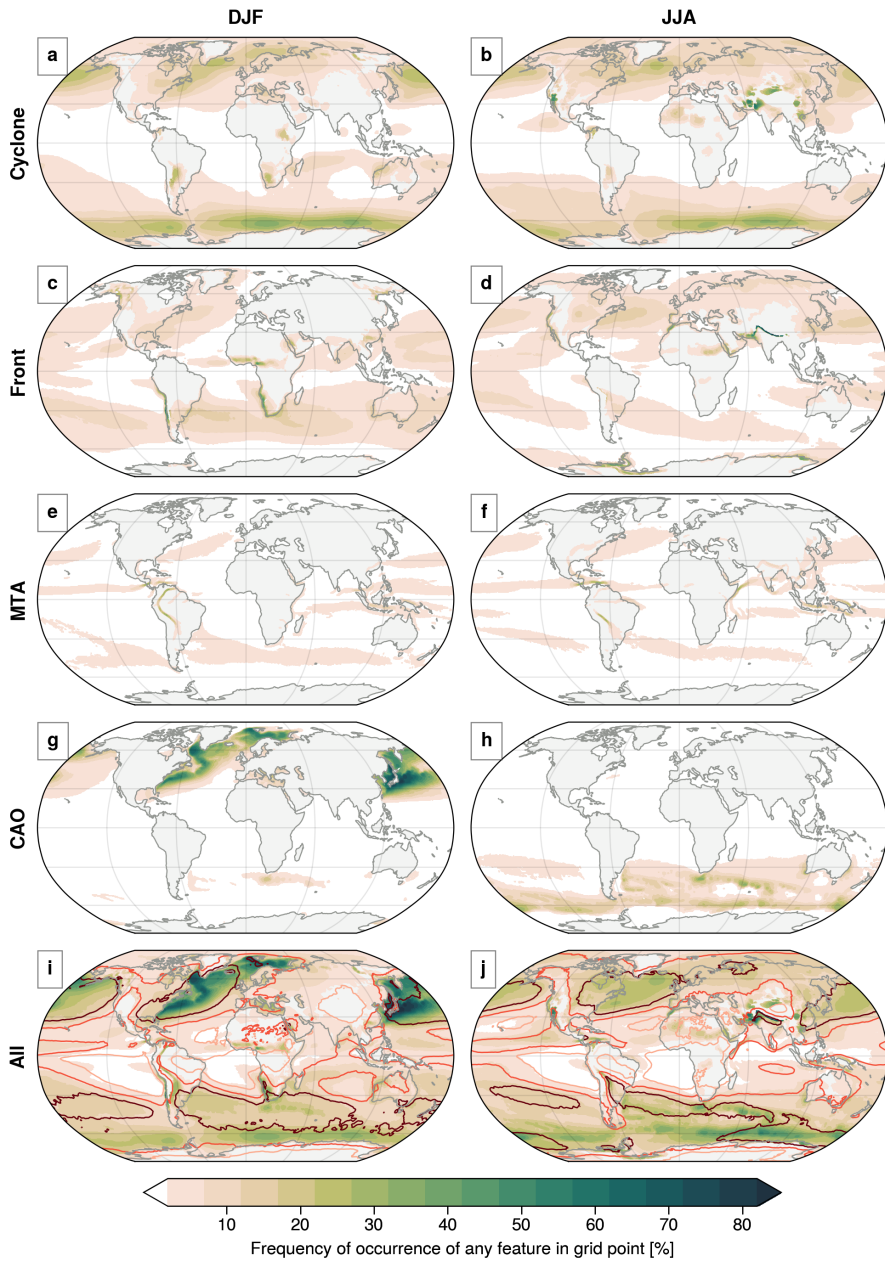
FIG. 1. Frequency of occurrence for DJF (left panels) and JJA (right panels) of ETCs (a,b), fronts (c,d), MTAs (e,f), CAOs (g,h), and their combined occurrence (i,j). Contours in (i,j) mark the percentage of how much precipitation is attributed with contour intervals of 30%, 70% and 90%, from light to dark red.
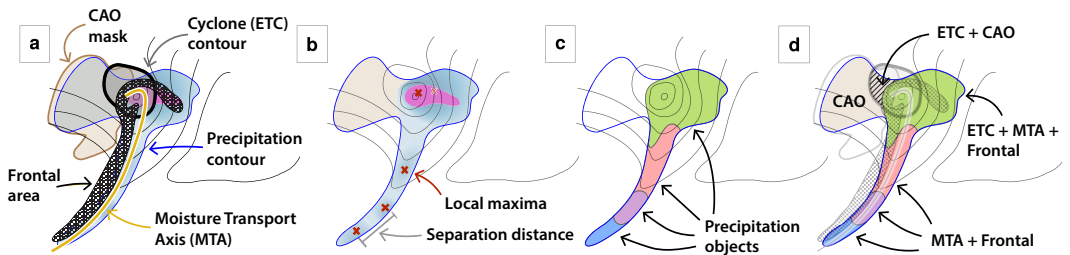
FIG. 2. Schematic illustrating the attribution method. a) Typical synoptic situation with 0.1 mm/3hr precipitation contour (blue contour), precipitation intensity (blue-to-pink shading), and sea level pressure (black lines). A front (checkered area) wraps around the cyclone center (thick, black contour) with a moisture transport axis ahead of the front (yellow line) and a CAO behind the cyclone (brown contour). b) We first attribute the precipitation occurring within the CAO (brown). The watershed algorithm then localizes maxima in the precipitation field (red crosses) that are set apart by a separation distance (grey line). c) The algorithm then returns precipitation objects (coloured patches). d) Each object is attributed to the feature, or combination of features, intersecting the object.

TABLE 1. Overview of the attributed precipitation, including abbreviations of the different precipitation categories, and their relative contribution to global, midlatitude (30°-60°), as well as high latitude precipitation on the NH and SH.

Weather Features	Abbreviation	Contribution			
		Global	Midlatitudes	NH > 60°N	SH > 60°S
CAO	CAO	1.1%	2.6%	3.1%	2.1%
ETC and CAO	CCAO	0.2%	0.4%	0.8%	0.5%
ETC	C	6.9%	9.6%	24.5%	30.4%
Front	F	6.5%	3.7%	6.2%	4.3%
MTA	A	20.8%	8.4%	3.1%	3.7%
MTA and Front	AF	15.5%	20.6%	5.4%	4.1%
ETC and MTA	CA	6.9%	9.5%	7.5%	10.1%
ETC and Front	CF	3.9%	5.5%	14.8%	17.1%
ETC, MTA, and Front	CAF	13.2%	28.2%	16.3%	14.8%
None	Unclassified	25%	11.5%	18.4%	12.9%

of our attribution to varying the minimum separation distance by ±33% over the period 2000-2010 is considerably less than for conventional distance thresholds (Table 2).

Catto et al. (2012) varied the search box size from the precipitating grid cell to a weather feature from 5° to 10°, yielding a variation of 17% in attributable precipitation to fronts in the

midlatitudes. In contrast, when we increase the minimum separation distance from 500 km to 1000 km, the precipitation attributable to fronts (all combinations including fronts) only increases by 11%. Utsumi et al. (2017) calculated the sensitivity to varying the radii of ETCs and fronts by ±25% in three regions (Table 2). At 60°, when averaging across the regions, we find our results to be approximately half as sensitive (11%) compared to Utsumi et al. (2017). However, unlike Utsumi et al. (2017), our maximum differences do not necessarily occur at 60°. Our sensitivities are comparable to those of Utsumi et al. (2017), varying at most by 25%, if choosing the location of the maximum sensitivity (at 64°N, 49°N, and 49°N in the different regions, respectively). However, note that we vary the distance relatively more than Utsumi et al. (2017).

Even though we classify 75% of the precipitation during wet events globally, we consistently attribute less precipitation to weather features than previous studies (Table 2). This can partly be explained by our higher temporal resolution, which leads to less overlap between the precipitation and the feature, and our stricter distance criterion. Lastly, some discrepancies result from different detection methods for the various weather features. For instance, Soster and Parfitt (2022) attributed almost 100% of the precipitation in the North Atlantic to fronts. However, they detected fronts more than twice as often in ERA5 (20-23% vs 8%) and considered a 5° search box around the precipitating grid box.

Despite the differences compared to previous studies, our results fall within the reported sensitivity ranges. Notably, the 90% attributed precipitation contour extends well beyond the 90% contour of occurrence of weather features, signifying a strong relationship between the precipitation and the considered weather features (Figure 1 i,j). If the opposite was true, i.e., if the weather features occur more often than the attributed precipitation amount, it would suggest that the occurrence of these weather features would be inconsequential for precipitation. Our results, therefore, confirm the importance of ETCs and fronts, as well as CAOs and ARs, for precipitation.

b. Case study

We illustrate the performance of our method for a case study on 1 January featuring an intensifying ETC east of Nova Scotia (C1), with the ETC (magenta), front (blue), and MTA (yellow) almost being collocated (Figure 3a). A CAO (brown) is evident behind the frontal zone as the ETC draws cold air from the continent over the relatively warm ocean. Although the precipitation does not

11

TABLE 2. Sensitivities of attribution methods to the respective distance thresholds. Hawcroft et al. (2012)
used a fixed radius around the ETCs, Catto et al. (2012) searched for fronts in the vicinity of the precipitation,
and Utsumi et al. (2017) used different radii surrounding ETCs and fronts. Sensitivities are given both at 60°N
and the location of maximum sensitivity for the three regions in Utsumi et al. (2017). Letters mark the different
precipitation categories used to calculate the sensitivity. See text for details.

Region	Hawcroft et al. (2012): ETC			ETC combinations	(C + CA + CF + CAF)	
	Radius (°)			Separation distance (km)		
	10	12	14	500	750	1000
Europe DJF	58%	73%	83%	46%	52%	57%
North Atlantic DJF	54%	71%	81%	47%	55%	62%
	Catto et al. (2012): Fronts			**Front combinations**	(F + CF + AF + CAF)	
	Search box (°)			Separation distance (km)		
	2.5	5	10	500	750	1000
Midlatitudes (30°-60°)	31%	68%	86%	34%	40%	45%

	Utsumi et al. (2017): Fronts and ETC			**C + CA + CF + CAF + AF + F**					
	@60N (max)			@60N			@max		
	Radius, fronts / ETC (km)			Separation distance (km)			Separation distance (km)		
	375 / 750	500 / 1000	625 / 1250	500	750	1000	500	750	1000
50°E - 100°E	70%	80%	90%	64%	70%	76%	22%	35%	47%
110°E - 160°E	64%	78%	87%	60%	67%	73%	44%	56%	65%
100°W - 60°W	70%	81%	90%	74%	78%	82%	30%	40%	49%

directly overlap with all the features, most of the precipitation is associated with the category CAF
(Figure 3c, pink) and occurs along the front and in the ETC's warm sector. The remainder of the
precipitation in the vicinity of the ETC occurs in the CAO and within the ETC contour, thus being
classified as CCAO (salmon) with substantially weaker intensity than in CAF.

Over the ensuing 42 hours, the cyclone (C1) moved to the southwest of Iceland (Figure 3b). The
front and the MTA have detached from the center of the ETC and stretch across most of the plot
domain, collocated with a band of precipitation. The precipitation along the warm front and parts
of the cold front is attributed to CAF (pink), while the precipitation along the remainder of the cold
front belongs to AF (Figure 3d, green).

With ETCs typically originating from the western side of the ocean basins, the frontal zone and
MTA generally occur within, or in the vicinity of, the ETC contour at the incipient stage of the
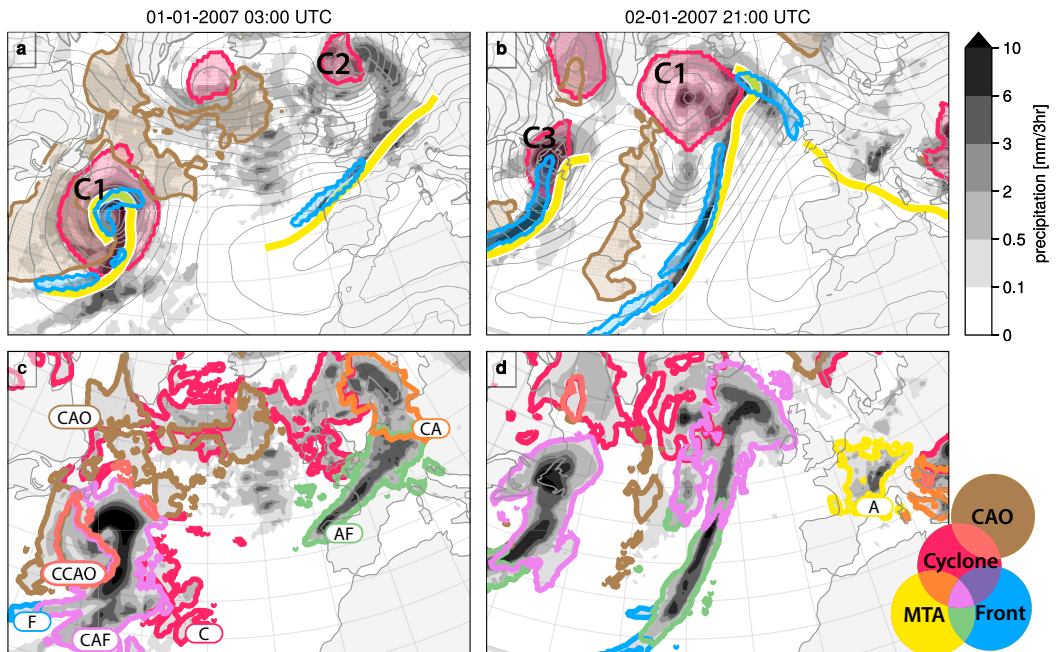
FIG. 3. Top panels (a,d) show precipitation (shading), mean sea level pressure (contours), MTAs (yellow lines), the outermost contour of the ETC (magenta), fronts (blue), and CAO mask (brown). The labelled ETCs are discussed in the text. The bottom panels (c,d) show attributed precipitation: CAO precipitation (brown), CCAO (salmon), C (magenta), CAF (pink), AF (green), A (yellow), and CA (orange), as indicated by the colour legend. Precipitation outside the coloured contours is unclassified.

development (i.e., as in C1 in Figure 3a, and C3 in Figure 3b). As ETCs mature, the front and MTA detach from the center of the ETC (i.e., as in C1 in Figure 3b and C2 in Figure 3a), with the front still providing a lifting mechanism yielding a band of precipitation stretching along the entire front. Thus, mature and decaying ETCs are more likely to have precipitation falling within the F, A, and AF categories than ETCs in their early stages of development.

3. Global climatology of precipitation attributed to weather features

a. Midlatitudes

Over the oceans, the stormtrack regions dominate with CAF, contributing up to 60% in DJF (Figure 4i) despite ETCs occurring less than 30% of the time (Figure 1a) and fronts and MTAs

being even less frequent (Figure 1c,e). The contribution of CAF in the stormtrack regions is relatively higher in the NH than in SH, and it is generally largest over the western part of the ocean basins and gradually decreases towards the east. Consistent with AF occurring along trailing cold fronts (Figure 3), the contribution from AF is displaced equatorward relative to the contribution from CAF (Figure 4f). The contribution of weather features occurring in isolation is negligible in the stormtrack regions.

On average, CAF is associated with the most intense precipitation (Figure 5). The mean precipitation intensity associated with CAF is more than 3.5 mm/3hr over the Gulf Stream region and more than 4 mm/3hr over the Kuroshio extension. AF is associated with slightly weaker intensities, approximately 1 mm/3hr less than CAF, but unlike the difference in contribution between CAF and AF, there is no equatorward shift in the precipitation intensities of AF. The intensities associated with precipitation occurring by weather features occurring in isolation (C, A, and F) are substantially weaker than the intensities for co-occurring features, with a maximum of 1 mm/3hr.

The maximum precipitation amount in DJF occurs over the Gulf Stream and Kuroshio extension region, but does not coincide with the maximum contribution from CAF, which occurs closer to the continents (Figure 4i). This offset in location is due to CAO precipitation that contributes to approximately 15% of the precipitation over the warm western boundary currents (Figure 4g). This signal is not visible in the SH stormtracks in JJA, consistent with CAOs contributing relatively less to the precipitation in the SH stormtracks compared to the NH stormtracks (Figure 6g).

The fraction of attributed precipitation to CAOs is considerably lower than their frequency (Figure 4g, Figure 1g), indicating weak precipitation intensity within CAOs. The mean precipitation intensity within CAOs in the midlatitudes is 0.5 mm/3hr (Figure 5g), consistent with Papritz and Sodemann (2018), who showed that CAO precipitation intensity ranges between 0.1 mm/hr and 1 mm/hr during an intense CAO in the Nordic Seas. The smallest contribution of all categories within the midlatitudes in DJF is associated with precipitation occurring within an ETC and a CAO (CCAO, Figure 4h), although the precipitation intensity is greater than during CAO only (on average 0.6 mm/3hr in the midlatitudes, Figure 5 g,h).

Downstream in the stormtracks over the midlatitude ocean, the mean precipitation intensities decrease (Figure 5) with the mean precipitation intensity for MTAs (A, Figure 5c) over the midlatitude ocean being relatively weak (1 mm/3hr) compared to when MTAs co-occur with ETCs (CA,

1.7 mm/3hr, Figure 5e), fronts (AF, 1.4 mm/3hr, Figure 5f), or both (CAF, 2.3 mm/3hr, Figure 5i). This is consistent with MTAs by themselves not being associated with lift. In contrast, fronts are associated with lift, though fronts in isolation (F, Figure 5b) are associated with relatively weak precipitation if they do not co-occur with MTAs (AF, 0.8 mm/3hr, Figure 5f) providing sufficient moisture. Similarly, ETCs only produce weak intensities (C, 0.8 mm/3hr, Figure 5a).

The difference between DJF and JJA in the stormtrack regions is small (Figure 4, Figure 6). Even though the stormtracks in the NH appear more zonal in JJA than DJF in terms of the distribution of ETCs (Figure 1a,b), this difference in orientation is not visible in the precipitation categories (Figure 4, Figure 6). However, summing all the precipitation associated with different combinations of ETCs yields a more zonal structure in summer, consistent with Hawcroft et al. (2012) (not shown). More discernible is the increased contribution from A, AF, and CAF poleward and eastward in summer (Figure 6c,f,i) compared to winter (Figure 4c,f,i), while CAO has no contribution in summer (Figure 6g).

The precipitation associated with fronts, or combinations of fronts with other weather features, along the North Atlantic stormtrack (Figure 4b,d,f,j) reveals a broadly consistent result compared to Hénin et al. (2019), with fronts contributing up to 80% over the Gulf Stream region in DJF. However, our estimates are slightly lower than Catto et al. (2012), especially downstream in the stormtrack regions. Furthermore, while our frontal contributions feature a decrease downstream in the stormtracks (Figure 4b,d,f,j), Utsumi et al. (2017) found an increase.

This discrepancy is most likely due to their attribution method, which evenly attributes precipitation to ETCs and fronts in the event of co-occurrence. As fronts and ETCs tend to be collocated in the maturing stage of ETCs and less so during the decaying stage (Schemm et al. (2018) and Figure 3a,b), their approach results in a partition of precipitation between ETCs and fronts in the upstream region, but not in the downstream region.

Towards the end of the stormtracks, when approaching the western shoreline of the respective continents, ARs are known to be a significant contributor to precipitation, contributing up to 50% of the annual rainfall in Western US (Gershunov et al. 2017) and Chile (Viale et al. 2018). Towards the coasts, A becomes relatively more important (Figure 4c), while CAF becomes relatively less important downstream in the stormtrack, where it contributes around 20% along the Western US, over Norway, and the British Isles (Figure 4i).

The intersection of the flow with topography can provide significant lift, explaining why A is relatively more important over the continents than the oceans. For A along the coastlines, particularly the North American west coast and Chile, there is a marked increase in precipitation intensity compared to further offshore (Figure 5 c). Consequently, the intensity increase is larger for MTAs in isolation (A) compared to when MTAs occur together with other features (CA, AF, CAF, Figure 5e,f,i). In southern Chile, A contributes substantially to precipitation (25-30%) and is relatively more important than CAF (10-15%) and AF (15-20%) in JJA (figure 6). However, despite the topography acting as a mechanism for lift, A only contributes only 10-15% along the North American West Coast in DJF, highlighting the importance of the circulation associated with ETCs and fronts.

Over the continents, most of the precipitation in summer is unclassified, with the fraction of unclassified precipitation being higher in summer than in winter (Figure 6j, Figure 4j). For example, in Southern Europe (Mediterranean in Iturbide et al. (2020)), the precipitation contribution from unclassified increases from 34% in DJF to 47% in JJA (Figure 6j, Figure 4j). While virtually all the unclassified precipitation over the NH continents is convective for JJA (Figure S1 in Supplementary Material), the mean unclassified precipitation intensities are still small (0.9mm/3hr) compared to when weather features are present (CAF, 2mm/3hr, Figure 7i).

Over the Great Plains in the US, Mesoscale Convective Systems (MCS) are known to contribute to 30-70% of the precipitation (Feng et al. 2021). Even though MCSs are not considered a category in our attribution, we attribute 79% of the precipitation during summer in the region (Figure 6j), indicating that other features are often present during MCSs. Most precipitation over the Great Plains is attributed to AF, implying that MTAs and fronts tend to organize the convection. Indeed, MTAs identify a corridor of moisture transport from the Gulf Stream to the Great Plains (Figure 1f). This moisture transport is likely associated with the Great Plains Low-Level Jet that organizes the MCSs in the region Feng et al. (2019).

b. High Latitudes

Despite weather features being only present 16% of the time poleward of 60°N (Figure 1i,j), we still attribute more than 80% of the precipitation with C being the main contributor to Arctic precipitation in DJF (25%, Figure 4a), while CAF contributes most in JJA (21%, Figure 6f). Similar
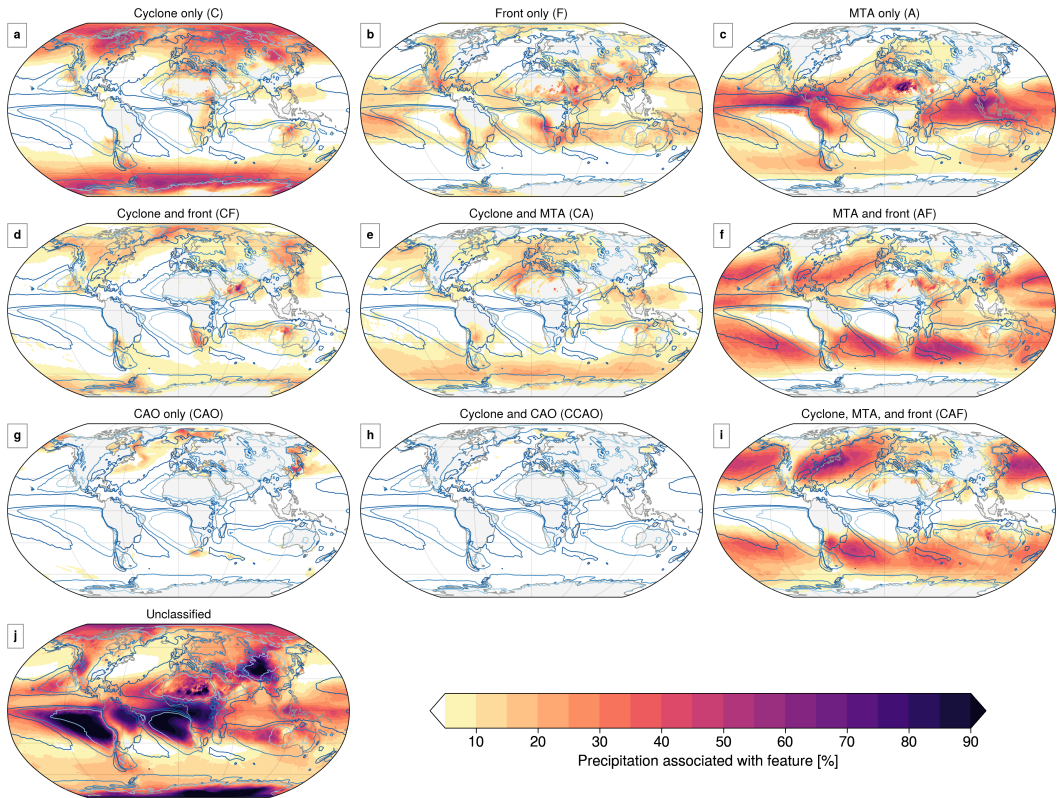
FIG. 4. Relative contribution of ETC only (a), Front only (b), MTA only (c), ETC and front (d), ETC and MTA (e), MTA and front (f), CAO only (g), ETC and CAO (h), ETC, MTA, and fronts (i), and Unclassified (j) to precipitation in DJF (shading). Contours mark the climatology of total accumulated precipitation: 50 mm/season (light blue) and 150 mm/season (dark blue).

to the midlatitudes, the strongest precipitation in the high latitudes occurs when ETCs, fronts, and MTAs co-occur, while the precipitation during ETCs only and unclassified is weak (Figure 5). However, there is a clear difference between the Pacific and Atlantic sectors of the Arctic Ocean, with the amount of attributed precipitation being higher in the Atlantic sector. This is associated with more weather features entering the Arctic from the North Atlantic, as seen in the pattern of frequency of occurrence of weather features (Figure 1).

CAO precipitation dominates in the Barents Sea and the Fram Strait in DJF (Figure 4), though most precipitation associated with CAOs tends to occur downstream when the flow intersects

17
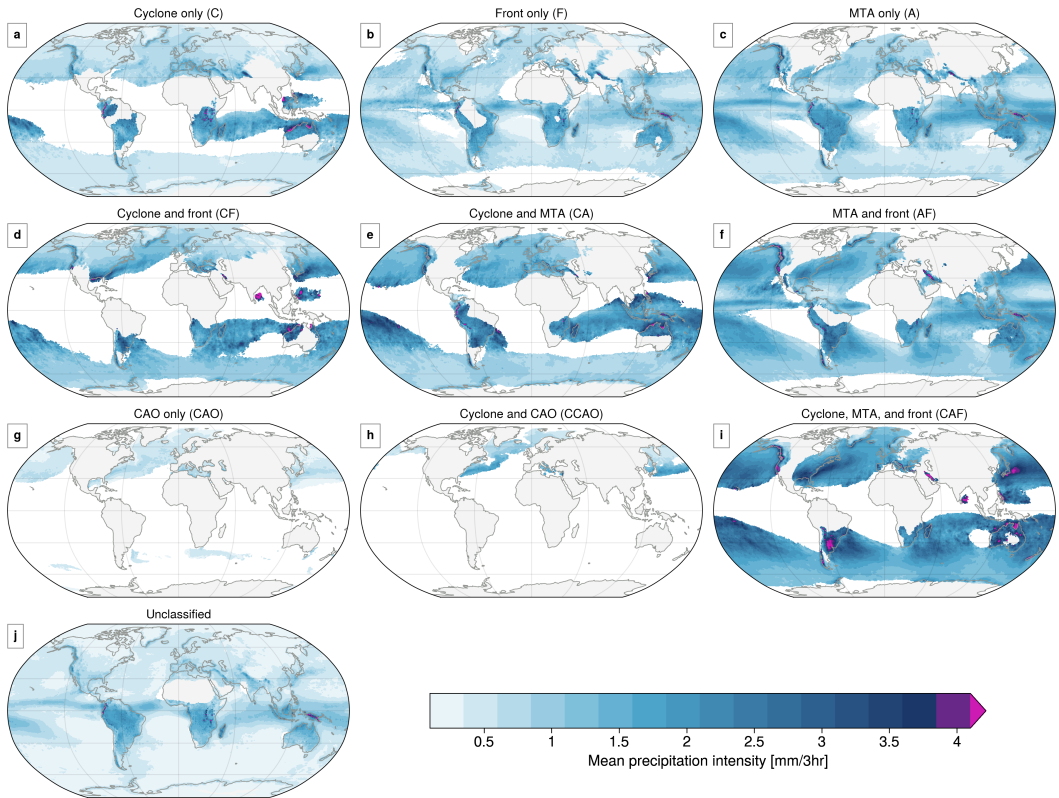
FIG. 5. Mean precipitation intensity during wet time steps in the different categories in DJF, with panels as in Figure 4. Intensity for the different categories is only shown in regions where the respective category occurred more than 1% within one season in more than 30% of the seasons.

with topography (Papritz and Sodemann 2018). We, however, do not consider this effect, as CAOs according to our definition cannot occur over land. Hence, the contribution from CAO to DJF precipitation, particularly in Northern Norway and Japan, may be underestimated. CCAO contributes less than CAO in the NH in DJF (Figure 4g,h), though for CCAO the precipitation intensity is higher than for CAO (figure 5g,h). In SH winter, CCAO does not contribute to precipitation anywhere, indicating that ETCs seldom overlap with CAOs. Overall, CAOs generally contribute less to precipitation in the SH than in NH.

Poleward of 60°S, C contributes most to precipitation in DJF (40%) but generally less in JJA (26%). Instead, in JJA, CF is the main contributor to precipitation. C produces considerably weaker

18
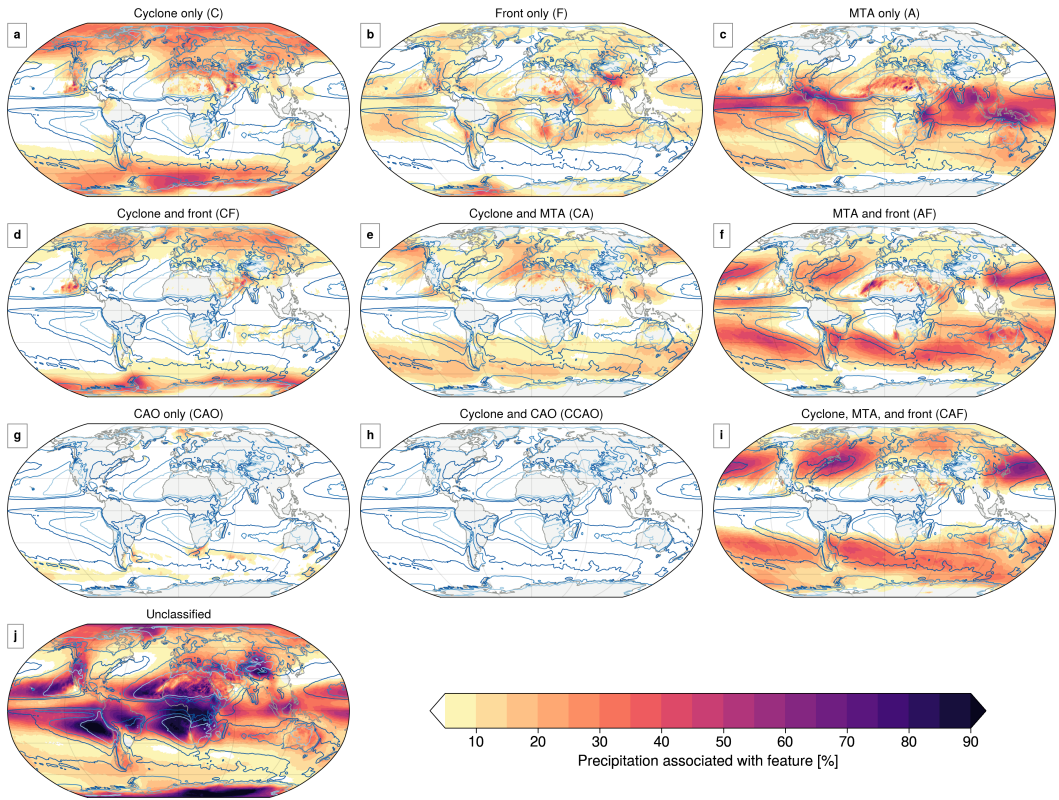
Fig. 6. Same as Figure 4 but for JJA.

precipitation (less than 1 mm/3hr) than the combined categories such as CAF (up to 2mm/3hr) and CA (up to 1.5 mm/3hr) Figure 7). Although MTAs occur only infrequently over Eastern Antarctica (Figure 1e,f), CAF contributes up to 25% of the precipitation in this region in JJA (Figure 6i), demonstrating the impact of MTAs on seasonal timescales. We attribute most of the precipitation in coastal Antarctica, but virtually none over the continent (Figure 4j, Figure 6j). The Antarctic continent is, however, a region of very little precipitation, where we only consider <10% of the annual precipitation with our precipitation intensity threshold. Due to its high orography, the Antarctic continent also barely features any weather features (Figure 1i,j).

19
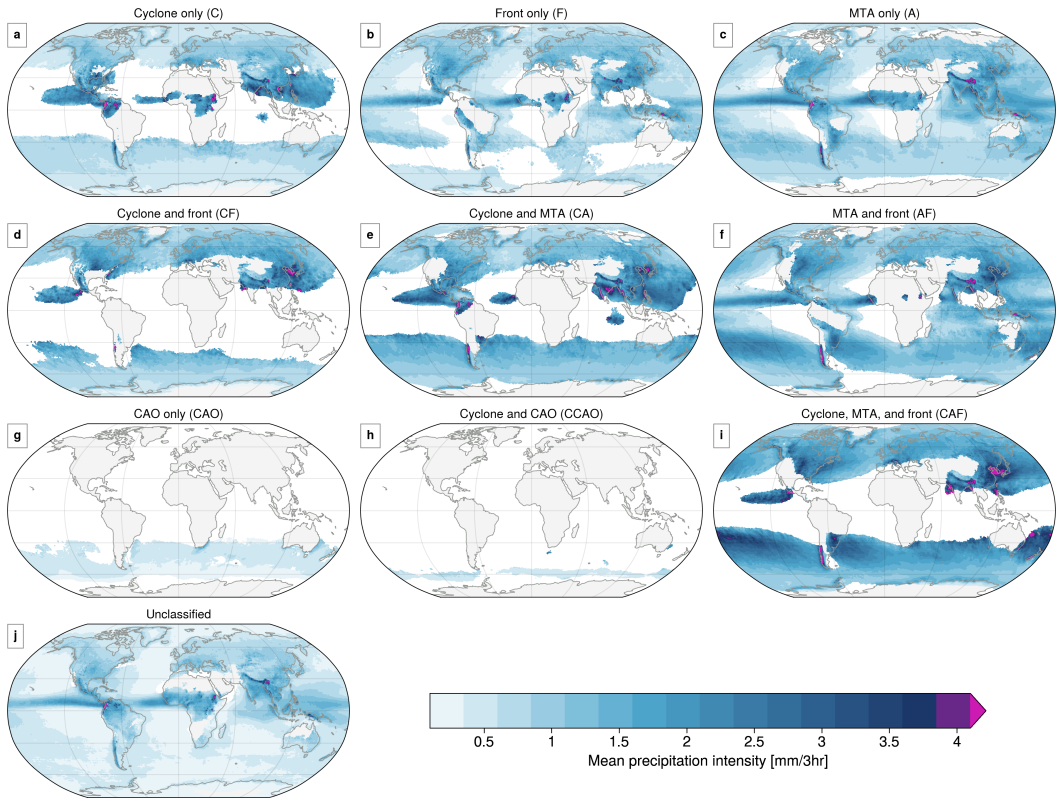
FIG. 7. Same as Figure 6, but for JJA.

c. Subtropics and Tropics

The only weather phenomenon we consider in the tropics are MTAs, which encompass both the ITCZ and the Monsoon circulation (Spensberger et al. 2023). Thus, A contributes most to precipitation in the Tropics (30%, Figure 4c, Figure 6c), while 33% remain unclassified. Because we detect fronts based on equivalent potential temperature, moisture gradients are sometimes also picked up as fronts, leading to F contributing with 8%, and AF with 14% to precipitation in the tropics.

The precipitation in the ITCZ and Monsoon regions is most intense when either a MTA or a front is present. Unlike the midlatitudes (Figure 5, Figure 7), there is less difference in the precipitation intensity between A and AF, presumably because even though a feature is present, convection is the main mechanism providing lift.

20

Large portions of the precipitation over the Amazon are classified as MTA in DJF (30%, Figure 4c). MTAs in this region are most likely associated with the South American Low-Level Jet that directs moisture from the Tropics to the La Plata Basin (e.g., Algarra et al. 2019). This pathway of moisture transport is clearly visible in the MTA climatology (Figure 1e,f).

In the shallow convection zones in the subtropics, all of the precipitation is unclassified (Figure 4j, Figure 6j). These regions are also relatively dry, with a mean precipitation intensity below 0.25 mm/3hr (Figure 5j, Figure 7j) and no detected weather features (Figure 1e,f).

Despite the dryness and lack of weather features in the Sahel and Sahara, 25% of the precipitation in JJA is attributable to A. This is in agreement with ARs contributing to more than 30% of the annual precipitation in the West Sahara (Khouakhi et al. 2022) and that MTAs in the Sahel are typically associated with precipitation (Spensberger et al. 2023, their Figure 7i). However, precipitation associated with MTAs (A) is highly intermittent, occurring in less than 30% of the seasons (filtered out in figures 5 and 7). As 70-90% of the precipitation in this region being caused by MCSs (Mathon et al. 2002), the high fraction of unclassified precipitation in JJA indicates that the convection in this region is not organized by the detected features (Figure 6).

Off the coast of California and Mexico, there is a hot spot with contributions from C, CF, and AF in JJA (Figure 6a,d,f), which is absent in DJF (Figure 4). These categories are also associated with intense precipitation, with more than 3 mm/3hr (figure 7 a,d,i). As Rodgers et al. (2001) showed that TCs contribute up to 50% of the precipitation west of Mexico, this attribution is most likely due to tropical cyclones (TCs) that have become sufficiently large to be detected as ETCs. Because of the large moisture transport in TCs, MTAs often occur as a ring around the center of the TC (see Figure 2 in Spensberger et al. (2023)). A similar pattern is evident between Australia and Madagascar in SH summer (Figure 4a,d,i), where Utsumi et al. (2017) found TCs to contribute to 50% of the precipitation. While our analysis shows lower attributions to C, CF, and AF, one should bear in mind that the seasons we present here are not peak TC seasons in any of these regions.

4. Extreme Precipitation

In general, we have a higher attribution rate globally for extreme precipitation events (86%, Figure 8j) than for wet events (60%). Note that we consider 3-hourly precipitation extremes that tend to be more influenced by convection compared to when using 6-hourly data. Utsumi et al.

21

(2017), however, found no discernible differences between 1-hourly and 24-hourly precipitation
extremes, where the co-occurrence of ETCs and fronts accounted for 90% of the precipitation
extremes on both time scales.

There is a clear seasonal cycle for extreme events (Figure 9). Over the ocean, most extreme
events tend to occur during autumn (SON in NH and MAM in SH), while most extreme events over
the continents occur in summer. The summer extremes over the continents are most likely related
to convection. Over the ocean outside California, however, the most extreme events tend to occur
during DJF. Similarly, the most extreme precipitation events in the SH during JJA occur along the
western side of the continents. This pattern aligns well with the seasonal precipitation distribution
and is equally attributed to AF and CAF (not shown).

Although most extreme precipitation over the midlatitude continents occurs during summer, the
bulk of these events is connected to a weather feature (Figure 8j). Thus, despite local convection
most likely being one of the main drivers of extreme precipitation events (Hand et al. 2004;
Lenderink and Attema 2015), they are most often still organized by synoptic-scale disturbances.
Furthermore, these synoptic scale features tend to co-occur during extreme precipitation, with the
contribution to extreme precipitation from any weather feature in isolation being negligible. This
is largely consistent with previous results, showing that the most extreme events occur when ETCs
and fronts co-occur (Catto and Pfahl 2013; Dowdy and Catto 2017). When also considering MTAs,
we find that most extreme events in the midlatitudes are caused by the co-occurrence of these three;
ETCs, fronts, and MTAs (CAF). CAF occurs markedly more frequently for extreme events than
for wet events and extends considerably further into the continents. Over land in the midlatitudes,
CAF occurs <9% during wet events, while it is connected to >29% of the extreme events.

In the Arctic, where a relative majority of the precipitation occurs during ETC only (C is
responsible for 29% of the wet events), CAF contributes most to extreme events. CAF accounts for
39% of the extreme events, compared to only 6% of the wet events. C, on the other hand, accounts
only for 11% of extreme events. Despite being a major contributor to the annual precipitation in the
NH high latitudes, CAO and CCAO are not associated with extreme precipitation events anywhere.

The pattern is similar around Antarctica, where CAF dominates during extreme events (35%),
although occurring relatively infrequently during wet events (9%). The main discrepancy between
the Arctic and the Antarctic is the importance of CA, which causes more extreme events in
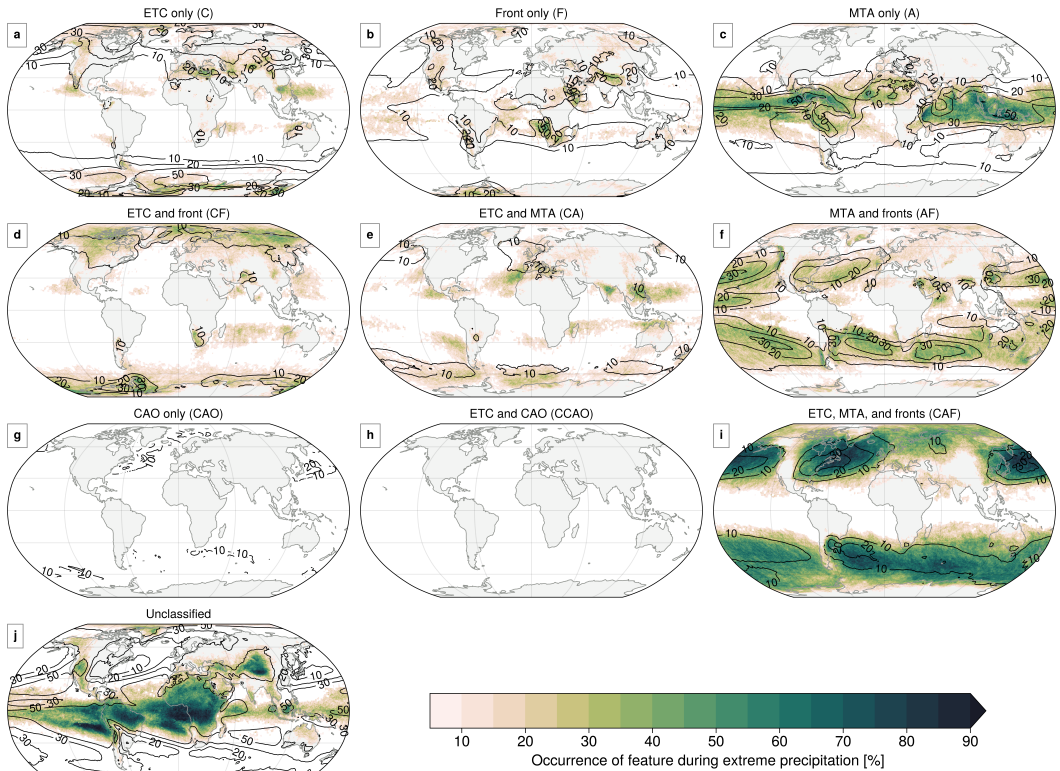
FIG. 8. Percentage of annual 3-hourly extreme events (99.9%) caused by the weather features (shading). Black contours mark the percentage of wet events (>0.1 mm/3hr) caused by the weather features. Panels are as in Figure 4.

Antarctica (13%) than in the Arctic (8%). Overall, extreme precipitation events in polar regions are mainly caused by a combination of features, particularly CAF, showing the importance of moisture transport towards higher latitudes.

There is generally little difference between mean and extreme precipitation events in the tropics, most likely related to the lack of different weather features to distinguish between types of events. Precipitation in the subtropics remains largely unclassified. However, cyclones and MTAs tend to be important for extreme precipitation in the Pacific west of Mexico, which might be related to TCs, as discussed earlier.

23
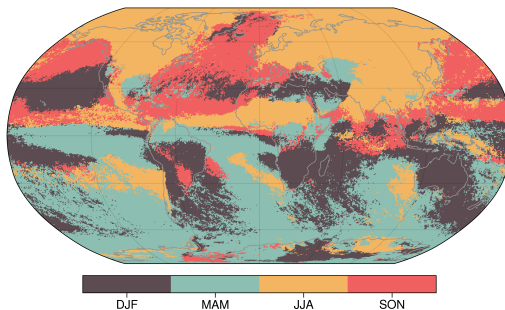
F<small>IG</small>. 9. The season in which the most 3-hourly extreme events (99.9%) occur.

5. Concluding Remarks

We introduce a new method to attribute precipitation to weather features and present the first global climatology of ETCs, fronts, ARs, CAOs, and their contribution to precipitation. Unlike previous studies, our method does not depend on a fixed distance threshold between the weather feature and the precipitation. Therefore, we can provide more consistent estimates of the relative importance of the weather features for precipitation. Overall, the attribution patterns are qualitatively similar to those of the previous studies, though we attribute relatively less to the weather features despite having a more comprehensive selection of weather features.

With our method, we classify 75% of the precipitation (exceeding 0.1 mm/3hr) globally as belonging to one or more weather features. The remaining 25% are unclassified. Most precipitation in the midlatitudes is associated with the co-occurrence of ETC, fronts, and MTAs (CAF), followed by MTAs and fronts (AF). CAF is relatively less important over the continents but still represents the second largest contributor after the unclassified category. Moreover, precipitation associated with CAF is consistently more intense than the other categories in the midlatitudes.

Despite weather features occurring relatively seldom in high latitudes, most of the precipitation (80%) occurs in association with synoptic-scale systems. ETC only (C) dominates the precipitation in these regions, despite the relatively weak intensity (< 1mm/3hr). CAF contributes 15% of the precipitation, and AF 5%, indicating that the impact of MTAs and fronts is evident on an annual scale despite occurring less than 2.5% of the time in these regions.

In the subtropical shallow convection zones, precipitation remains largely unattributed due to the region's lack of detected weather features. In contrast, a substantial amount of precipitation in

24

the tropics is assigned to MTAs (30%), as MTA is the only tropical weather feature we consider, picking up the moisture transport associated with the ITCZ and monsoon circulations.

The co-occurrence of weather features is dominating extreme precipitation events. In the mid-latitudes, CAF occurs during 36% of the extreme events, almost four times as often as during regular precipitation events. This is also the case over the continents, where most extreme precipitation events occur during summer, mostly associated with convection. Thus, synoptic-scale perturbations provide an environment favourable for convection and intense precipitation.

Considering the combination of features rather than the features in isolation gives insight into the required ingredients for precipitation. For example, the presence of an MTA can be considered to be an indication of relatively high moisture availability. However, the mere presence of MTAs is insufficient, with the associated precipitation intensity over the ocean being much weaker than when MTAs co-occur with fronts or ETCs. Thus, MTAs require a mechanism generating lift to produce relatively intense precipitation. On the other hand, a front by itself does not produce strong precipitation by itself unless the air is moist. Hence, considering only one feature in isolation makes it more difficult to distinguish why some features are associated with intense precipitation and others are not. It is, therefore, vital to consider multiple features and their combinations for attribution studies.

We demonstrated that our approach is well suited to attribute precipitation to different weather features across different geographic regions and climates, independent of given thresholds or a radius of influence. Given that precipitation is predominately linked to ETCs, fronts, MTAs, CAOs, or their combination, our attribution provides the basis to study the mechanisms leading to precipitation. Given the uncertainties of future changes in mean and extreme precipitation, our approach can thus help to separate the causes of these changes by attributing them to changes in the features themselves or to changes in the precipitation associated with the features.

References

Algarra, I., J. Eiras-Barca, R. Nieto, and L. Gimeno, 2019: Global climatology of nocturnal low-level jets and associated moisture sources and sinks. *Atmospheric Research*, **229 (June)**, 39–59, https://doi.org/10.1016/j.atmosres.2019.06.016, URL https://doi.org/10.1016/j.atmosres.2019.06.016.

Beucher, S., and C. Lantuejoul, 1979: Use of Watersheds in Contour Detection. *International Workshop on Image Processing: Real-time Edge and Motion Detection/Estimation*, 12–21, URL http://cmm.ensmp.fr/{~}beucher/publi/watershed.pdf.

Catto, J. L., C. Jakob, G. Berry, and N. Nicholls, 2012: Relating global precipitation to atmospheric fronts. *Geophysical Research Letters*, **39 (10)**, 1–6, https://doi.org/10.1029/2012GL051736, URL https://onlinelibrary.wiley.com/doi/full/10.1029/2012GL051736https://onlinelibrary.wiley.com/doi/abs/10.1029/2012GL051736https://agupubs.onlinelibrary.wiley.com/doi/10.1029/2012GL051736http://doi.wiley.com/10.1029/2012GL051736.

Catto, J. L., and S. Pfahl, 2013: The importance of fronts for extreme precipitation. *Journal of Geophysical Research Atmospheres*, **118 (19)**, 10,791–10,801, https://doi.org/10.1002/jgrd.50852, URL https://onlinelibrary.wiley.com/doi/full/10.1002/jgrd.50852https://onlinelibrary.wiley.com/doi/abs/10.1002/jgrd.50852https://agupubs.onlinelibrary.wiley.com/doi/10.1002/jgrd.50852http://doi.wiley.com/10.1002/jgrd.50852.

Dowdy, A. J., and J. L. Catto, 2017: Extreme weather caused by concurrent cyclone, front and thunderstorm occurrences. *Scientific Reports*, **7 (1)**, 1–8, https://doi.org/10.1038/srep40359, URL http://dx.doi.org/10.1038/srep40359https://www.nature.com/articles/srep40359.

Feng, Z., R. A. Houze, L. R. Leung, F. Song, J. C. Hardin, J. Wang, W. I. Gustafson, and C. R. Homeyer, 2019: Spatiotemporal characteristics and large-scale environments of mesoscale

convective systems east of the rocky mountains. *Journal of Climate*, **32 (21)**, 7303–7328, https://doi.org/10.1175/JCLI-D-19-0137.1.

Feng, Z., and Coauthors, 2021: A Global High-Resolution Mesoscale Convective System Database Using Satellite-Derived Cloud Tops, Surface Precipitation, and Tracking. *Journal of Geophysical Research: Atmospheres*, **126 (8)**, 1–29, https://doi.org/10.1029/2020JD034202.

Gershunov, A., T. Shulgina, F. M. Ralph, D. A. Lavers, and J. J. Rutz, 2017: Assessing the climate-scale variability of atmospheric rivers affecting western North America. *Geophysical Research Letters*, **44 (15)**, 7900–7908, https://doi.org/10.1002/2017GL074175.

González-Herrero, S., F. Vasallo, J. Bech, I. Gorodetskaya, B. Elvira, and A. Justel, 2023: Extreme precipitation records in Antarctica. *International Journal of Climatology*, **(January)**, 1–14, https://doi.org/10.1002/joc.8020, URL https://onlinelibrary.wiley.com/doi/10.1002/joc.8020.

Gorodetskaya, I. V., M. Tsukernik, K. Claes, M. F. Ralph, W. D. Neff, and N. P. Van Lipzig, 2014: The role of atmospheric rivers in anomalous snow accumulation in East Antarctica. *Geophysical Research Letters*, **41 (17)**, 6199–6206, https://doi.org/10.1002/2014GL060881.

Guan, B., D. E. Waliser, and F. M. Ralph, 2023: Global Application of the Atmospheric River Scale. *Journal of Geophysical Research: Atmospheres*, **128 (3)**, 238–238, https://doi.org/10.1029/2022JD037180, URL https://www.nature.com/articles/175238c0https://onlinelibrary.wiley.com/doi/10.1029/2022JD037180.

Hand, W. H., N. I. Fox, and C. G. Collier, 2004: A study of twentieth-century extreme rainfall events in the United Kingdom with implications for forecasting. *Meteorological Applications*, **11 (1)**, 15–31, https://doi.org/10.1017/S1350482703001117, URL http://doi.wiley.com/10.1017/S1350482703001117.

Hawcroft, M. K., L. C. Shaffrey, K. I. Hodges, and H. F. Dacre, 2012: How much Northern Hemisphere precipitation is associated with extratropical cyclones? *Geophysical Research Letters*, **39 (24)**, 1–7, https://doi.org/10.1029/2012GL053866, URL https://onlinelibrary.wiley.com/doi/abs/10.1029/2012GL053866.

Hénin, R., A. M. Ramos, S. Schemm, C. M. Gouveia, and M. L. R. Liberato, 2019: Assigning precipitation to mid-latitudes fronts on sub-daily scales in the North Atlantic and European sector:

Climatology and trends. *International Journal of Climatology*, **39 (1)**, 317–330, https://doi.org/
10.1002/joc.5808, URL https://onlinelibrary.wiley.com/doi/10.1002/joc.5808.

Hersbach, H., and Coauthors, 2020: The ERA5 global reanalysis. *Quarterly Journal of the Royal Meteorological Society*, **146 (730)**, 1999–2049, https://doi.org/10.1002/qj.3803.

Iturbide, M., and Coauthors, 2020: An update of IPCC climate reference regions for subcontinental analysis of climate model data: definition and aggregated datasets. *Earth System Science Data*, **12 (4)**, 2959–2970, https://doi.org/10.5194/essd-12-2959-2020.

Khouakhi, A., F. Driouech, L. Slater, T. Waine, O. Chafki, A. Chehbouni, and O. Raji, 2022: Atmospheric rivers and associated extreme rainfall over Morocco. *International Journal of Climatology*, **42 (15)**, 7766–7778, https://doi.org/10.1002/joc.7676, URL https://onlinelibrary. wiley.com/doi/10.1002/joc.7676.

Klein Tank, A. M., F. W. Zwiers, and X. Zhang, 2009: Guidelines on Analysis of extremes in a changing climate in support of informed decisions for adaptations. Tech. Rep. WCDMP-No. 72, WMO, 52 pp. URL https://library.wmo.int/doc{_}num.php?explnum{_}id=9419.

Lavers, D. A., A. Simmons, F. Vamborg, and M. J. Rodwell, 2022: An evaluation of ERA5 precipitation for climate monitoring. *Quarterly Journal of the Royal Meteorological Society*, **148 (748)**, 3152–3165, https://doi.org/10.1002/qj.4351, URL https://onlinelibrary.wiley.com/ doi/10.1002/qj.4351.

Lavers, D. A., and G. Villarini, 2013: The nexus between atmospheric rivers and extreme precipitation across Europe. *Geophysical Research Letters*, **40 (12)**, 3259–3264, https://doi.org/
10.1002/grl.50636.

Lenderink, G., and J. Attema, 2015: A simple scaling approach to produce climate scenarios of local precipitation extremes for the Netherlands. *Environmental Research Letters*, **10 (8)**, 085 001, https://doi.org/10.1088/1748-9326/10/8/085001, URL https://iopscience.iop. org/article/10.1088/1748-9326/10/8/085001.

Mathon, V., H. Laurent, and T. Lebel, 2002: Mesoscale Convective System Rainfall in the Sahel. *Journal of Applied Meteorology*, **41 (11)**, 1081–1092, https://doi.org/10.1175/1520-0450(2002)

041⟨1081:MCSRIT⟩2.0.CO;2, URL http://journals.ametsoc.org/doi/10.1175/1520-0450(2002) 041⟨3C1081:MCSRIT⟩3E2.0.CO;2.

Nash, D., L. M. Carvalho, C. Jones, and Q. Ding, 2022: Winter and spring atmospheric rivers in High Mountain Asia: climatology, dynamics, and variability. *Climate Dynamics*, **58 (9-10)**, 2309–2331, https://doi.org/10.1007/s00382-021-06008-z, URL https://doi.org/10.1007/ s00382-021-06008-z.

Nogueira, M., 2020: Inter-comparison of ERA-5, ERA-interim and GPCP rainfall over the last 40 years: Process-based analysis of systematic and random differences. *Journal of Hydrology*, **583 (August 2019)**, 124 632, https://doi.org/10.1016/j.jhydrol.2020.124632, URL https://doi. org/10.1016/j.jhydrol.2020.124632.

Papritz, L., S. Pfahl, I. Rudeva, I. Simmonds, H. Sodemann, and H. Wernli, 2014: The role of extratropical cyclones and fronts for Southern Ocean freshwater fluxes. *Journal of Climate*, **27 (16)**, 6205–6224, https://doi.org/10.1175/JCLI-D-13-00409.1.

Papritz, L., S. Pfahl, H. Sodemann, and H. Wernli, 2015: A climatology of cold air outbreaks and their impact on air-sea heat fluxes in the high-latitude South Pacific. *Journal of Climate*, **28 (1)**, 342–364, https://doi.org/10.1175/JCLI-D-14-00482.1.

Papritz, L., and H. Sodemann, 2018: Characterizing the local and intense water cycle during a cold air outbreak in the Nordic seas. *Monthly Weather Review*, **146 (11)**, 3567–3588, https://doi.org/ 10.1175/MWR-D-18-0172.1, URL http://journals.ametsoc.org/doi/10.1175/MWR-D-18-0172. 1.

Papritz, L., and T. Spengler, 2017: A Lagrangian climatology of wintertime cold air outbreaks in the Irminger and Nordic Seas and their role in shaping air-sea heat fluxes. *Journal of Climate*, **30 (8)**, 2717–2737, https://doi.org/10.1175/JCLI-D-16-0605.1.

Pfahl, S., and H. Wernli, 2012: Quantifying the Relevance of Cyclones for Precipitation Extremes. *Journal of Climate*, **25 (19)**, 6770–6780, https://doi.org/10.1175/JCLI-D-11-00705.1, URL http://journals.ametsoc.org/doi/10.1175/JCLI-D-11-00705.1.

Ralph, F. M., P. J. Neiman, G. A. Wick, S. I. Gutman, M. D. Dettinger, D. R. Cayan, and A. B. White, 2006: Flooding on California's Russian River: Role of atmospheric rivers. *Geophysical Research Letters*, **33 (13)**, 3–7, https://doi.org/10.1029/2006GL026689.

Reid, K. J., A. D. King, T. P. Lane, and D. Hudson, 2022: Tropical, Subtropical, and Extratropical Atmospheric Rivers in the Australian Region. *Journal of Climate*, **35 (9)**, 2697–2708, https://doi.org/10.1175/JCLI-D-21-0606.1, URL https://journals.ametsoc.org/view/journals/clim/35/9/JCLI-D-21-0606.1.xml.

Rodgers, E. B., R. F. Adler, and H. F. Pierce, 2001: Contribution of tropical cyclones to the North Atlantic climatological rainfall as observed from satellites. *Journal of Applied Meteorology*, **40 (11)**, 1785–1800, https://doi.org/10.1175/1520-0450(2001)040⟨1785:COTCTT⟩2.0.CO;2.

Rüdisühli, S., M. Sprenger, D. Leutwyler, C. Schär, and H. Wernli, 2020: Attribution of precipitation to cyclones and fronts over Europe in a kilometer-scale regional climate simulation. *Weather and Climate Dynamics*, **1 (2)**, 675–699, https://doi.org/10.5194/wcd-1-675-2020.

Rutz, J. J., and Coauthors, 2019: The Atmospheric River Tracking Method Intercomparison Project (ARTMIP): Quantifying Uncertainties in Atmospheric River Climatology. *Journal of Geophysical Research: Atmospheres*, **124 (24)**, 13 777–13 802, https://doi.org/10.1029/2019JD030936, URL https://onlinelibrary.wiley.com/doi/10.1029/2019JD030936.

Schär, C., and Coauthors, 2016: Percentile indices for assessing changes in heavy precipitation events. *Climatic Change*, **137 (1-2)**, 201–216, https://doi.org/10.1007/s10584-016-1669-2, URL http://dx.doi.org/10.1007/s10584-016-1669-2.

Schemm, S., M. Sprenger, and H. Wernli, 2018: When during Their Life Cycle Are Extratropical Cyclones Attended by Fronts? *Bulletin of the American Meteorological Society*, **99 (1)**, 149–165, https://doi.org/10.1175/BAMS-D-16-0261.1, URL https://journals.ametsoc.org/doi/10.1175/BAMS-D-16-0261.1.

Serreze, M. C., A. D. Crawford, and A. P. Barrett, 2015: Extreme daily precipitation events at Spitsbergen, an Arctic Island. *International Journal of Climatology*, **35 (15)**, 4574–4588, https://doi.org/10.1002/joc.4308.

Serreze, M. C., J. Voveris, A. P. Barrett, S. Fox, P. D. Blanken, and A. Crawford, 2022: Characteristics of extreme daily precipitation events over the Canadian Arctic. *International Journal of Climatology*, **42 (16)**, 10 353–10 372, https://doi.org/10.1002/joc.7907, URL https://onlinelibrary.wiley.com/doi/10.1002/joc.7907.

Shields, C. A., J. D. Wille, A. B. Marquardt Collow, M. Maclennan, and I. V. Gorodetskaya, 2022: Evaluating Uncertainty and Modes of Variability for Antarctic Atmospheric Rivers. *Geophysical Research Letters*, **49 (16)**, https://doi.org/10.1029/2022GL099577.

Solari, F. I., J. Blázquez, and S. A. Solman, 2022: Relationship between frontal systems and extreme precipitation over southern South America. *International Journal of Climatology*, **42 (15)**, 7535–7549, https://doi.org/10.1002/joc.7663, URL https://onlinelibrary.wiley.com/doi/10.1002/joc.7663.

Sørland, S. L., and A. Sorteberg, 2015: The dynamic and thermodynamic structure of monsoon low-pressure systems during extreme rainfall events. *Tellus, Series A: Dynamic Meteorology and Oceanography*, **67 (1)**, https://doi.org/10.3402/tellusa.v67.27039.

Soster, F., and R. Parfitt, 2022: On Objective Identification of Atmospheric Fronts and Frontal Precipitation in Reanalysis Datasets. *Journal of Climate*, **35 (14)**, 4513–4534, https://doi.org/10.1175/JCLI-D-21-0596.1, URL https://journals.ametsoc.org/view/journals/clim/35/14/JCLI-D-21-0596.1.xml.

Spensberger, C., 2021: Dynlib: A library of diagnostics, feature detection algorithms, plotting and convenience functions for dynamic meteorology. Zenodo, https://doi.org/10.5281/zenodo.4639624.

Spensberger, C., K. Konstali, and T. Spengler, 2023: Moisture transport axes and their relation to atmospheric rivers and warm moist intrusions, in Preparation.

Spensberger, C., and M. Sprenger, 2018: Beyond cold and warm: an objective classification for maritime midlatitude fronts. *Quarterly Journal of the Royal Meteorological Society*, **144 (710)**, 261–277, https://doi.org/10.1002/qj.3199.

Sprenger, M., and Coauthors, 2017: Global climatologies of Eulerian and Lagrangian flow features based on ERA-Interim. *Bulletin of the American Meteorological Society*, **98 (8)**, 1739–1748, https://doi.org/10.1175/BAMS-D-15-00299.1.

Terpstra, A., I. V. Gorodetskaya, and H. Sodemann, 2021: Linking Sub-Tropical Evaporation and Extreme Precipitation Over East Antarctica: An Atmospheric River Case Study. *Journal of Geophysical Research: Atmospheres*, **126 (9)**, e2020JD033 617, https://doi.org/10.1029/2020JD033617, URL https://onlinelibrary.wiley.com/doi/full/10.1029/2020JD033617.

Turner, J., and Coauthors, 2019: The Dominant Role of Extreme Precipitation Events in Antarctic Snowfall Variability. *Geophysical Research Letters*, **46 (6)**, 3502–3511, https://doi.org/10.1029/2018GL081517.

Utsumi, N., H. Kim, S. Kanae, and T. Oki, 2017: Relative contributions of weather systems to mean and extreme global precipitation. *Journal of Geophysical Research: Atmospheres*, **122 (1)**, 152–167, https://doi.org/10.1002/2016JD025222, URL http://doi.wiley.com/10.1002/2016JD025222.

Viale, M., R. Valenzuela, R. D. Garreaud, and F. M. Ralph, 2018: Impacts of atmospheric rivers on precipitation in Southern South America. *Journal of Hydrometeorology*, **19 (10)**, 1671–1687, https://doi.org/10.1175/JHM-D-18-0006.1.

Wernli, H., and C. Schwierz, 2006: Surface cyclones in the ERA-40 dataset (1958-2001). Part I: Novel identification method and global climatology. *Journal of the atmospheric sciences*, 2486–2507, URL http://journals.ametsoc.org/doi/abs/10.1175/JAS3766.1.

Supporting information for "Global attribution of precipitation to weather features"
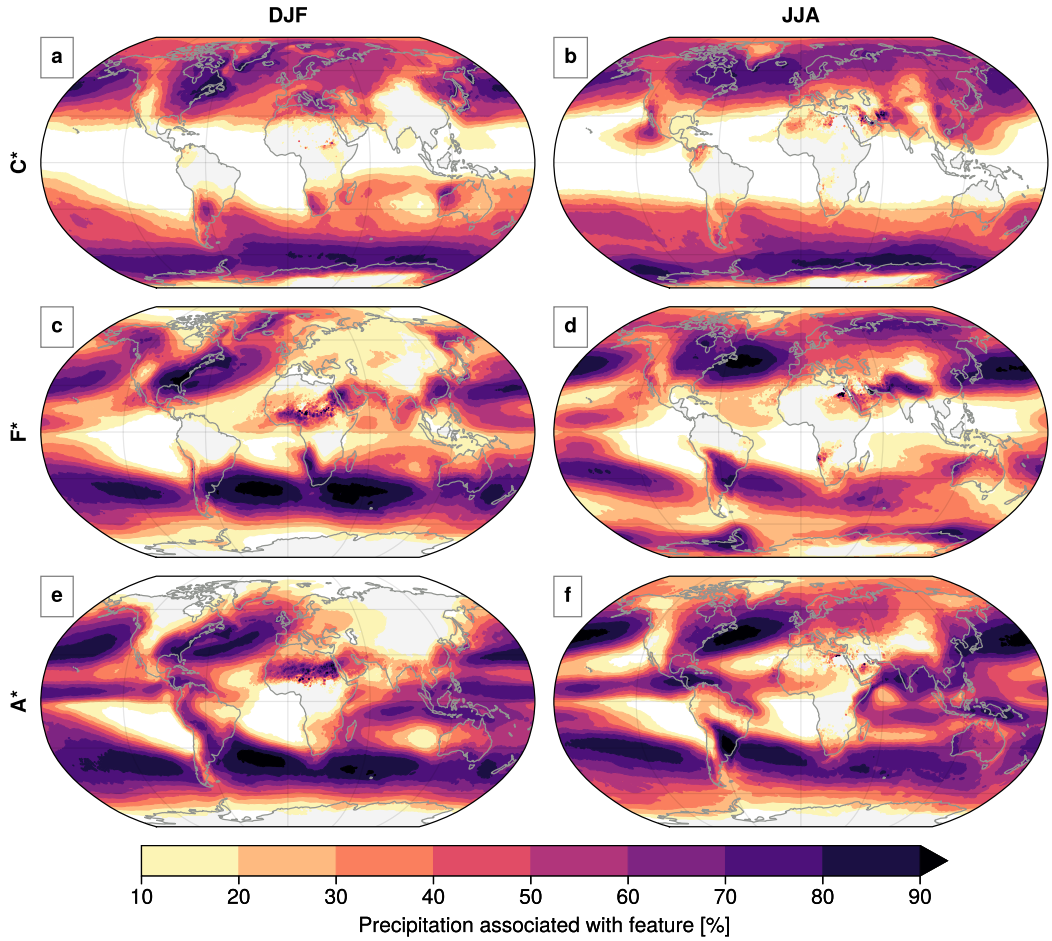
Fig. S 1. Precipitation associated with combination of features for DJF (a, c, e) and JJA (b, d, f). a, b: Combination of cyclones (C* = C + CF + CA + CAF + CCAO), c, d: combination of fronts (F* = F + CF + FA + CAF), e, f: combination of MTAs (A* = A + AF + CA + CAF).

1
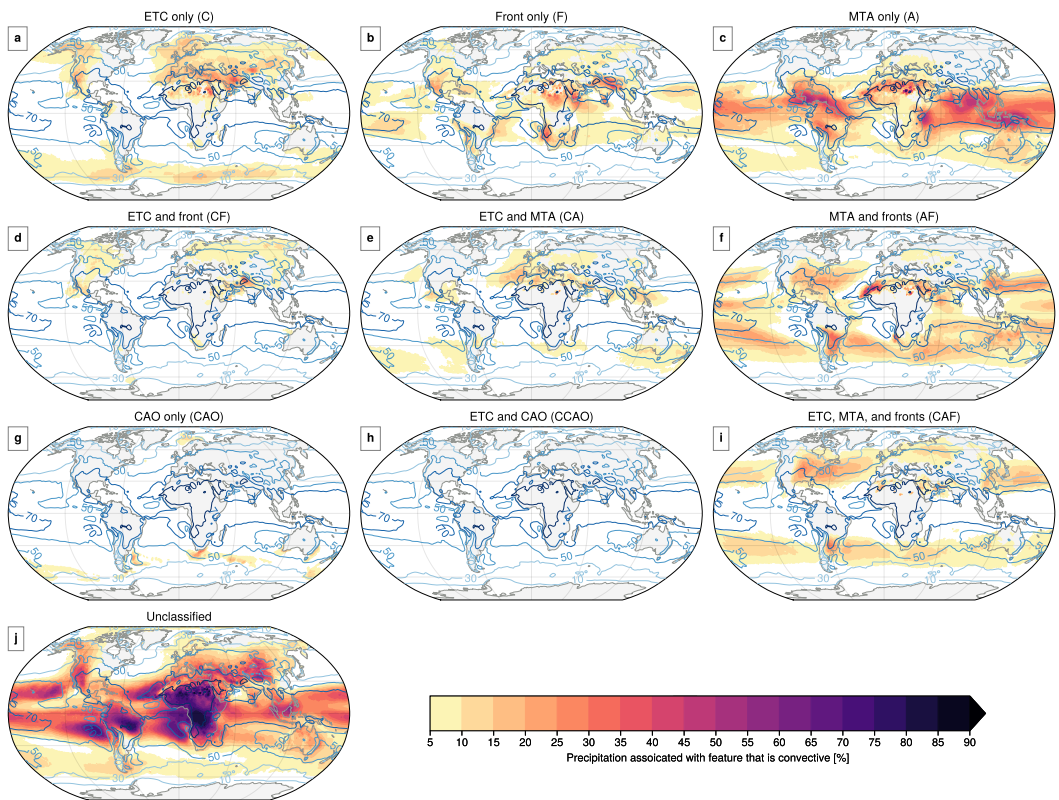
Fig. S 2. Percentage of the convective precipitation to total precipitation within the different categories for JJA. Blue contours mark the climatological contribution from convective precipitation to the total precipitation, irrespective of the category.

Paper III

Linking future precipitation changes to weather features in CESM2-LE

K. Konstali, T. Spengler, C. Spensberger, and A. Sorteberg *Manuscript in preparation,*

Paper IV

Atmospheric fronts drive future changes in extreme precipitation in the extratropics

K. Konstali, T. Spengler, C. Spensberger, and A. Sorteberg *Manuscript in preparation,*

uib.no